TAR ELIMINATION IN BIOMASS GASIFICATION – DEVELOPMENT OF Fe_2O_3/SiO_2-Al_2O_3 FLUIDIZABLE CATALYSTS AND THERMODYNAMIC MODELING

BY

MUFLIH ARISA ADNAN

A Thesis Presented to the

DEANSHIP OF GRADUATE STUDIES

KING FAHD UNIVERSITY OF PETROLEUM & MINERALS

DHAHRAN, SAUDI ARABIA

In Partial Fulfillment of the
Requirements for the Degree of

MASTER OF SCIENCE

In

CHEMICAL ENGINEERING

January 2017

KING FAHD UNIVERSITY OF PETROLEUM & MINERALS

DHAHRAN- 31261, SAUDI ARABIA

DEANSHIP OF GRADUATE STUDIES

This thesis, written by **MUFLIH ARISA ADNAN** under the direction his thesis advisor and approved by his thesis committee, has been presented and accepted by the Dean of Graduate Studies, in partial fulfillment of the requirements for the degree of **MASTER OF SCIENCE IN CHEMICAL ENGINEERING.**

Mozahar Hossain

Dr. Mohammad Mozahar Hossain
(Advisor)

Dr. Oki Muraza
(Co-Advisor)

Dr. Mohammed S. Ba-Shammakh
Department Chairman

Dr. Mohammed S. Ba-Shammakh
(Member)

Dr. Salam A. Zummo
Dean of Graduate Studies

عمادة الدراسات العليا
DEANSHIP OF GRADUATE STUDIES

12/1/17
Date

Shaikh Abdur Razzak

Dr. Shaikh Abdur Razzak
(Member)

Dr. Mohammad Rezwanul Quddus
(Member)

January 2017

Dedicated to

my beloved parents, Drs. Muhammad Basith and Dra. Sri Utami Andayaningsih,

my brother Taufiq Hidayat, and

my sisters Fatimah and Aisyah

ACKNOWLEDGMENTS

All praises and worship are for Allah, the most Beneficent, the Most Merciful. *Salawat* and blessing be upon the last Prophet Muhammad *shalallahu 'alaihi wa sallam*, his family, his companions, and all those who follow him.

I deeply thanks to my parents, Drs. Muhammad Basith and Dra. Sri Utami Andayaningsih, for their continuous supports, motivations, sacrifices, pure loves, and *du'a*. My brother Taufiq Hidayat, and my sisters Fatimah and Aisyah for their jokes and encouragements. May Allah rewards them the best in the world and hereafter.

I sincerely thank my academic advisors Dr. M. Mozahar Hossain (advisor) and Dr. Oki Muraza (co-advisor) for the kind assistance and great discussing in the field. I am also indebted to them for their patience in teaching, efforts, inspirations, supports, and encouragement during my master degree at KFUPM. I always admired their deep knowledge and vision.

I express my appreciation to Dr. M. Ba-Shammakh, Dr. Shaikh Abdurrazzak, and Dr. M. Rezwanul Quddus to be part of thesis committee members. Thank for their evaluations, valuable advice and suggestions.

I owe many thanks to Prof. Hugo I. de Lasa (University of Western Ontario) and Prof. Herri Susanto (Bandung Institute of Technology) for their helpful comments and suggestions.

I would also like to thank the financial support provided to this project by both King Abdul Aziz City for Science and Technology (KACST) under research grant number AT-32-67 and Center of Excellence in Nanotechnology (CENT) 2202 funded by Saudi Aramco.

Millions of thanks go to Mr. Iswan Pradiptya and Mr. Tri Bagus Susilo for being my best friend, the support and help their provided, accompanying and kindness.

I am very grateful to Mr. Hendro Setyanto, M.Si. and his wife Mrs. Sri Wakhidah Rahayuningsih, S.Ag., Tiffany Hanik Lestari, and all Imah Noong members for their support and *du'a*.

I also thank to Yusuf, Andy, and all the fellow Indonesian students at KFUPM for their support and affection. Last but not least, I would like to deeply thank Mr. Teguh Kurniawan and Mr. Sagir Adamu for their kind help and assistance in the laboratory.

TABLE OF CONTENTS

LIST OF TABLES

LIST OF FIGURES

LIST OF ABBREVIATIONS

BET	Brunauer–Emmett–Teller
BJH	Barrett-Joyner-Halenda
Btu	British thermal units
CGE	Cold gas efficiency
CREC	Chemical reactor engineering centre
DTG	Differential thermogravimetric
ER	Equivalence ratio
FID	Flame ionization detector
GC	Gas chromatography
GSE	Gasification system efficiency
JCPDS	Joint committee on powder diffraction standards
LHV	Low heating value
OECD	Organization for economic cooperation and development
SEM	Scanning electron microscope
TCD	Thermal conductivity detector
TEOS	Tetraethyl orthosilicate
TG	Thermogravimetric
TGA	Thermogravimetric analysis
TPD	Temperature programmed desorption
XRD	X-ray diffraction

Symbols and Greek letters

G	Gibbs free energy
R	gas constant
T	temperature
nc	number of components
np	number of phases
n_i^k	number of the mole of component i in phase k
g_i^k	chemical potential of component i in phase k
k_{des}	desorption constant
T_m	centering temperature
V_m	amount of ammonia adsorbed at saturation
θ_{des}	fractional surface coverage of the adsorbed species
k_{do}	pre-exponential factor
E_{des}	energy of desorption
T_0	initial temperature
t	heating time
V_{do}	initial values for the desorbed volume
y_i	mole fraction of component i
n_i	number of mole of component i
x_i	conversion of component i
m_i	mass flow rate of component i
Q_i	energy produced or consumed by equipment i

R^2	high correlation coefficient number
β	heating rate
θ	surface coverage

ABSTRACT

Full Name	:	Muflih Arisa Adnan
Thesis Title	:	TAR ELIMINATION IN BIOMASS GASIFICATION -- DEVELOPMENT OF Fe_2O_3/SiO_2-Al_2O_3 FLUIDIZABLE CATALYSTS AND THERMODYNAMIC MODELING
Major Field	:	Chemical Engineering
Date of Degree	:	January 2017

This research deals with the removal of tars from biomass gasification processes. In the regard, both experimental and thermodynamic modeling approach have been considered. In experimental study, iron oxide on SiO_2-Al_2O_3 catalysts are synthesized, characterized and evaluated in a fluidized bed using toluene as a tar model compound. Under the studied reaction conditions, Fe_2O_3/SiO_2-Al_2O_3 yield high toluene conversions (76%). The composition of the gases produced (H_2 (12%), CO (44%), CO_2 (18%) and CH_4 (1%)) are close to their corresponding equilibrium values. The Fe_2O_3/SiO_2-Al_2O_3 catalyst also display stable activities over repeated reaction and re-generation cycles. The presence of Si enhances the stability of the γ-Al_2O_3 support at high temperatures as revealed by TGA, XRD and BET surface area analysis. NH_3-TPD showed that the addition of Fe_2O_3 increase the catalyst acidity, which contributed to the higher tar conversion. Thus, the relatively cheap and unharmful Fe_2O_3/SiO_2-Al_2O_3 catalyst has great potential for industrial applications in tar elimination from biomass gasification processes.

The performance of a gasification process for different biomass is evaluated by developing a thermodynamic model using Aspen Plus. The parametric study is evaluated by varying the gasification temperature, the reformer temperature, the oxygen equivalence ratio, and the steam to carbon ratio. It is found that at same gasification temperature and with no gasifying agent, the increase of H_2/CO ratio of producer gas is proportional to the H/O ratio in the feed biomass. The gasification of algae with oxygen exhibits the highest H_2/CO ratio (0.94). The highest cold gas efficiency is found during gasification of algae with oxygen (0.93) or steam (1.60), while the highest gas system efficiency is obtained for rice husk using the same gasification agents (1.11 or 0.89 with oxygen or steam, respectively).

The thermodynamic model is further developed to take into account of presence of tar in the gasification process. The model shows higher accuracy as compared to the conventional model in term of the composition of producer gas. The parametric study is conducted by varying O_2 equivalence ratio, steam to carbon (S/C) ratio, and split ratio of the gasifying agents through different zones (e.g., combustion zone, counter-current reduction zone, or co-current reduction zone). Introducing the gasifying agents through counter-current reduction zone has positive effect on the gasification performances in term of cold gas efficiency (CGE), gasification system efficiency (GSE), and H_2 and CO concentrations. Gasification with steam exhibits higher H_2 concentration (0.44 at S/C ratio=1) when compared to gasification with oxygen (0.28). In the gasification with oxygen, high CGE (0.79) and GSE (0.94) are observed when ER = 0.3.

ملخص الرسالة

الاسم الكامل	**:**	**مفلح أريسا عدنان**
عنوان الرسالة	**:**	**نزع القطران اثناء تبخير الكتل الحيوية - نماذج ديناميكا حرارية وتطوير مواد حفازة**
التخصص	**:**	**الهندسة الكيميائية**
تاريخ الدرجة العلمية	**:**	**يناير 2017**

تم بنجاح وضع اكسيد الحديد على الالمنيوم المدعم بالسيليكون باستخدام كمية قليلة من المحلول. نتائج الاجهزة ك TGA/DTGو XRD اثبتت بان وجود السيليكون حسن من استقرار اكسيد الالمنيوم (γ-Al_2O_3) عند درجة حرارة مرتفعة. المادة المصنعة (Fe_2O_3/SiO_2-Al_2O_3) تم تسخينها عند 950 درجة مائوية، وامتازت هذه المادة بمساحة سطح عالية قدرت بـ 49 متر مربع لكل واحد جرام. جهاز الـ NH_3-TPD أظهر بان اظافة الحديد يزيد من حموضية المادة المصنعة. صور المجهر الالكتروني (SEM) اكدت الخصائص التكوينية للمواد المحفزة بالنسبة لشكل سطح المادة. التجارب المختبرية باستخدام CREC fluidized Riser Simulator عند عدة درجات حرارة و زمن تفاعل مختلف لهذة المادة المحفزة، أعطى تحول عالي للتولوين. هذة المادة المصنعة لها أسهام قوي في التطبيقات الصناعية علما بانها منخفضة التكلفة وغير ضارة ومستقرة تحت ضروف التشغيل.

اداء عملية تحويل الغاز لكتل حيوية مختلفة تم تقييمها عن طريقة تطوير نموذج ديناميكي حراري باستخدام برنامج " Aspen Plus". في هذه الدراسة تم أخذ كتل حيوية مختلفة لاختبارها مثل الطحالب (N.oculta) و أسعف النخل و الأيكة الساحلية وقشر الأرز. تم دراسة تأثير مكونات الكتلة الحيوية على اداء عملية تحويل الغاز عن طريق احداث تغيير في درجة حرارة عملية تحويل الغاز وجهاز التبخير ومعادلة كمية الاوكسجين و نسبة البخار للكاربون. الدراسة وجدت أنه في نفس درجة التبخير وبدون وجود اي عامل للتبخير أن الزيادة في نسبة الهيدروجين لاول اكسيد الكاربون (H_2/CO) في الغاز المنتج يتناسب تناسبا طرديا مع نسبة الهيدرويجين الى الاوكسين (H/O) في الكتلة الحيوية المراد تبخيرها. فعملية تحويل الطحالب الى غاز بوجود الاكسجين أعطت أعلى نسبة للهيدروجين بالنسبة لاول اكسيد الكاربون (H_2/CO). أعلى كفائة للغاز البارد (كفائة الغاز البارد عبارة عن معدل الطاقة في الغاز المنتج بالنسبة للخام الداخل في العملية) حصل عليها خلال عملية تحويل الطحالب الى بخار في وجود الهواء او بخار الماء، بينمها أعلى كفائة للنظام (كفائة النظام عبارة عن الكفائة الكلية للعملية) حصل عليها من قشور الأرز عند نفس الغازات.

منهاج جديد تم اتباعة لديناميكا عملية تحويل الغاز الى بخار باستخدام برنامج (Aspen Plus) باخذ اعتبار تكوين القطران. النموذج الحالي اظهر دقة عالية مقارنة بالنماذج المعروفة من حيث مكونات الغاز الناتج. عدة عوامل تم دراستها من خلال احداث تغيير في نسبة الغازات المستخدمة مع الكتل الحيوية في ثلاثة أماكن مختلفة (مثل منطقة الاحتراق ومنطقة اختزال ضد اتجاة التيار ومنطقة اختزال مع اتجاة التيار). استخدام الغازات في منطقة اختزال ضد اتجاة التيار له تأثير ايجابي على عملية تحويل الكتل الحيوية الى بخار من حيث كثافة الغاز البارد والنظام ونسبة الهيدروجين الى ثاني اكسيد الكاربون.كذلك تم دراسة تأثير نسبة الاكسوجين ونسبة بخار الماء بالنسبة للكاربون (S/C) على آداء عملية تحويل الكتل الحيوية. ان اضافة بخار الماء يحسن من انتاج الهيدروجين. ان أعلى كفائة للغاز البارد تم ملاحظتها عندما استخدم الاكسوجين كغاز مع الكتل الحيوية في منطقة اختزال ضد اتجاة التيار و 0.3 كنسبة اكسيجين مكافئة.

CHAPTER 1

INTRODUCTION

In recent years, worldwide energy demand is growing at a rapid pace, as a result of the fast economic development [1]. The international energy outlook 2016 predicted that the world energy consumption increased from 549 to 815 quadrillion BTU within eight years (2012 – 2020), as illustrated in Figure 1.1. It is worth noticing that recently the energy demand is still primarily relying on the fossil fuel (82%) [2]. Indeed, the consumption of fossil fuels as a principal energy source causes serious environmental problems such as climate change and acid rain. Attempts to substitute fossil fuels by renewable energy is becoming essential. Biomass is an attractive renewable energy source, given that it is considered as both carbon neutral and having low sulfur content [3, 4]. In addition, biomass is abundantly available in many countries. For instance, Malaysia and Indonesia are producing significant amount of biomass waste per year from the cultivation of palm oil tree [5]. Vietnam, Myanmar, China, India, Bangladesh, and South East Asia have been reported to produce rice husk waste in the massive amounts [6]. Thailand has been listed for its high availability of mangrove trees [7]. Besides availability of biomass, additional advantages can attract the researcher to investigate its use. Recently, there are some research have been focused on microalgae cultivation and processing because of its production with positive environmental impact [8-10].

Biomass as a renewable energy feedstock has been applied to fermentation, direct combustion, pyrolysis and gasification [4, 11]. Gasification is one of the best alternatives

for biomass conversion. Common products species from biomass gasification are permanent gases, tars, unreacted char and inert ash. The gas product contains H_2, CO, CO_2 and CH_4, and is frequently designated as "producer gas". Producer gas offers flexibility, since it can be easily converted into heat, electricity and petrochemical products [12-14].

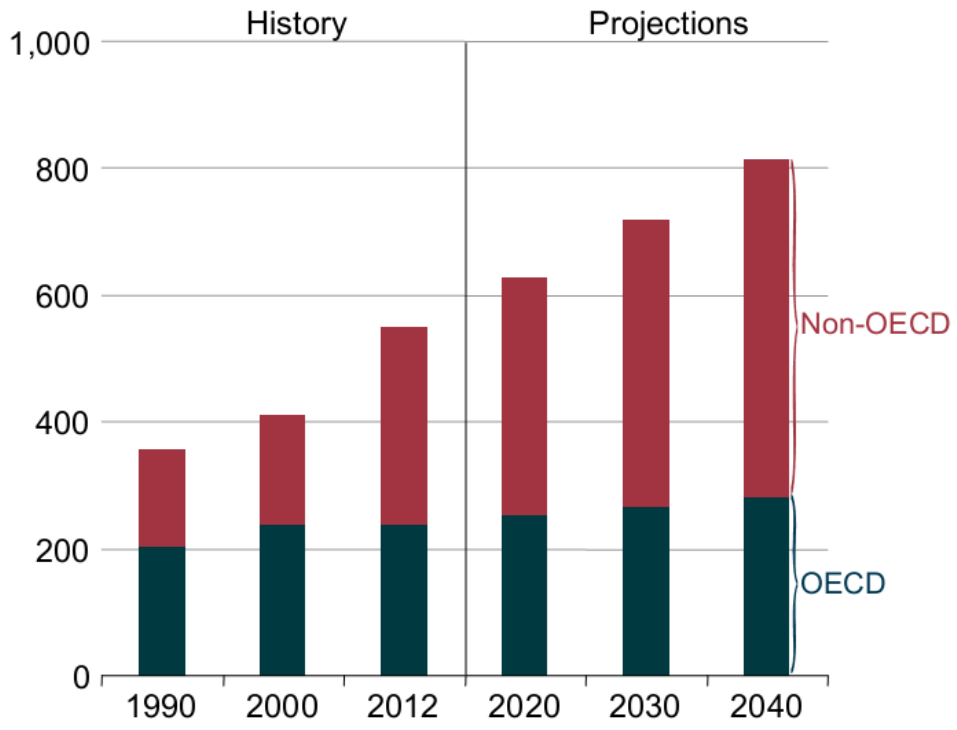

Figure 1.1 World energy consumption, history and prediction (in BTU, OECD: Organization for Economic Cooperation and Development)

To the best of our knowledge, the performance investigation of biomass gasification using various biomasses is not widely studied. Investigation of biomass gasification is mainly focused on only a single type of biomass. For example, Guangul et al. [15] reported that oil palm fronds can be considered as an alternative energy source in Malaysia through gasification using downdraft fixed bed gasifier with air as a gasifying agent. Shahbaz et al.

[5] investigated the air velocity in the fluidized bed gasifier for gasification of palm oil waste. Kook et al. [16] studied the gasification of rice husk by varying the gasifier temperature and equivalence ratio using a bubbling fluidized bed reactor. Loha et al. [17] developed an equilibrium model to study the performance of fluidized bed reactor for rice husk gasification by varying the steam to biomass ratio and the gasification temperature. Zhu et al. [18] studied the gas yield and the bed agglomeration on co-gasification of algae and wood pellets. Kraisornkachit et al. [7] reported the combined gasification process consisting of gasifier, reformer, and CO_2 absorber, to produce a producer gas with high H_2/CO ratio.

The formation of tars is a major issue in biomass gasification. During gasification, tars are mainly produced from the decomposition of lignocellulosic biomass in the pyrolysis stage [19]. The condensation of tars causes operational problems in the downstream gasification units such as in pipes, filters, gas engines, and others [4, 20]. Furthermore, the presence of tars lowers process efficiency, given that condensed tars include aromatic hydrocarbons, with a large contained energy density. Tar composition is affected by many factors such as the gasification operating conditions, type of gasifier used and type of biomass utilized [12, 21-23]. Typically, toluene is the main compound of the tar produced from biomass gasification [12]. Physical, thermal and catalytic tar conversion are the most common processes that are used to eliminate the tars in the producer gas [13, 24, 25].

Catalytic tar conversion is an attractive process for tar conversion, given that the catalytic tar conversion requires low energy [4, 24, 26]. Regarding advances in catalyst design for tar gasification, catalyst performance can be achieved by incorporating an active

catalyst phase on a high surface area support. Gamma alumina (γ-Al_2O_3) has been widely employed as a catalyst support due to its high surface area [27]. However, at high temperatures, the porous structure collapses and is transformed into other alumina forms. In addition, the presence of iron and water vapor can accelerate the transformation of alumina into other phases [28, 29]. This can lead to low surface area with a resulting catalyst deactivation.

However, and through the incorporation of suitable dopants, γ-Al_2O_3 can be stabilized, preventing phase transition and sintering. Moreover, the presence of silica as a dopant in the alumina can improve the stability of the γ-Al_2O_3 at high temperatures [27, 30]. Mardkhe et al. [27] established a one-pot, solvent-deficient method to synthesize silica-doped alumina. The silica acts in this case, as a retardant of the gamma alumina phase transformation. Beguin et al. [29] also reported that the addition of silica on alumina can enhance the thermal stability of the alumina toward sintering in the presence of 20% vol. of water at 1220 ^{o}C.

Taking the above description into account, the research herein has been focused on tar elimination and performance prediction of biomass gasification. The major contribution of this research are as follows:

i. Developed highly active and thermally stable Fe_2O_3/SiO_2-Al_2O_3 catalyst for tar elimination.
ii. Investigated the effect of biomass composition on the performance of biomasss gasification using thermodynamic analysis.
iii. Developed new approach on thermodynamic simulation of gasification process has been conducted using Aspen Plus by considering the formation of tar.

iv. Showed enhanced gasification performance by developing a gasifier configuration using oxygen and/or steam as the gasifying agent.

CHAPTER 2

LITERATURE REVIEW

A considerable volume of experimental and modelling studies have been conducted in order to understand the nature of gasification. This chapter presents the basic theory of biomass, gasification process, tar components, and tar elimination process. As well, the theory of equilibrium reaction is presented in this chapter.

2.1. Biomass

Biomass is referred to organic materials derived from the reaction called photosynthesis, consuming CO_2, water and sunlight to produce carbohydrates molecules, comprising the plant tissues [3]. The biomass consists of many components such as cellulose, hemicellulose, lignin, lipids, water, ash, and other compounds [31]. However, due to the application interest, the characteristic of biomass is generally quantified with the ultimate and proximate analysis [4]. Ultimate analysis represents the elemental composition of the biomass (C, H, O, N, S) in mass fraction, while proximate analysis describes the mass fraction of fixed carbon, volatile matter, moisture, and ash. In addition, it is customary to provide the heating value of the biomass. Biomass is divided into four major types [4]: (1) Energy crops which are especially directed for energy source such as Salix Viminalis and Mischantus X Gigantus, (2) Agricultural wastes such as rice husk and sugar cane fiber, including animal manure, (3) Forestry residues such as logging residues and mill wood waste, and (4) Industrial and municipal wastes such as black liquor from pulp and paper industries.

2.2. Biomass gasification process

Biomass gasification converts solid biomass into a combustible gas mixture which mainly consists of H_2, CO, CO_2 and CH_4 in the presence gasifying agents such as air, oxygen, carbon dioxide and/or steam at high temperature [32, 33]. Biomass gasification process is sequentially divided into three steps such as drying, pyrolysis, and gasification, as shown in Figure 2.1. Initially biomass is heated up to 120^{o}C. The moisture content of the biomass drastically decreased at 120 ^{o}C due to evaporation. When the temperature is increased up to 500 ^{o}C, the biomass cellulose, hemicellulose and lignin are decomposed, producing volatiles and char [4]. The volatiles mainly consists of heavy hydrocarbon and tar, while the char mainly consists of carbon [34]. This step is called pyrolysis. After pyrolysis, the remaining char is gasified at 500 – 900 ^{o}C with the presence of gasifying agents [4, 35]. In general, gasification involves numerous complex chemical reaction which are summarized as follows [19].

Partial oxidation	$C + ½ O_2 \leftrightarrow CO$	ΔH^0_{298} = –111 MJ/kmol	(2.1)
Boudouard reaction	$C + CO_2 \leftrightarrow 2CO$	ΔH^0_{298} = +172 MJ/kmol	(2.2)
Steam reforming	$C + H_2O \leftrightarrow CO + H_2$	ΔH^0_{298} = +131 MJ/kmol	(2.3)
Methane formation	$C + 2H_2 \leftrightarrow CH_4$	ΔH^0_{298} = –74MJ/kmol	(2.4)
Water gas shift reaction	$CO + H_2O \leftrightarrow CO_2 + H_2$	ΔH^0_{298} = –42 MJ/kmol	(2.5)
Methane reforming	$CH_4 + H_2O \leftrightarrow CO + 3H_2$	ΔH^0_{298} = +206 MJ/kmol	(2.6)
CO_2 reforming	$CH_4 + CO_2 \leftrightarrow 2CO + 2H_2$	ΔH^0_{298} = +247 MJ/kmol	(2.7)

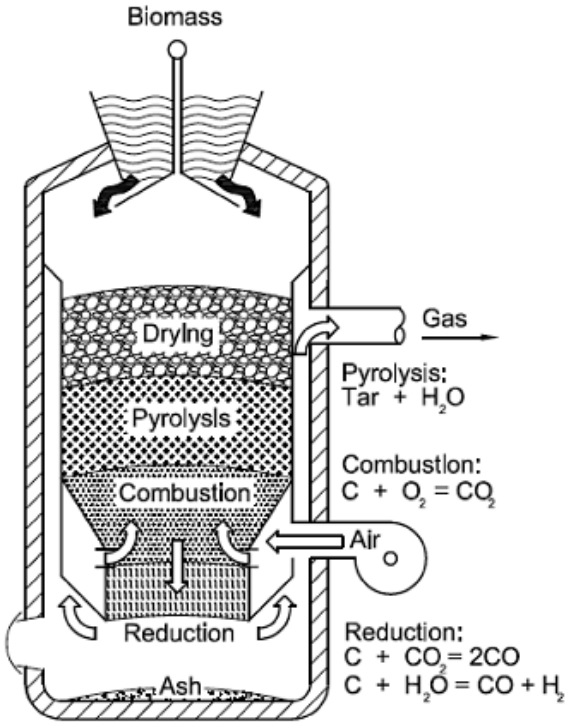

Figure 2.1. Schematic diagram of gasification process [4].

The type of gasification reactor, called gasifier, is classified according to the fluidization regime in the gasifier. Recently, three typical designs of gasifier such as fixed bed, fluidized bed and entrained-flow has been widely used for industrial application. In the fixed-bed gasifier (sometimes it is called moving-bed gasifier), the feedstock moves slowly downward by the gravity as it is gasified (see Figure 2.2a). The fixed-bed gasifier is classified into updraft gasifier and downdraft gasifier according to the flow direction of the gasifying agent [36]. The fluidized bed gasifier show high efficiency due to the good mixing of biomass feedstock and the gasifying agent which result in the uniform composition and temperature inside the gasfier, as shown in Figure 2.2b [37]. In the entrained-flow gasifier, the pulverized feedstock is fed along with the gasifying agent in co-current flow (see Figure 2.2c). The entrained-flow gasifier requires high temperature

since residence time in the gasifier is short (in order of seconds) [36]. The specification and the diagram of these three reactors is presented in Table 2.1 and Figure 2.2, respectively.

Table 2.1. Comparison of some commercial gasifiers [38].

Parameters	**Fixed-bed**	**Fluidized-bed**	**Entrained-bed**
Feed size	<51 mm	<6 mm	<0.15 mm
Feedstock tolerance	Low-rank coal	Low-rank coal and excellent for biomass	Any coal but unsuitable for biomass
Tolerance for coarse	Very good	Good	Poor
Tolerance for fines	Limited	Good	Poor
Steam requirements	High	Moderate	Low
Oxidant requirements	Low	Moderate	High
Cold-gas efficiency	80%	89%	80%
Application	Small capacities	Medium capacities	Large capacity

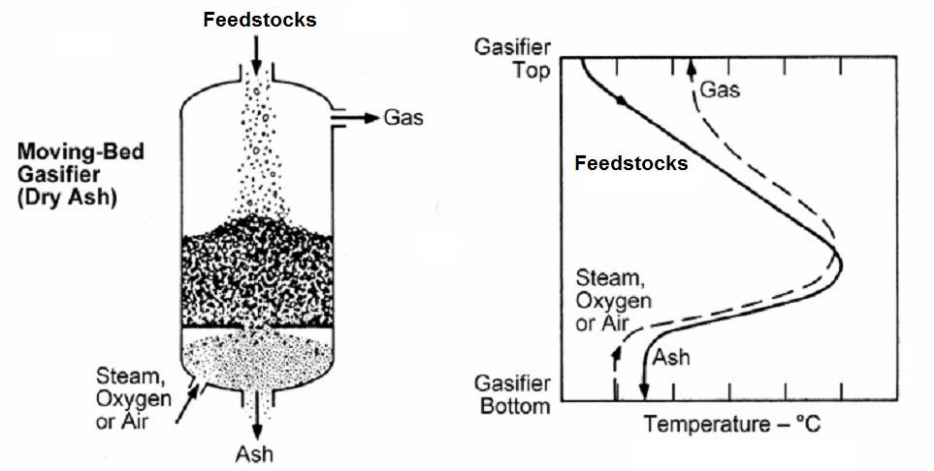

(a)

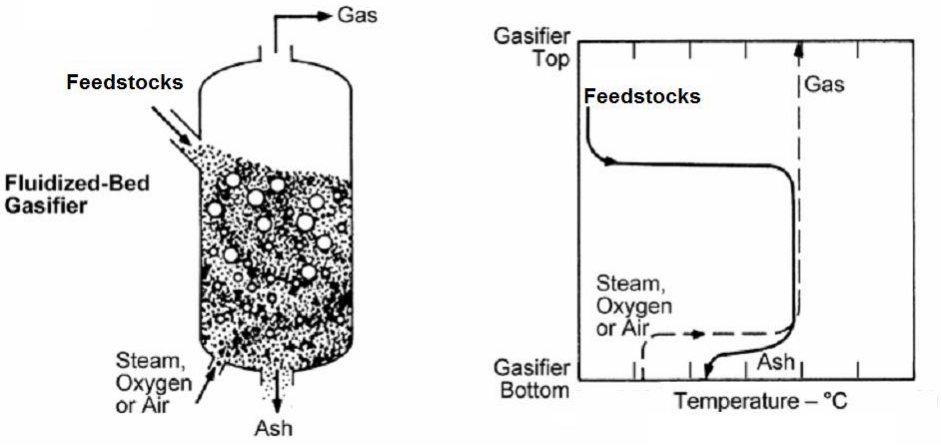

(b)

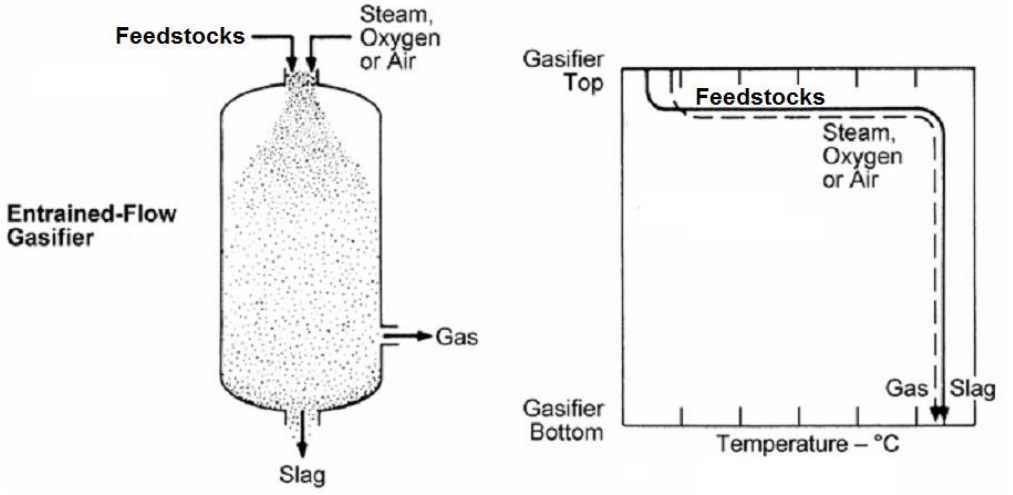

(c)

Figure 2.2. Diagram of (a) fixed-bed gasifier, (b) fludized-bed gasifier and (c) entrained-flow gasifier [39]

Some parameters such as gasifying agent and operating condition greatly influence the gasification process. The use of pure oxygen as gasifying agent provides producer gas with higher heating value as compared to air as a gasifying agent due to low N_2 concentration. Gasification with steam produced the producer gas with high H_2 concentration since steam is playing the role as the hydrogen source for gasification [40-42]. Some recent studies reported the use of CO_2 offers some advantages such as high carbon conversion and less CO_2 emission [43]. However at atmospheric pressure, CO_2 addition has no positive influence on the gasification [44].

Gasification temperature is an important factor that influences the composition of producer gas. Some studies reported the tar yield was decreased and H_2 content increased with the increasing of temperature [45, 46]. Higher temperature can produce producer gas with high H_2 and CO content because the higher temperature enhance the endothermic water gas reaction and can effectively decompose the tar into light gaseous product [12]. In the case of biomass gasification with steam, producer gas with higher H_2/CO ratio was obtained from higher gasification temperature since the higher temperature enhance the endothermic water gas reaction [47].

2.3. Tar components

Tar is defined as a mixture of hydrocarbons including single-ring to 5-ring aromatic compounds, and also oxygen-containing hydrocarbon [48]. Tars are formed in the pyrolysis step in the presence of limited oxygen through a series of complex reactions [49]. The composition and amount of tar in the producer gas depends on many factors such as operating conditions, biomass type, gasifying agent and type of gasifier [12, 25, 50, 51].

However, temperature has significant effect on the tar composition, as shown in Figure 2.3. The organic compounds become more stable at higher temperature [12]. One should notice that tar problem is not mainly caused by the tar quantity, but it is also affected by the properties and the composition of tars [49]. Based on the appearance, tar can be classified into three classes as shown in Table 2.2.

Due to the complexity of the actual tar, in order to understand the nature of tar cracking in a simple way, some researchers used toluene (C_7H_8) as a tar model [52-54], since it is one of the major composition in tar from biomass gasification (See Figure 2.4) [12]. Toluene is an aromatic hydrocarbon consisting of a CH_3 group attached to a phenyl group, as shown in Figure 2.5.

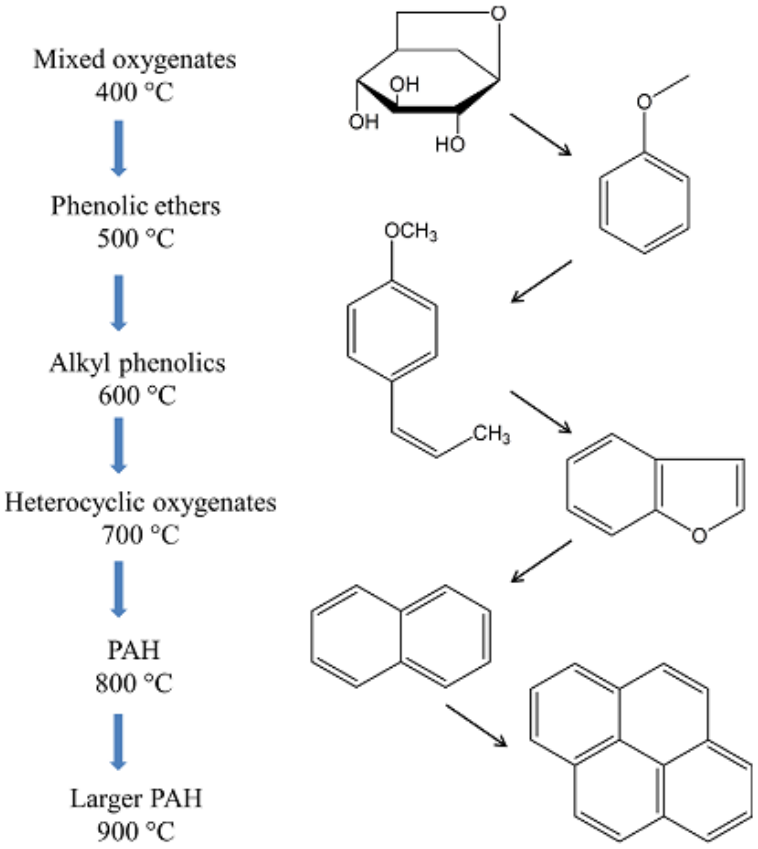

Figure 2.3. Tar maturation scheme [12]

Table 2.2. Tar classification based on the appearance

Classification	Example
Primary	Levoglucosan, furfural and hydroxyacetaldehyde
Secondary	Phenol, cresol and xylene
Tertiary	Benzene, naphthalene and toluene

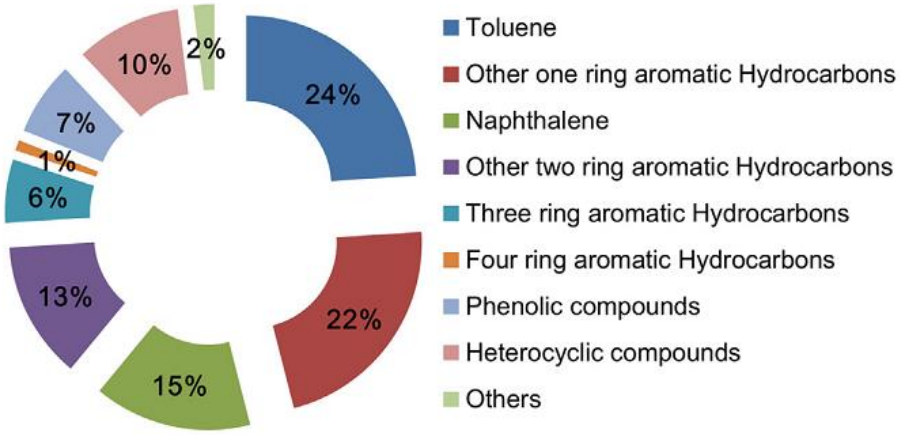

Figure 2.4. Typical tar composition of biomass tars [12]

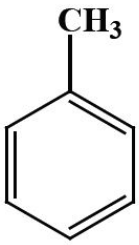

Figure 2.5. Structure of toluene.

2.4. Tar elimination

A considerable volume of literatures have reported various methods for tar reduction. It is worth noticing that the methods are favorable when one meets the following requirements: (1) efficient in term of operation, (2) economically attractive, and importantly (3) should not have negative effects on the producer gas [55]. The methods are generally categorized as primary method (i.e., inside the gasifier) and secondary method (i.e., outside the gasifier). The concept of primary method is preventing and/or eliminating the presence of tar in the gasifier by several approaches such as (1) selection of proper operating parameters [55], (2) use of catalysts [41], and (3) gasifier modifications [25, 56]. The secondary method or also called as downstream gas cleaning can be done by mechanical methods (e.g., cyclone, filters, and scrubber) and tar cracking of downstream process through thermal cracking or catalytic cracking [55].

In the case of thermal cracking of tar, the tar is eliminated at high temperature. Considerable volume of literatures reported that thermal cracking of tars occurs at temperatures higher than 700 ^{o}C. Indeed, the higher operating temperatures yields lower tar content [57]. For example, El-Rub et al. [58] reported that phenol as a tar surrogate is stable when the pyrolysis at 700^{o}C. However, when the temperature was increased up to 800^{o}C, the phenol conversion improved up to 97wt%. Phuphuakrat et al. [59] observed the effect of temperature on the conversion of tar from Japanese cedar. In their study, a reduction of 78% tar (measured using gravimetric mass) was observed when the temperature was increased from 600 ^{o}C to 800 ^{o}C. Zanzi et al. [60] reported that the tar yield from pyrolysis of birch wood significantly reduced from 1.1 to 0.2 wt% maf (moisture ash free) when the temperature was increased from 800 to 1000^{o}C. In other literature, Zanzi

et al. [60] also reported that the tar yield from the pyrolysis of mixture of aspen (10%) and birch (90%) reduced from 1.2 to 1.1 wt% maf if the temperature was elevated from 750 to 900^{o}C.

Attempts in tar reduction by gasifier modification has been reported by some researchers [55]. Pan et al. [61] observed the effect of secondary air injection on tar contents using fluidized-bed gasifier at temperature range 840–880 ^{o}C. The addition of secondary air just above the feeding point with a ratio of primary air to secondary air of 20% can reduce tar up to 88.7wt%. Brandt et al. [62] designed a two-stage gasifier which consists of a pyrolysis unit, two gasification units (i.e., gasification unit and char gasification unit), with the capacity of 100 kW (see Figure 2.6). In their study, the pyrolysis products (i.e., char and volatiles) entered the top of the gasification unit. Indeed, the mixture of air and steam was injected into the gasification unit to promote partial oxidation reaction. Then, the char was sent to the char gasification unit and however the gases passed through the bed of unreacted char, producing a producer gas with tar content of 15 mg/m^3. Susanto et al. [25] developed a co-current moving bed gasifier with internal recycle of pyrolysis gas (see Figure 2.7). The basic concept of this sophisticated design is producing high temperature combustion zone, and sending the tar from pyrolysis stage into the combustion zone. In this gasifier, the biomass was pyrolysed in the pyrolysis zone. The volatiles were mixed with the air and burnt in the combustion zone while the char was sent to the gasification zone. The flue gas from the combustion zone acted as a gasifying medium in the gasification zone. A clean gas producer with tar content of 48 mg/Nm^3 was produced from this design since all tars from the pyrolysis zone must pass through the hot flame in the combustion zone.

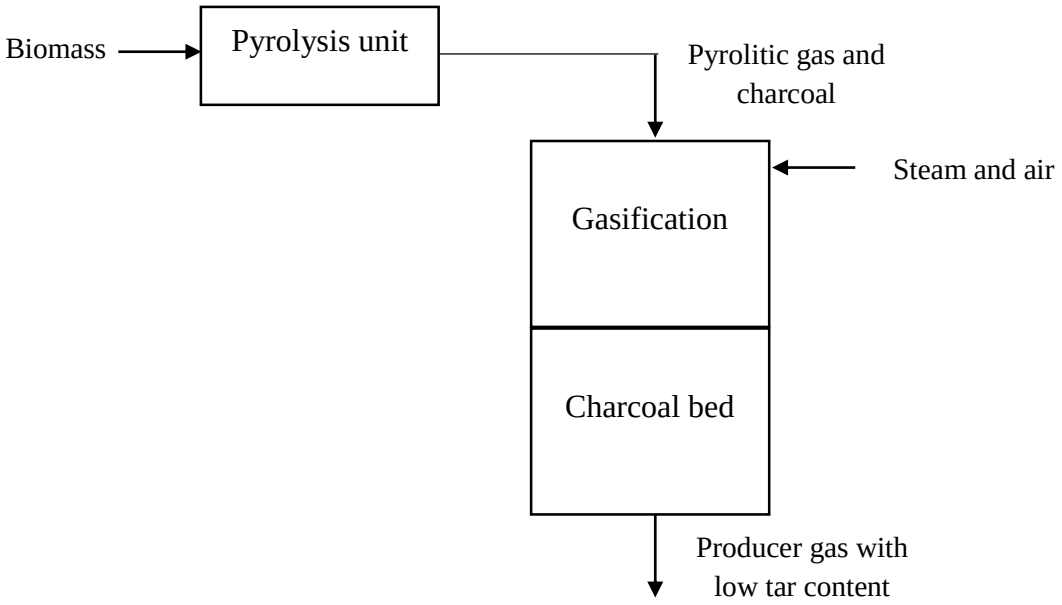

Figure 2.6. Two stage gasifier by Technical University of Denmark [62]

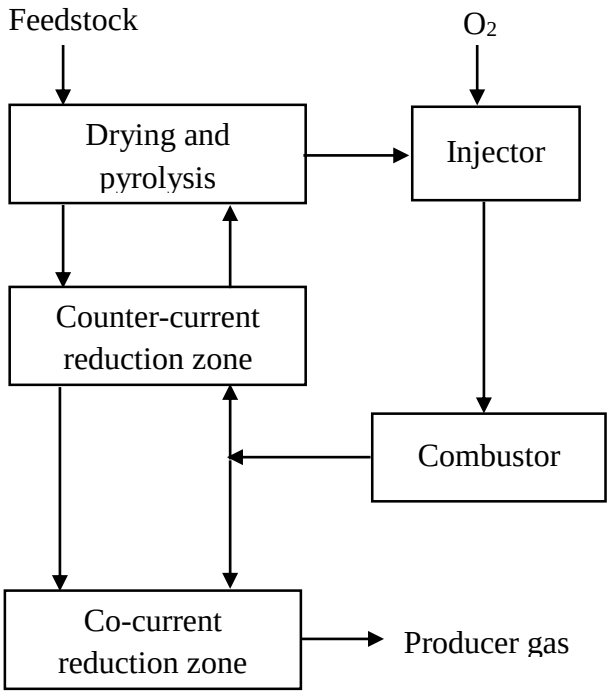

Figure 2.7. Downdraft gasifier with internal recycle by Susanto et al. [25]

For the purposes of tar catalytic cracking, the catalysts should display (1) high catalytic activity, (2) high resistance to carbon deposition and sintering, (3) the ability to withstand harsh process conditions, (4) the capability of methane reforming in order to produce syngas, and (5) cost effective [63]. It is worth noting that catalyst is divided into three main components: (1) an active catalytic phase or metal, (2) a dopant or promoter, and (3) high surface area support.

Tar cracking involves numerous complex heterogeneous reactions. The following reactions are hypothesized involved in tar elimination [13].

Steam reforming	C_pH_q (tar) + $pH_2O \longleftrightarrow pCO + (p + q/2)H_2$	(2.8)
Dry reforming	$C_pH_q + pCO \longleftrightarrow 2pCO + (q/2)H_2$	(2.9)
Thermal cracking	$C_pH_q \longleftrightarrow C^* + C_xH_y$ (smaller tar) + gas	(2.10)
Hydrocracking or hydroreforming of tars	$C_pH_q + H_2 \longleftrightarrow CO + H_2 + CH_4 + \ldots +$ coke	(2.11)

The basic catalytic mechanism of the steam reforming of tar is the dehydrogenation of hydrocarbon components in tar on the active sites of catalysts whereas the carbon could be formed on the same sites. However, the deposited carbon could further reacts with steam to generate additional CO and maintains the catalysts activity [12].

The catalysts for tar conversion can be categorized in two types based on the location where the catalytic reaction of tar conversion occurs; either directly employed in the gasifier (primary catalyst) or in the particular reactor outside the gasifier (secondary catalyst). The presence of active materials in the gasifier prevent the tendencies of solid agglomeration on the reactor wall. However, catalyst in the gasifier may be affected by deactivation due to carbon deposition on the catalyst surface [4]. Secondary catalysts are attractive for tar conversion in hot producer gas [64]. Dolomite, olivine, alkali metals and

transition metals showed promoting several chemical reaction in tar conversion either as primary catalyst or secondary catalyst [4].

Concerning catalysts for tar conversion, olivine and dolomite are possible choices given their thermal and mechanical stability, and their good cracking activity. However, these natural minerals require relatively high reaction temperatures (above 850 °C) to achieve significant tar conversions. For instance, at 750 °C, tar conversion is limited to 21%. As well, the specific surface area of these natural minerals is very low (<0.5m^2/g) [65]. Virginie et al. [52] examined the catalytic activity of olivine for toluene steam reforming. The toluene conversion using olivine was only 30% at 900 ^oC. Devi et al. [65] investigated the performance of olivine for tar cracking with naphthalene as a tar model. These authors reported that at 900 ^oC, there was a 81% naphthalene conversion for calcined olivine compared to a 48% naphthalene conversion for untreated olivine.

A Fe-based catalyst is a cost effective and relatively unharmful material and this when compared to other metals such as Ni, Cu, Mo and Co [66]. Virginie et al. [52] investigated the catalytic steam reforming of toluene using iron supported on olivine with various iron loadings. It appears that the iron oxide (hematite) on olivine has positive effects on toluene conversion. However, the high conversion of toluene (90%) could only be reached at 850 ^oC.

Fe-based catalysts, loaded with iron in their metallic form have also been reported as promising for tar decomposition, given their hydrocarbon cracking and water-gas shift reactivity [52, 67, 68]. Nordgreen et al. [69] studied the gasification of birch feedstock using a commercial iron catalyst purchased from *Höganäs* AB. In their study, naphthalene conversion on metallic iron catalysts was 40% at 850 ^oC [20].

2.5. Equilibrium reaction

The non-stoichiometric equilibrium approach, by means minimization of Gibbs free energy, can be used for thermodynamic modeling of gasification process [70]. Many literatures reported that the Gibbs minimization approach provides good accuracy compared to experimental result [43, 71, 72]. However, in some cases, the modifications of the equilibrium model is required in order to approach the experimental results [73].

Numerous studies have investigated the biomass gasification using thermodynamic analyses. The minimization of Gibbs free energy is a non-stoichiometric equilibrium approach, which has been widely used for thermodynamic analysis on gasification process [7, 74]. Several thermodynamic studies were conducted with negligible tar presence. To cite a few, Renganathan et al. [75] investigated of carbonaceous feedstock gasification using CO_2, steam, and O_2 as gasifying agents. Chaiwatanodom et al. [72] studied the performance of the biomass gasification with recycled CO_2. Krainsornkachit et al. [7] evaluated the performance of different combined systems of biomass gasification, which consist of a gasifier, a reformer, and a CO_2 recycle. On other hand, only few researchers have taken tar into account in their gasification model. For instance, Gopaul et al. [76] used char as tar model in their study of the chemical looping gasification for hydrogen production. Mostavi et al. [77] calculated the yield of tar, as a function of temperature, based on the empirical equation proposed by Fagbemi et al. [34]. These authors assumed tar to be formed of cyclic hydrocarbons such as $C_3H_6O_2$, C_6H_6O, C_7H_8, and $C_{10}H_8$.

A system is considered to be at equilibrium condition if the total Gibbs free energy (G) is minimum. The composition of each compound is calculated by minimizing the objective function G. The dimensionless G/RT is shown as follow [78].

$$\frac{G}{RT} = \sum_{k=1}^{np}\left(\sum_{i=1}^{nc} n_i^k\right) g_i^k \tag{2.12}$$

G, *R* and *T* represents total Gibbs free energy, gas constant and temperature, respectively. Number of components and number of phases are assigned as *nc* and *np*, respectively. n_i^k and g_i^k are assigned to the number of the mole and the chemical potential of component *i* in phase *k*, respectively. In addition, minimization of total Gibbs free energy must satisfy the mass balance of elements, as shown below.

$$\sum_{k=1}^{np} n_i^k = z_i F \vdots \qquad i = 1, 2, 3, ..., nc \tag{2.13}$$

$$0 \le n_i^k \le z_i F \vdots \qquad i = 1, 2, 3, ..., nc \tag{2.14}$$

2.6. Summary of the review

The review of many published literatures concludes that the biomass gasification is an attractive process to convert the biomass into useful energy. The fluidized-bed gasifier is the best reactor configuration for catalytic biomass gasification. However, the formation of tar during biomass gasification is a major problem since the condensation of tars in the proceeding equipment may severely disturb the process. The summary of the literature review is mentioned as follow.

a. Tar from biomass gasification can be removed by selecting proper operation conditions, adding catalysts in the process, or modifying the gasifier.
b. The catalytic tar conversion is an attractive conversion process since the catalytic tar conversion process requires low energy.

c. A Fe-based catalyst is a cost effective and relatively unharmful material and this when compared to other metals such as Ni, Cu, Mo and Co.

d. The addition of silica on alumina has been reported can stabilize the textural properties of alumina with the presence of water and iron at high temperature.

e. Many literatures have reported the performance of iron oxide at high reaction temperature ($\geq$850 ^{o}C), as shown in Table 2.3. However, few studies conducted at moderate temperature (400–600 ^{o}C).

f. The minimization of Gibbs free energy approach can provides results in close agreement with their experimental counterparts

g. Only few investigation reported the effect of biomass composition on the performance of biomass gasification, as shown in Table 2.4.

h. A limited volume of literatures reported the thermodynamic model of biomass gasification with taking tar formation into account, as shown in Table 2.5.

Table 2.3. Summary of the published research on the catalyst for tar cracking.

Support/ natural mineral	Active metals	Tar/tar model	Reaction Temperature	Conversion	Reference
Olivine	-	Toluene	900^{o}C	30%	Virginie et al. [52]
Calcined olivine	-	Naphthalene	900^{o}C	81%	Devi et al. [65]
Untreated olivine	-	Naphthalene	900^{o}C	48%	Devi et al. [65]
Olivine	Iron oxide	Toluene	850^{o}C	90%	Virginie et al. [52]
-	Metallic iron	Tar from birch	850^{o}C	60%	Nordgreen [69]
Al_2O_3	Iron oxide	Gasification of cedar sawdust	850^{o}C	High gas yield	Uddin et al. [23]

Table 2.4. Summary of the published research on performance of biomass gasification

Biomass	Aim of the study	Reference
Palm oil fronds	The performance of gasification using downdraft fixed bed gasifier with air as a gasifying agent	Guangul et al. [15]
Palm oil waste	The air velocity in the fluidized bed gasifier for gasification	Shahbaz et al. [5]
Rice husk	The gasifier temperature and equivalence ratio using a bubbling fluidized bed reactor	Kook et al. [16]
Rice husk	The performance of fluidized bed reactor by varying the steam to biomass ratio and the gasification temperature using equilibrium model	Loha et al. [17]
Algae and wood pellets	The gas yield and the bed agglomeration on co-gasification	Zhu et al. [18]

Table 2.5. Summary of the published research on thermodynamic modelling of biomass gasification

Tar compound	Aim of the study	Reference
Neglected	Investigation on the carbonaceous feedstock gasification using CO_2, steam, and O_2 as gasifying agents.	Reganathan et al. [75]
Neglected	Examination of the performance of the biomass gasification with recycled CO_2	Chaiwatanodom et al. **[72]**
Neglected	Evaluation of the performance of different combined systems of biomass gasification, which consist of a gasifier, a reformer, and a CO_2 recycle.	Krainsornkachit et al. **[7]**
Char and tar are modelled as pure carbon	Investigation on the chemical looping gasification for hydrogen production	Gopaul et al. **[76]**
Tar is modelled as $C_3H_6O_2$, C_6H_6O, C_7H_8, and $C_{10}H_8$	Simulation of woody biomass gasification using steam with dry sorption CO_2 capture	Mostavi et al. **[77]**

CHAPTER 3

THESIS OBJECTIVES

This Thesis encompasses with three main objectives concerning biomass gasification including: (1) development of highly active and stable Fe_2O_3/SiO_2-Al_2O_3 catalysts suitable for catalytic cracking toluene (a model compound as tar), (2) thermodynamic study on the gasification process using various biomass, and (3) new approach on thermodynamic simulation of gasification process including tars.

The experimental study on catalytic toluene steam reforming using Fe_2O_3/SiO_2-Al_2O_3 catalysts is conducted to understand the effect of the iron oxide catalyst on tar cracking at moderate reaction temperatures (400 – 600^oC). The specific objectives are as follows:

i. To evaluate the effects of calcination temperatures on the textural properties and stability of Fe_2O_3/SiO_2-Al_2O_3 catalysts,
ii. To study the effects of iron loadings on the textural properties and stability of the catalysts,
iii. To investigate the effect of iron loading on the activity and product selectivity of the iron oxide catalysts,
iv. To study the effect of reaction temperature and reaction time on the conversion and product selectivity,

The thermodynamic study of a set of gasification process using various biomass is developed to investigate relation between biomass composition and the quality of the

producer gas in order to obtain a preliminary estimation for the application of biomass gasification. The specific objectives are as follows:

i. To study the effect of gasification temperature on the producer gas composition and performance of the gasification process,
ii. To study the effect of reformer temperature on the producer gas composition and performance of the gasification process,
iii. To study the equivalence ratio on the producer gas composition and performance of the gasification process,
iv. To study the steam to carbon ratio on the producer gas composition and performance of the gasification process,

A new approach to model a downdraft gasifier is developed by considering the formation of tar using the ubiquitous process simulator: Aspen Plus. The present model is adapted from the one developed by Susanto and Beenackers [25], which proved impeccable for the solution of tar formation problem. The specific objectives are as follows:

i. To enhance the gasifier performance in term of composition of H_2 and CO, cold gas efficiency, and gasification system efficiency, the oxygen and mixture of oxygen and steam as the gasifying agents are introduced to the gasifier.
ii. To investigate the effect of the injection of gasifying agents through the three different zones such as combustion zone, counter-current reduction zone, and co-current reduction zone.
iii. To study the effect of the O_2 equivalence ratio and steam to carbon ratio on the performance of gasification process.

CHAPTER 4

METHODOLOGY

4.1. Experimental work on supported iron oxide catalyst

4.1.1. Material

Tetraethyl orthosilicate (TEOS) (liquid, 99.9%), and iron (III) nitrate nonahydrate (granular, 98%) were purchased from Sigma-Aldrich. Aluminum isopropoxide (granular, 98%) was purchased from Acros Organics.

4.1.2. Synthesis method

Catalyst synthesis was developed by closely following the method proposed by Mardkhe et al [27]. For instance, the water was added to the aluminum isopropoxide using a 1:5 mol ratio. This was followed by adding immediately 15wt% silica in the form of tetraethyl orthosilicate (TEOS), water to the TEOS at a 2:1 mol ratio and 5wt% iron in the form of iron (III) nitrate nonahydrate. These reagents were mixed for 20 min. The precursor was then calcined for 2 h using a temperature ramp rate of 2 ^{o}C/min up to 750 °C.

Codes for the prepared catalysts are as follows: a) first, the weight percent of Fe, b) second, the ISA acronym for iron silica alumina, c) third, the weight percent of Si in between brackets and d) finally, the calcination temperature. Thus, for a sample consisting of 5wt% Fe, 15wt% Si and calcined at 750 ^{o}C, the designation is 5-ISA(15)-750.

4.1.3. Catalyst characterizations

Thermal stability

The thermal stability of the catalyst was tested using thermogravimetric analysis (TGA) SDT Q600. The mass loss of the sample was measured as the temperature was increased using a constant heating rate of 10 ^{o}C/min. The temperature range covered was 25 – 1000 ^{o}C with the catalyst sample being under a 10 mL/min N_2 flow.

Phase composition

X-ray diffraction patterns of the catalyst samples were acquired using a Rigaku MiniFlex Diffractometer using Ni filtered Cu Kα radiation. The samples were scanned at every 0.03^{o} from 10 to 90° in the 2θ scale with a scan time constant of 2^{o}/min. The diffraction spectra have been indexed by comparing these with the Joint Committee on Powder Diffraction Standards (JCPDS) files.

Textural properties

The catalyst textural properties such as specific surface area, average pore sizes and pore volumes of the catalysts were obtained on a Micromeritics ASAP 2020 Analyzer using N_2 adsorption at 77 K. Prior to the analyses, each sample (0.2 – 0.3 g) was prepared by degassing at 300 ^{o}C for 2.5 h. The N_2 adsorption-desorption isotherm was recorded over a relative pressure (P/P_0) range from 0 to 0.99.

Acidity study

The acid site density and acid site strength on the catalyst surface were measured using ammonia temperature programmed desorption (TPD). A Micromeritics Autochem II 2920 Analyzer was used to determine ammonia TPD. Prior to the measurements, catalysts were brought to saturation by flowing a stream of gas containing 5% NH_3 in Helium at 50

^{o}C for 1 hr. After saturation, the amount of ammonia released from the sample was measured at the temperature range of 50 – 750 ^{o}C with a heating rate of 10^{o}C/min

Scanning Electron Microscope

The surface morphology of the catalysts prepared were observed using a MIRA3 Tescan Scanning Electron Microscope (SEM). To avoid catalyst modification during SEM analysis, catalysts were coated with a conductive carbon film. Then, the SEM analysis was run using an accelerating voltage of 20 kV. The working distance was 13.55 mm.

4.1.4. Catalytic steam reforming of tar in a CREC Riser Simulator

The activity of the prepared catalysts for toluene steam reforming was evaluated in a CREC Riser Simulator. The CREC Riser Simulator is a laboratory scale mini-fluidized bed reactor that is particularly valuable for catalyst testing under the operating conditions close to those of industrial-scale fluidized bed reactors Figure 4.1 provides a schematic of the CREC Riser Simulator. Additional specifications of CREC Riser Simulator can be found in de Lasa [79].

A 0.3 g of fluidizable catalyst with three different iron loadings (5wt%, 10wt% and 15wt%) was used in the toluene conversion experiments. Toluene steam reforming runs were carried out at different temperatures, ranging from 400 to 600 ^{o}C, while the reaction time was varied in the 10 – 25 sec range.

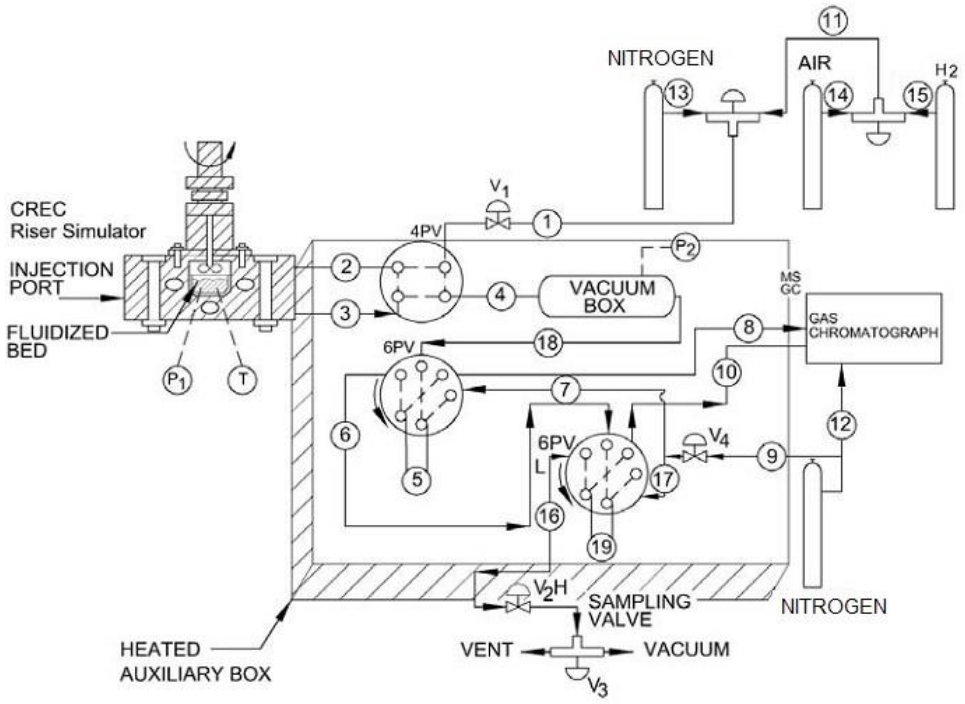

Figure 4.1. Schematic Diagram of the CREC Riser Simulator and its Accessories. The 4PV permits: i) the isolation of the reactor for gasification to take place (when lines 2-3 are connected) and ii) reactor evacuation (when lines 3-4 are connected). The two 6PVs allow: i) loading sampling loops 5 and 19 with the lines 18-5-6 and 6-19-16 being connected, and ii) directing the sample to the capillary and packed bed column of the GC system through the connection of 7-5-8- and 17-19-10 lines, respectively.

At the beginning of the run, the catalyst was loaded into the catalyst basket with porous grids placed both at the top and at the bottom of the basket. Prior to the reaction, the reactor was adequate reactor operation was checked for leaks. Once this operation completed, the temperature in the 50mL reactor was raised gradually under a nitrogen atmosphere to the desired reaction temperature. Then, the water and toluene were fed to the reactor using a syringe. During the injection, the pressure inside the reactor was increased up to 55 psi (380 kPa). When the desired reaction time was reached, products were quickly evacuated from the reactor to the vacuum box. This was achieved given the pressure in the 1 liter vacuum box was typically set at 3 psi (21 kPa) prior to evacuation.

During experiments, temperature in the vacuum box was held at around 180 °C. This prevented condensation of unreacted toluene. After product evacuation from the reactor, N_2 was injected into the vacuum box. Reaction products and the N_2 were carefully mixed for 2 min in the vacuum box and transferred to a GC Agilent 7890A unit for analysis. Gas product species such as H_2, CO_2, CO and CH_4 were analyzed using Thermal Conductivity Detector (TCD) while the toluene was analyzed by a Flame Ionization Detector (FID). Catalysts were regenerated by flowing the air for 10 min and this to combust the carbon formed on the catalyst. All runs were repeated with the same procedure at least three times, and this to secure the reproducibility of the results. The performance of the catalysts was evaluated in terms of dry gas composition (CO, CO_2, H_2 and CH_4) and the toluene conversion, as follows:

$$x_{Toluene}(\%) = (n_{Toluene\ in} - n_{Toluene\ out})/n_{Toluene\ in} \quad (4.1)$$

$$y_i = \frac{n_i}{\sum n_i} \quad (4.2)$$

where *i* represents H_2, CO, CO_2 and CH_4.

4.2. Thermodynamic study of gasification using various biomasses

4.2.1. Process description

The gasifying agent (oxygen and steam) and biomass feedstock were fed separately to the gasifier. The raw producer gas from gasifier was then sent to a cyclone in order to remove the unreacted carbon (char) and ash. The obtained clean producer gas was fed to a reformer unit to improve the quality of producer gas by promoting both the CO_2 reforming and the methane reforming reactions. After the reformer unit, the producer gas was sent to a CO_2 absorber unit (with an assumed 90% CO_2 removal efficiency). The pure CO_2 from

the absorber was cooled to 150°C, while the producer gas was cooled to 25°C. In general, gasification involves a set of complex chemical reactions which are summarized below [7].

Partial oxidation	$C + ½ O_2 \leftrightarrow CO$	ΔH^0_{298} = –111 MJ/kmol	(4.3)
Boudouard reaction	$C + CO_2 \leftrightarrow 2CO$	ΔH^0_{298} = +172 MJ/kmol	(4.4)
Steam reforming	$C + H_2O \leftrightarrow CO + H_2$	ΔH^0_{298} = +131 MJ/kmol	(4.5)
Methane formation	$C + 2H_2 \leftrightarrow CH_4$	ΔH^0_{298} = –74MJ/kmol	(4.6)
Water gas shift reaction	$CO + H_2O \leftrightarrow CO_2 + H_2$	ΔH^0_{298} = –42 MJ/kmol	(4.7)
Methane reforming	$CH_4 + H_2O \leftrightarrow CO + 3H_2$	ΔH^0_{298} = +206 MJ/kmol	(4.8)
CO_2 reforming	$CH_4 + CO_2 \leftrightarrow 2CO + 2H_2$	ΔH^0_{298} = +247 MJ/kmol	(4.9)

4.2.2. Simulation system

The non-stoichiometric equilibrium approach, by means of the minimization of Gibbs free energy, can be used for thermodynamic modeling of gasification process [70]. Many papers report that the Gibbs minimization approach provides results in close agreement with their experimental counterparts [43, 71, 72]. In this study, a thermodynamic simulation of biomass gasification was conducted using the Aspen Plus software. Biomass was defined as a nonconventional component in Aspen Plus, while gaseous products and solid carbon were defined as mixed component and cisolid component, respectively. Therefore, MIXCINC stream class were selected in this simulation. Additional information related to the Aspen Plus simulation are summarized in Table 4.1.

Table 4.1. Input attributes in the Aspen.

Input	Attributes
Thermodynamic packages	Peng-Robinson
Phase system	Vapor-liquid
Stream class	MIXCINC
Input mode	Steady-state
Enthalpy	HCOALGEN (code 6)
Density	DCOALIGT

The gasifier was developed using two blocks (RYield and RGibbs) that produce the producer gas. An external FORTRAN code (defined using a calculator block) is embedded in RYield to decompose the biomass (nonconventional component) into C, H_2, O_2, N, and S elements (mixed component) based on the ultimate and proximate analysis. The product of the RGibbs block were limited to O_2, H_2, CO, CO_2, CH_4 and C (pure solid). The cyclone block was used to remove ash and unconverted carbon (char). A reformer reactor was used to upgrade the producer gas and was modelled using the REquil block. Two reactions: CO_2 reforming and CH_4 reforming were assumed to occur in this reformer. An ideal CO_2 absorber (with a 90% CO_2 removal) was defined using external Ms. Excel subroutine in the calculator block. The pure CO_2 from the absorber was vented after cooling to 150^{o}C. Figure 4.2 depicts the block flow diagram of gasification process. The producer gas exiting the CO_2 absorber was cooled to 25^{o}C by using cooler block. The results of our simulations agree closely with the findings of other authors [72, 75]. Indeed the relative error was less than 10%, as shown in Table 4.2.

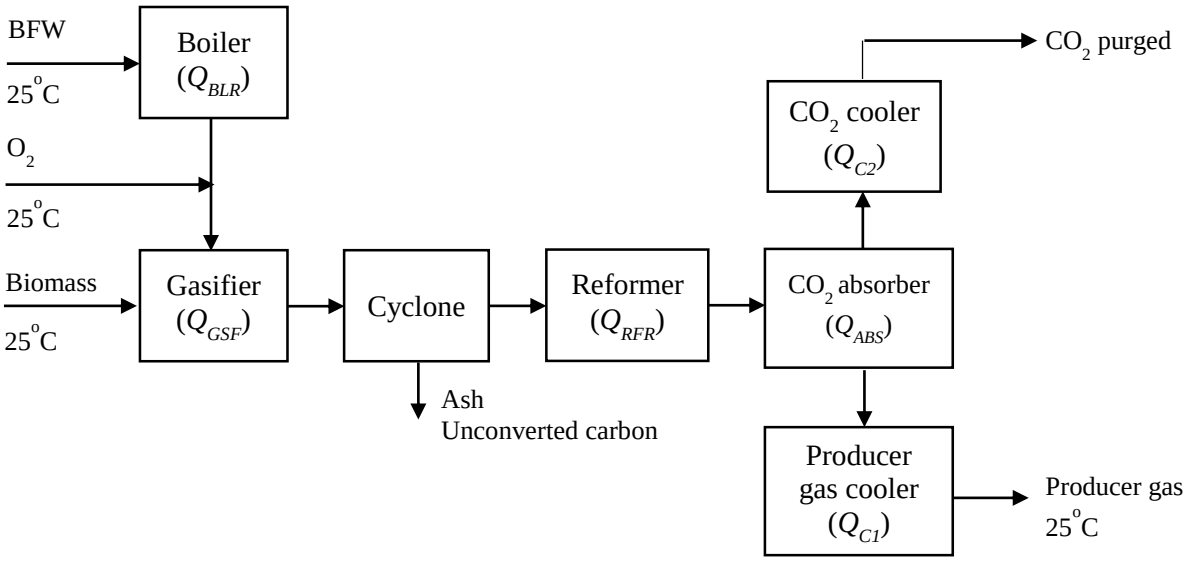

Figure 4.2. Process flow diagram of combined gasifier and reformer with CO_2 recycle.

Table 4.2. Model validation. (Biomass $CH_{1.4}O_{0.6}$, $CO_2/C = 0.5$ and P = 1 atm).

	Our work	Renganathan [75]	Chaiwatanodom [72]	%Error [75]	%Error [72]
T = 800°C					
H_2	31.34%	30.70%	30.98%	2.06%	1.16%
CO	62.22%	60.00%	59.78%	3.56%	3.92%
CO_2	6.02%	9.80%	9.01%	n.r	n.r
CH_4	0.42%	0.00%	4.30%	n.r	n.r
T = 1000°C					
H_2	31.64%	29.00%	30.25%	8.34%	4.39%
CO	63.67%	62.50%	62.41%	1.84%	1.98%
CO_2	4.69%	8.10%	7.33%	n.r	n.r
CH_4	0.00%	0.00%	5.87%	n.r	n.r
T = 1200°C					
H_2	31.65%	29.00%	29.43%	8.36%	7.01%
CO	63.67%	65.00%	64.29%	-2.08%	-0.97%
CO_2	4.68%	6.70%	6.28%	n.r	n.r
CH_4	0.00%	0.00%	7.10%	n.r	n.r

A parametric study was conducted by varying (1) the gasification temperature, (2) the reformer temperature, (3) the oxygen equivalence ratio, and (4) steam to carbon ratio. Performance of the gasification process can be described in term of (1) the composition of producer gas, (2) cold gas efficiency, and/or (3) gas system efficiency.

Dry gas composition was used to determine the composition of producer gas. Low heating value (LHV) of producer gas was defined as the average of heating value of all components in the producer gas as indicated below:

$$LHV_{producer\ \ gas} = y_{H_2} \times LHV_{H_2} + y_{CO} \times LHV_{CO} + y_{CH_4} \times LHV_{CH_4} \tag{4.10}$$

Where y_{H_2}, y_{CO} and y_{CH_4} are mole fraction of hydrogen, carbon monoxide and methane, respectively while; LHV_{H_2}, LHV_{CO} and LHV_{CH_4} are low heating value of hydrogen, carbon monoxide, and methane, respectively.

Cold gas efficiency (CGE) is the ratio of the energy in the producer gas to the energy in the biomass, as defined in the equation given below [75].

$$CGE(-) = \frac{m_{producer\ gas} \cdot LHV_{\ producer\ gas}}{m_{biomass} \cdot LHV_{\ biomass}} \tag{4.11}$$

where, $m_{producer\ gas}$ is mass flowrate of producer gas, $m_{biomass}$ is mass flowrate of biomass, $LHV_{producer\ gas}$ is low heating value of producer gas and $LHV_{biomass}$ is low heating value of biomass. By definition, the value of CGE is equal to 1, if the energy in the biomass is completely converted into producer gas then

Gasification system efficiency (GSE), defined by Eq. (4.12), was used to measure the energy efficiency of the gasification process. Two rule of thumbs were employed in order to calculate the energy requirement for (i) O_2 production (30 kW/ton O_2 produced [80]), and (ii) CO_2 absorption (3 MJ/kg CO_2 absorbed [81]). The higher the GSE value, the better the performance of gasification process.

$$GSE = \frac{m_{producer\ gas} \times LHV_{producer\ gas} + Q_{C1} + Q_{C2} + Q_{GSF} + Q_{RFR}}{m_{biomass} \times LHV_{biomass} + Q_{BLR} + Q_{ABS}} \tag{4.12}$$

where, Q_{C1} and Q_{C2} are energy produced from cooling producer gas and CO_2, respectively; Q_{GSF} and Q_{RFR} are energy required/produced from gasifier and reformer, respectively; and Q_{BLR} and Q_{ABS} are energy consumed by boiler and CO_2 absorber, respectively.

A biomass feed rate of 100 kg/hr was used in all simulation. The ultimate and proximate analysis of the biomass, including the heating value of biomass are summarized in Table 4.3. For each biomass, we investigate the effect of (1) gasifier temperature, (2) reformer temperature, (3) oxygen equivalence ratio, and (4) steam to carbon ratio on the gasification performance. The temperature of gasifier has to be maintained at a suitable temperature (isothermal operation) in order to meet the energy requirement and/or kinetic limitation [75]. The operating conditions of the gasification process are summarized in Table 4.4. During the simulation, the effect of tar formation during gasification was neglected.

Table 4.3. Proximate and ultimate analysis of various biomass.

	Mangrove [82]	Rice husk [83]	Palm frond [5]	Algae (*N. oculta*) [9]
Proximate (wt.%)				
Moisture	5.3	9.5	5.3	6.71
Volatile matters	36.26	67.6	71	78.94
Fixed carbon	56.4	6.3	16.8	7.95
Ash	2.04	16.6	6.9	6.4
Ultimate analysis (wt.%)				
C	66.46	49.2	43.6	47.50
H	4.37	2.2	4.76	6.15
O	29.14	48.02	50.56	46.35
N	0.03	0.44	0.57	n.r
S	n.r	0.06	0.51	n.r
Cl	n.r	0.08	n.r	n.r
High heating value (MJ/kg)	25.34	19.8	18.11	15.07

Table 4.4. Operating conditions in the simulation.

Inlet temperature of biomass, boiler feed water and O_2	25^{o}C
Temperature of steam entering gasifier	327^{o}C
Temperature of gasifier	600 – 1200^{o}C
Pressure in the all simulations	1 bar
Equivalence ratio	0 – 1
Steam to biomass ratio	0 – 2

4.3. Thermodynamic study of tar elimination in biomass gasification

4.3.1. Process description

The gasifier consists of four zones: (1) pyrolysis, (2) combustion, (3) counter-current reduction, and (4) co-current reduction (see block flow diagram in Figure 4.3). A biomass feedstock is fed into the pyrolysis zone at the top of the gasifier. In this pyrolysis section, the biomass is converted into solid products (char and ash) and gaseous products (combustible gases, volatile matters, and tars). One should note that the recycle gas from counter-current zone also flows to the pyrolysis zone due to the suction force from the injector. Concurrently, air is injected into the combustion zone through the injector. In addition, in order to enhance the yield of H_2, steam is introduced into the gasifier. The solid products, from the pyrolysis zone, flow to the counter current zone while the gaseous products along with steam and air go to the combustion zone through the injector. The gaseous products from the combustion zone are then split into two streams: (1) a main stream, which flows to the co-current reduction zone, and (2) a recycle stream, which flows to the counter-current reduction zone. In the counter-current reduction zone, the char reacts with the recycle gas from the combustion zone. The remaining char directly goes to the co-current reduction zone while the gaseous products flow to the pyrolysis zone. In the co-current reduction zone, the char reacts with the gaseous products from the combustion zone, and yields gas producer (i.e., mainly CO, H_2, CH_4 and CO_2). It is worth mentioning that the whole gasification systems involves the set of consecutive chemical reactions summarized below [7].

Partial oxidation $\quad C + \frac{1}{2} O_2 \leftrightarrow CO \quad \Delta H^0_{298} = -111$ MJ/kmol $\quad (4.13)$

Boudouard reaction	$C + CO_2 \leftrightarrow 2CO$	ΔH^0_{298} = +172 MJ/kmol	(4.14)
Steam reforming	$C + H_2O \leftrightarrow CO + H_2$	ΔH^0_{298} = +131 MJ/kmol	(4.15)
Methane formation	$C + 2H_2 \leftrightarrow CH_4$	ΔH^0_{298} = –74MJ/kmol	(4.16)
Water-gas shift reaction	$CO + H_2O \leftrightarrow CO_2 + H_2$	ΔH^0_{298} = –42 MJ/kmol	(4.17)
Methane reforming	$CH_4 + H_2O \leftrightarrow CO + 3H_2$	ΔH^0_{298} = +206 MJ/kmol	(4.18)
CO_2 reforming	$CH_4 + CO_2 \leftrightarrow 2CO + 2H_2$	ΔH^0_{298} = +247 MJ/kmol	(4.19)
Furan steam reforming	$C_4H_4O + 4H_2O \leftrightarrow 4CO + 6H_2$	ΔH^0_{298} = +287 MJ/kmol	(4.20)
Hydrogen combustion	$H_2 + ½\ O_2 \leftrightarrow H_2O$	ΔH^0_{298} = –484 MJ/kmol	(4.21)

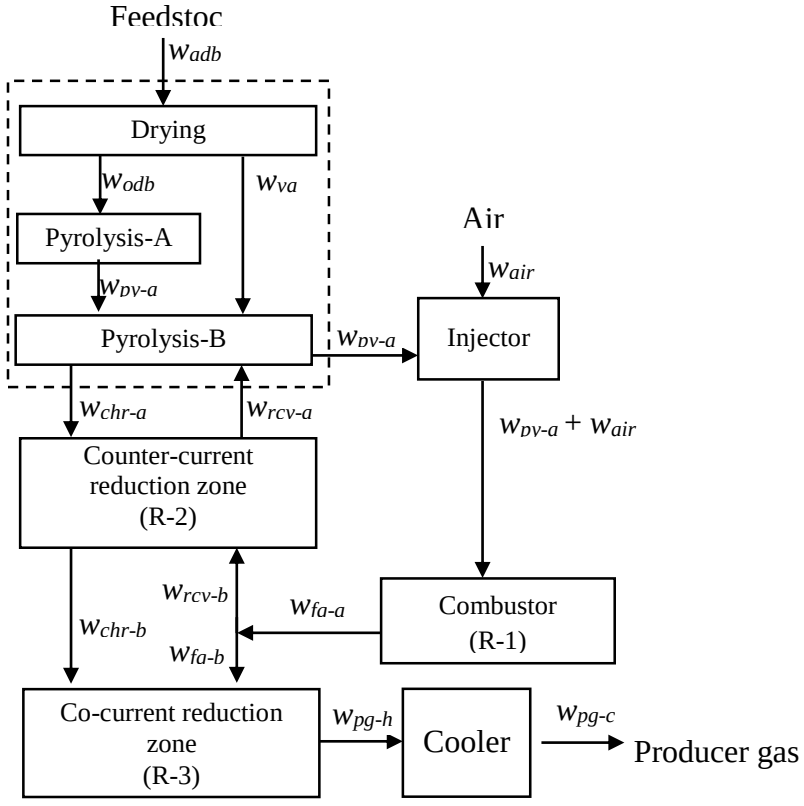

Figure 4.3. Block diagram of downdraft gasifier with internal recycle (dashed line: pyrolysis zone) [25]

4.3.2. Process simulation

In our study, the Gibbs minimization approach is achieved by Aspen Plus software. In order to build the model of gasification process in Aspen Plus, both the biomass and the ash are considered as nonconventional component, while the solid carbon and the gaseous products are assigned as cisolid component and mixed component, respectively. Consequently, the MIXCINC stream class is picked in order to tackle those components. The Peng-Robinson thermodynamic package is used as a global property package in the simulation. Further information related to the operating conditions of the gasification in the Aspen Plus are summarized in Table 4.5. In context of the present simulation, one should notice that (1) nitrogen and ash are considered as inert components, and (2) mass transfer effect and pressure drop are negligible.

Table 4.5. Operating conditions in the simulation.

Inlet temperature of biomass, boiler feed water, and oxygen	298 K
Temperature of steam	600 K
Pressure in the all blocks and streams	100 kPa
Oxygen equivalence ratio	0 – 1
Steam to carbon ratio	0 – 2

Drying

The air-dried biomass with a mass flow rate of 28 kg h^{-1} and a moisture content of 8wt% is used in this simulation. The block diagram of the process is shown in Figure 4.3. In the case of drying process, the moisture content of the air-dried biomass (m_{adb}) is assumed to be completely vaporized due to high temperature (850 K), resulting the oven-dried biomass

(m_{odb}). One should notice that the oven-dried biomass (m_{odb}) goes to the pyrolysis-A while the water vapor (w_{vap}) flow to the pyrolysis-B.

Pyrolysis-A

In the pyrolysis-A, the oven-dried biomass is converted into char, volatiles, ash, and tar. The ultimate and proximate analysis of the biomass as oven-dried is shown in Table 4.6.

Table 4.6. Ultimate and proximate analysis of the biomass [25]

Proximate	wt% db
Volatile matters	81.0
Fixed carbon	19.0
Ultimate	
C	49.7
H	6.5
O	43.3
Ash	0.5

In the present simulation, the following assumptions are made:

1. Carbon and ash are the only constituent of the char. This assumption is based on the experimental results by Fagbemi et al. [34] showing that the char is dominated by carbon atom (>88wt% at pyrolysis temperature of 500^{o}C (773 K)). The ash is assumed to be inert.
2. The amount of the ash free char is calculated using the empirical relationship of char mass yield as a function of temperature [84], as follow:

$$Y_C = 0.106 + 2.43 \times \exp(-0.66 \times 10^{-2} \times T) \quad (4.22)$$

where Y_c and T are char mass yield in kg ash free char/kg daf biomass, and pyrolysis temperature in ^{o}C, respectively.

3. Volatiles is limited to contain CO, H_2, CO_2, H_2O, CH_4 and C_2H_6. This assumption is taken because many literatures [34, 85, 86] reported that the CO, H_2, CO_2, H_2O, CH_4 and C_2H_6 are the major gases from pyrolysis process.
4. Tar is represented by C_4H_4O. de Lasa et al. [4] reported that C_4H_4O presents in the biomass tars from the pyrolysis at 450–500 ^oC.

The number of moles of the volatiles (i.e., CO, H_2, CO_2, H_2O, CH_4, and C_2H_6) and the tar (i.e., C_4H_4O) are calculated by solving the elemental balance. A proper initial value must be taken in order to approach the correct composition of the volatiles and tar. The composition of the products of the pyrolysis-A are summarized in Table 4.7.

Table 4.7. The composition of the products of the pyrolysis-A

Component	Mol fraction	Mass fraction
Volatiles and tar		
CO	0.11	0.11
H_2	0.10	0.01
CO_2	0.13	0.20
CH_4	0.05	0.03
C_2H_6	0.07	0.08
H_2O	0.41	0.27
C_4H_4O (tar)	0.10	0.31
Char (solid)		
C	n.c*	0.97
Ash	n.c	0.03

*n.c.: not calculated

Pyrolysis-B

In the pyrolysis-B, the water vapor (w_{vap}) from drying process, and the volatile ($w_{py\text{-}a}$) from the pyrolysis-A react with the recycle gas ($w_{rcy\text{-}a}$) from the counter current reduction zone. One should notice that the equilibrium are not reached by the char and the tar in the Pyrolysis B. In other words, the tar and the char are considered as non-reacting

components. This is attributed to the fact that decomposition of tar does not occur at 850 K [13]. In addition, the absence of oxygen in the Pyrolysis-B retard char conversion since the reactivity of gasifying agent decreases in the following order: oxygen > steam > CO_2 [19].

Combustion zone

After pyrolysis-B, the pyrolysis gas ($w_{py\text{-}a}$) along with the air (w_{air}) are directed to the combustion zone through the injector. The counter-current reduction zone is simulated using RGibbs since the high reaction temperatures are expected. The modification in the RGibbs is attempted in order to match the experimental results. In the combustion zone, CH_4 is considered as a non-reacting component. Indeed, this assumption lays on the fact that CH_4 is diluted. One should notice that the amount of oxygen in the combustion zone is not sufficient to oxidize the combustible gases (i.e., H_2, CO, and CH_4). Furthermore, due to the lack of oxygen, the flame speed of CH_4 is lower than that of CO or hydrogen [23]. Due to this modification, oxygen, an air component, reacts with hydrogen from the pyrolysis zone through exothermic hydrogen combustion reaction (Eq. 9). Due to this exothermic reaction, high temperature can be achieved. It is worth mentioning that the temperature in the combustion zone reach 1495 K, which is sufficient for tar decomposition [5]. This is also confirmed by the experimental studies on thermal cracking [9, 24] that the amount of tars significantly decrease at temperatures higher than 1273 K. It is worth noticing that the use of oxygen as a gasifying agent enhance the temperature of the combustion zone, as shown in Figure 4.5a. This is of course due to the absence of inert gas (i.e., nitrogen) in the producer gas. The flue gas ($w_{fg\text{-}a}$) from the combustion zone is split into two streams (i.e., $w_{rcy\text{-}b}$ and $w_{fg\text{-}b}$) with a gas/air recycle ratio of 0.85 (*v*/*v* at stp).

Counter-current reduction zone

After pyrolysis-B, the char ($w_{chr\text{-}a}$) is directly sent to the counter-current reduction zone. The counter-current reduction zone is simulated using RGibbs reactor. No modification is made in the RGibbs for this process. The reactions occur based on the minimization of Gibbs free energy by considering the operating conditions and the composition of the feed components. The unreacted char from counter-current reduction zone are sent to the co-current reduction zone ($w_{chr\text{-}b}$), while the gaseous products are flown to the Pyrolysis-B ($w_{rcy\text{-}b}$).

Co-current reduction zone

The unreacted char ($w_{chr\text{-}b}$) from counter-current reduction zone undergoes to the co-current reduction zone. In addition, the flue gas stream ($w_{fg\text{-}b}$) from the combustion zone is also directed to the co-current reduction zone. The co-current reduction zone is simulated using RGibbs. The modification in the RGibbs is conducted in order to match the experimental results. The modification is done by determining H_2O, CH_4 and C as non-reacting components with non-reacting mole fractions of 0.80, 0.80 and 0.65, respectively. The hot producer gas from co-current reduction zone ($w_{pg\text{-}h}$) is then cooled to 298 K, producing a producer gas with ambient temperature ($w_{pg\text{-}c}$).

4.3.3. Performance evaluation

Performance of the gasification can be described in term of (1) the composition of H_2 and CO in the producer gas, (2) cold gas efficiency, and (3) gasification system efficiency. The composition of producer gas is determined by dry gas composition. Cold gas efficiency (CGE) is the ratio of the energy in the producer gas to the energy in the biomass, as defined below:

$$CGE(-) = \frac{m_{producer\ gas} \cdot LHV_{producer\ gas}}{m_{biomass} \cdot LHV_{biomass}} \tag{4.23}$$

where, $m_{producer\ gas}$ is mass flowrate of producer gas, $m_{biomass}$ is mass flowrate of biomass, $LHV_{producer\ gas}$ is low heating value of producer gas and $LHV_{biomass}$ is low heating value of biomass. Therefore, if the energy in the biomass is completely converted into producer gas then the value of CGE is equal to unity.

Gasification system efficiency (GSE) is used to measure the energy efficiency of the gasification process, as defined in Eq. (16). A rule of thumb is used to calculate the energy requirement for O_2 production: 305 kWh/ton O_2 produced [80]. The higher the GSE value, the better the performance of gasification process.

$$GSE = \frac{m_{producer\ gas} \times LHV_{producer\ gas} + QPYR + QCOMB + QRED1 + QRED2 + QCLR}{m_{biomass} \times LHV_{biomass} + QBOIL + Q_{O_2}} \tag{4.24}$$

where, *QPYR, QCOMB, QRED1, and QRED2* are energy required/produced from the pyrolysis zone, the combustion zone, the counter-current reduction zone, and the co-current reduction zone, respectively, while *QBOIL* and Q_{O_2} represents energy required for steam and O_2 production, respectively. *QCLR* is energy produced from producer gas cooler.

4.3.4. Model validation

For model validation, the simulation is conducted adiabatically with the same feed rate as the one used in the experimental work by Susanto and Beenackers [25]. Indeed, the properties and the heating value of the biomass are also similar to their experimental work. The validation of the model is performed by comparing both the composition and the temperature of the producer gas. Figure 4.4 shows the mole fraction of the producer gas at

different recycle ratios. Clearly, the gas composition of the present simulation agree closely with the experimental results of Susanto and Beenackers [25]. Furthermore, the simulation relative error on the producer gas composition for recycle ratios of 0.4, 0.65, 0.85 and 1.07 are 6%, 8%, 4% and 11%, respectively. In addition, the temperature of the present simulation is also in good agreement with the experimental results, as depicted in Figure 4.5. The experimental temperature of producer gas is lower than that of the simulation due to heat losses in the top of the gasifier.

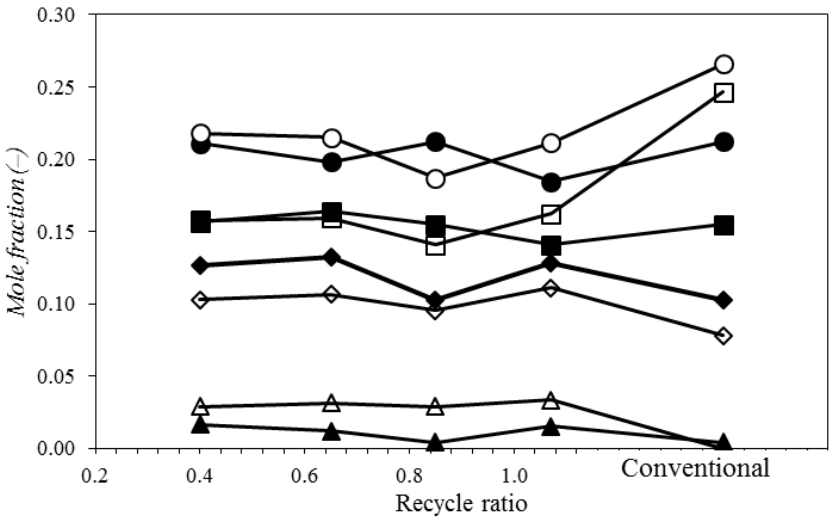

Figure 4.4. Composition of producer gas at various recycle ratios and conventional model(●, ▲, ■, and ◆ represent the mole fraction of CO, CH_4, H_2 and CO_2 obtained from the experiments by Susanto and Beenackers [5], while ○, △, □, and ◇ represent the mole fraction of CO, CH_4, H_2 and CO_2 obtained from the models)

The composition of the producer gas obtained by the conventional gasifier model is also presented in Figure 4.4. The conventional gasifier model refers to the gasifier model which was simulated using two separate reactors (i.e., RYield and RGibbs reactors) for biomass

decomposition and gasification reaction, respectively [7, 72, 73, 75]. In the conventional gasification model, the presence of tars is neglected.

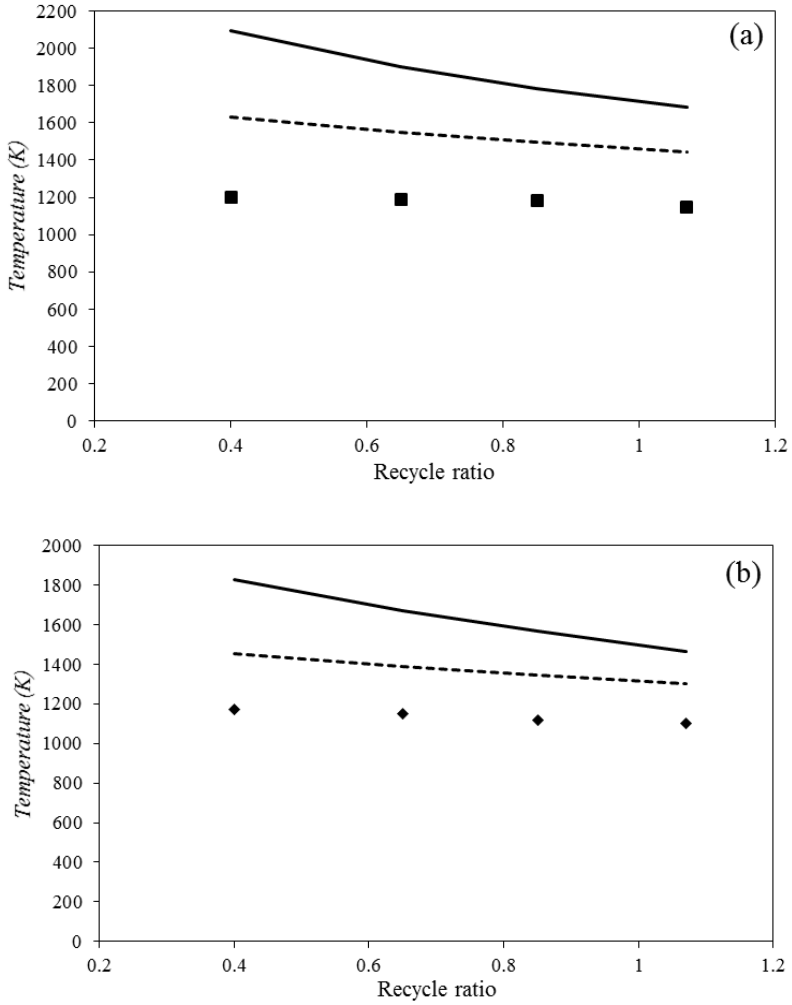

Figure 4.5. Temperature of (a) combustion zone and (b) co-current reduction zone at various recycle ratio. (Full line: model using oxygen, dashed line: model using air, dots: experimental results by Susanto and Beenackers [25])

It is worth mentioning that the accuracy of our present model is higher than that of the conventional gasification model. Indeed, comparison with the experimental results obtained by Susanto and Beenackers [25], show that the relative error of the conventional

model is 33% while our model counterpart is between 4% and 11%. This is because the presence of tar is taken into account by our model. On other hand, the conventional model assumes that tars are not formed during gasification. Despite the fact that the conventional model (i.e., without tar presence) shows good agreement with the experimental results [72], the experimental results that were used for validation reported that a mixture of tar and water (7 – 9wt.% of the output materials) is present [89]. Thus, the assumption of no tar formation in the conventional model can adversely affect model's accuracy (i.e., gas composition and flow rate) especially when compared to the experimental results with minor tar formation in the producer gas.

CHAPTER 5

RESULTS AND DISCUSSION – CATALYST DEVELOPMENT

5.1. Catalyst characterization

5.1.1. Thermal stability

The study of the catalyst thermal stability was conducted under N_2 flow. With this end, both thermogravimetric (TG) and differential thermogravimetric (DTG) analyses were developed.

Figure 5.1 reports both TGA and DTG data for 5-ISA(15)-700, 5-ISA(15)-950 and 5-ISA(15)-1100. One can notice that for the three catalysts considered, an initial catalyst weight loss in the 30 to 200 ^{o}C range was expected. This initial weight loss can be related to the dehydration of physically adsorbed water [90]. In this respect, DTG curves showed a mass loss rate for 5-ISA(15)-750 which was much higher than the mass loss rate for 5-ISA(15)-950 and 5-ISA(15)-1100. This weight loss difference as per the TGA, was assigned to the dissimilarity of crystalline phases formed during catalyst preparation. This was confirmed by the XRD as shown in Figure 5.1, where the sample synthesized by calcination at 750 °C (5-ISA(15)-750) displays an amorphous phase. In contrast to this, catalyst samples prepared by calcination at 950 °C (5-ISA(15)-950) and 1100 °C (5-ISA(15)-1100) with alumina in the γ-phase. Thus, in the case of an amorphous 5-ISA(15)-750 catalyst, the mass loss was considered to be caused by both dehydration of adsorbed water and decomposition of the amorphous material. Thus, it was concluded that Al_2O_3 in

the crystalline γ-phase [91] is more thermally stable than the Al_2O_3 in the more disordered amorphous phase.

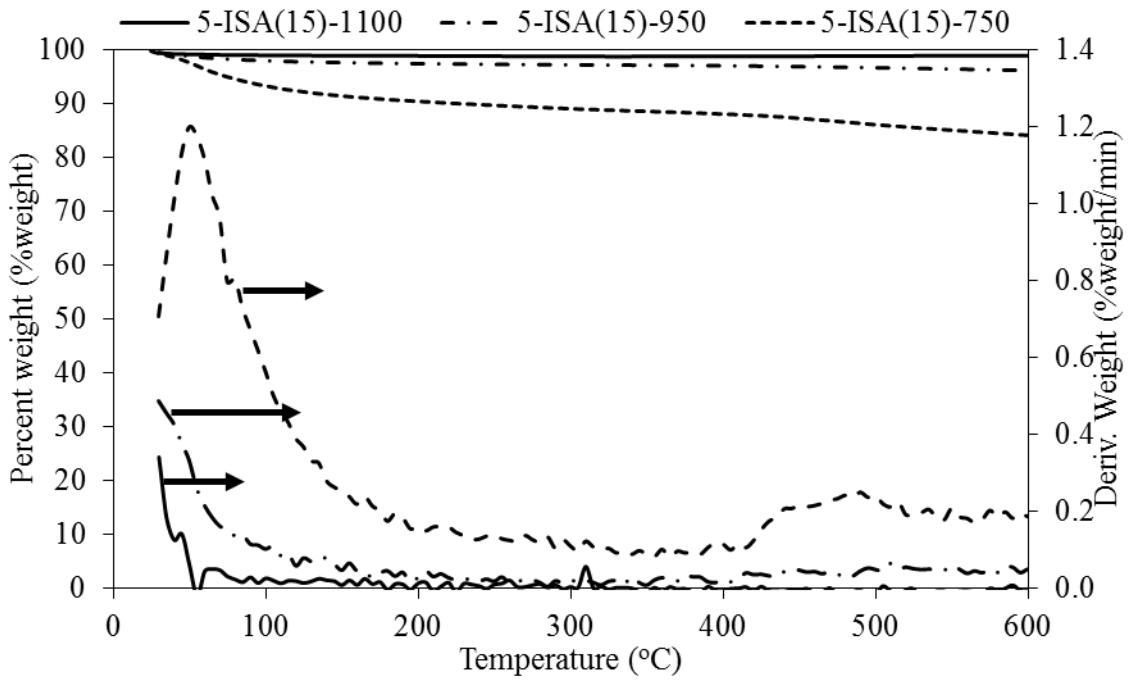

Figure 5.1. TGA analysis result of iron-silica doped alumina.

Furthermore, for the 5-ISA(15)-750, the DTG showed a significant mass loss peak in the 50 to 55 °C range. This peak was assigned to the quick evaporation of the catalyst precursor chemical (alcohol) remaining from catalyst synthesis and the physically adsorbed water. The similar conclusion has been reported by Mardkhe et al. [27]. On the other hand, there were no DTG peaks for 5-ISA(15)-950 and 5-ISA(15)-1100.

However, and as shown in Figure 5.1, there were also significant and additional mass losses as the temperature was increased from 200 to 600 °C [92]. This was especially important for the 5-ISA(15)-750. Mass losses were much more limited for the 5-ISA(15)-950 and 5-ISA(15)-1100. Therefore, it was concluded that the 5-ISA(15)-950 and the 5-

ISA(15)-1100 displayed good and enhanced thermal stability with the SiO_2 addition being favourable.

5.1.2. Phase composition

X-ray diffraction analysis was performed on the fresh catalyst. This was done to investigate the phase composition. Figure 5.2 reports the XRD patterns of a fresh Fe_2O_3/SiO_2-Al_2O_3 catalyst calcined at different temperatures.

The XRD patterns of the synthesized catalyst, calcined at 750°C(5-ISA(15)-750), exhibited an amorphous phase, with no observed peak in the $2\theta = 10^o$ to $2\theta = 90^o$ range. On the other hand, catalyst samples calcined at 950°C (5-ISA(15)-950) and 1100°C (5-ISA(15)-1100) showed the characteristic γ-Al_2O_3 diffraction peaks at $2\theta = 45^o$ and $2\theta = 66^o$. Thus, it was concluded that the addition of Si ions enhances the γ-Al_2O_3 thermal stability, with Si ions retarding α-Al_2O_3 nucleation by replacing Al ions in tetrahedral sites. It is hypothesized that this reduces the total available structure vacancies [93]. These results are in agreement with Mardkhe et al. [27], with a similar conclusion reported for lanthanum addition [94].

In addition, XRD diffraction peaks attributed to mullite ($2Al_2O_3.SiO_2$) were observed as shown in Figure 5.3, for both the 5-ISA(15)-950 and 5-ISA(15)-1100. This appears to be the result of excess Si ions being transformed into mullite crystals [93]. In fact, formation of mullite during the synthesis of SiO_2-doped Al_2O_3, at higher than 10wt% Si, was reported by others [27, 93, 95].

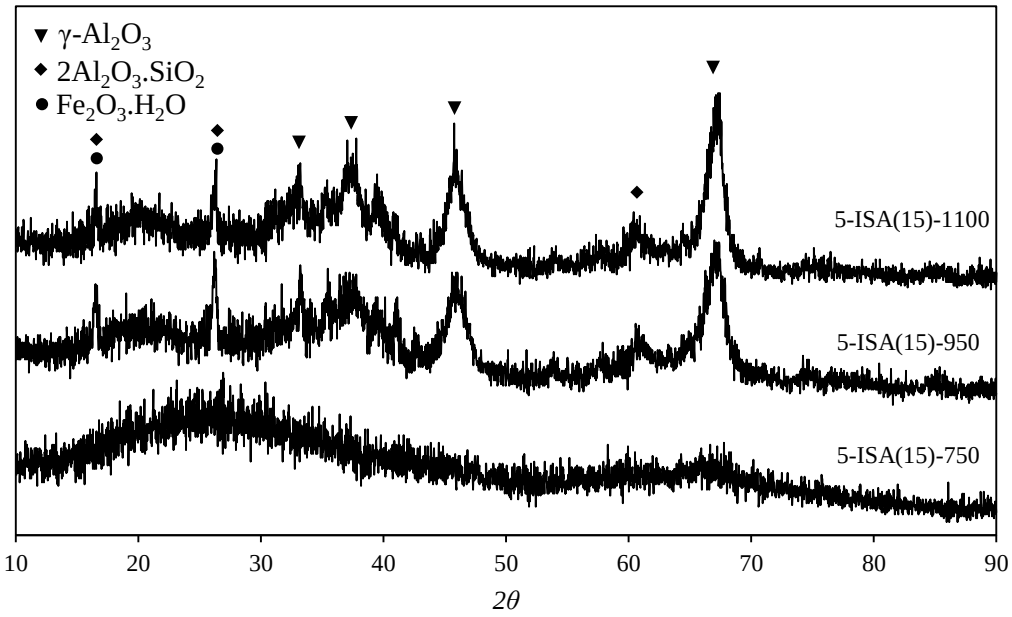

Figure 5.2. XRD pattern of iron-silica doped alumina synthesized by different calcination temperatures.

Regarding the XRD reported in Figure 5.2, one may notice the difficulty of assessing iron oxide (Fe_2O_3) using XRD. Fe_2O_3 peaks may potentially overlap with mullite at the 2θ = 17° and 2θ = 26° bands. Interpretation of XRD is further complicated given Si is loaded at 15wt% and Fe at 5wt%. For more precise, when the iron loading is increased up to 10wt% and 15wt%, there are two more peaks correspond to Fe2O3 at 2θ = 33° and 2θ = 35° bands, as shown in Figure 5.4.

Figure 5.4 exhibits the XRD patterns of the fresh Fe_2O_3/SiO_2-Al_2O_3 catalyst with different iron loadings. One can notice that the XRD patterns for 0wt% Fe catalyst calcined at 950 ^oC (0-ISA(15)-950) were dominated by γ-Al_2O_3 peaks. One can also observe that the crystallinity of the γ-Al_2O_3 decreased with iron loadings, while mullite peaks increased. This finding was particularly significant when iron loadings increased from 10wt% to 15wt%.

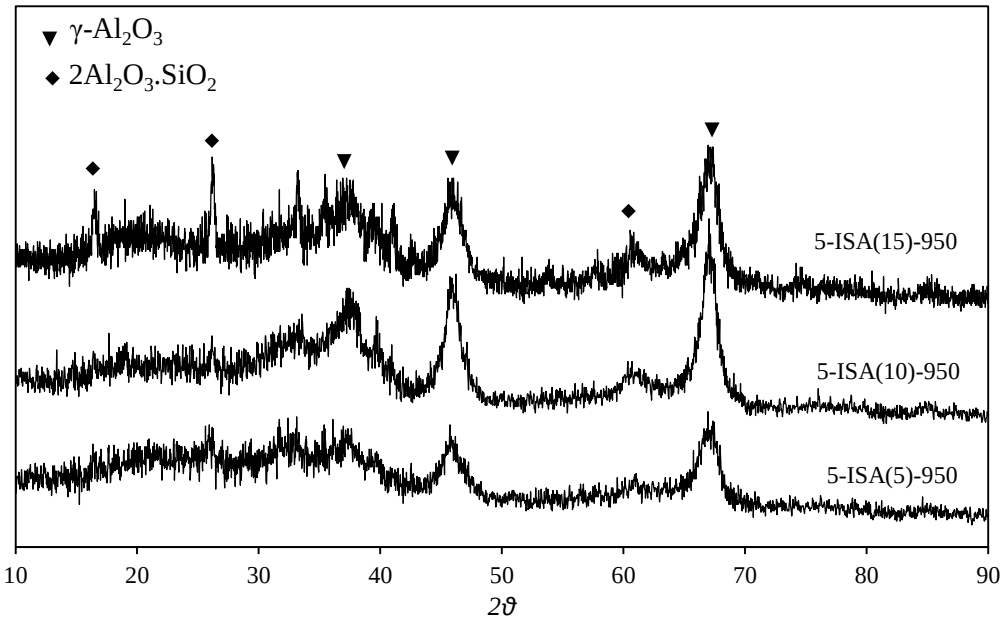

Figure 5.3. XRD pattern of iron-silica doped alumina at various Si loading.

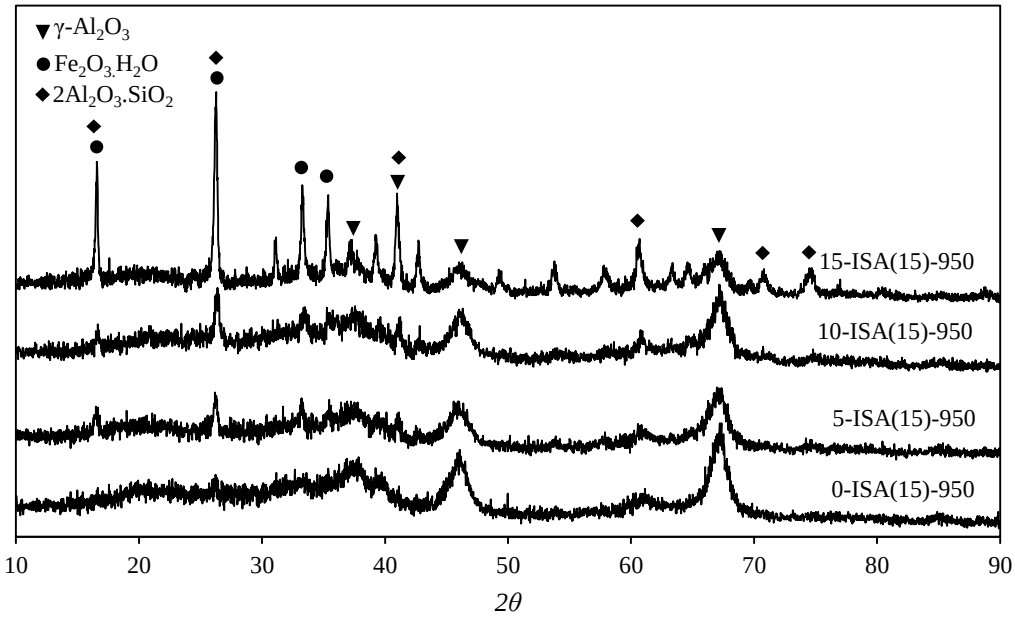

Figure 5.4. XRD pattern of iron-silica doped alumina at various iron loadings.

Figure 5.2 and Figure 5.3 do not show the XRD peaks for SiO_2, at $2\theta = 22.5^o$. The absence of SiO_2 XRD peaks was attributed to SiO_2 being in the amorphous phase or alternatively being homogenously mixed with the support in other phases. This is consistent with the findings of others [27, 93]. On the other hand, the Fe_2O_3 XRD peaks at $2\theta = 33^o$ and 35^o were clearly observed on the 15wt% of iron sample (15-ISA(15)-950).

5.1.3. Textural properties

Table 5.1 shows the surface areas, pore volumes and average pore diameters for the fresh catalysts. The BET (Brunauer–Emmett–Teller) measurements showed that the surface area of 5-ISA(15)-950 was significantly higher than that of the 5-ISA(15)-750. This indicates that the γ-Al_2O_3 (crystalline phase) contributes with a higher BET surface area than the amorphous material. This was attributed to the microscopic structure of the γ-Al_2O_3, which is a regular and ordered lattice [96, 97]. In this regard, the XRD shows that γ-Al_2O_3 was formed after calcination at 950 ^oC, while the amorphous phase found at 750 ^oC. Interestingly, the BET surface area of the catalysts calcined at 950 ^oC with 10wt% iron loading (10-ISA(15)-950) (29 m^2/g) was higher than that obtained by Ashok and Kawi (20 m^2/g) [98]. In addition, the catalysts calcined at 1100 ^oC (5-ISA(15)-1100) (8 m^2/g) displayed considerably larger BET surface areas than those studied by Kumar et al (<1 m^2/g) [28]. This shows that the addition of 15wt% silica improves the structural properties of alumina at high temperatures. However, the BET surface area of 5-ISA(15)-1100 was much lower than the BET surface area of 5-ISA(15)-950. This was attributed to the 1100 °C calcination temperature enhancing the formation of mullite, yielding a lower the surface area [93].

Table 5.1. BET and BJH results of Fe_2O_3/SiO_2-Al_2O_3 catalyst at different calcination temperatures.

Samples	A_{BET} (m^2/g)	BJH Pore diameter (Å)	BJH Pore Volume (cm^3/g)	Ref.
5-ISA(15)-750	46	100	0.107	This work
5-ISA(15)-950	49	146	0.189	This work
5-ISA(15)-1100	8	67	0.023	This work
10-ISA(15)-950	29	111	0.085	This work
15-ISA(15)-950	6	96	0.011	This work
3%Fe- Al_2O_3[a]	< 1	n/a	0.002	[28]
9%Fe- Al_2O_3[b]	20	n/a	n/a	[98]

[a] calcined at 1100 for 8 h
[b] calcined at 900ºC for 4 h

The pore volume of the catalysts was measured by the BJH (Barrett-Joyner-Halenda) method. Table 5.1 shows that: a) the pore volume increased as the calcination temperature was raised from 750 to 950 ºC, and b) the pore volume decreased when calcination temperature increased up to 1100 ºC. Thus, it appears that the crystalline phase yields more porous catalysts than the amorphous phase. In addition, the catalyst in the crystalline phase also has larger pore diameters than the catalyst in the amorphous phase. On the other hand, for the sample calcined at 1100 ºC, there is both a reduction of pore diameter and pore volume. This can be assigned to the mullite surface formation resulting in a reduction of pore volume via pore blocking [93]. Furthermore, Figure 5.5 shows a bimodal pore size distribution for both the 5-ISA(15)-750 and 5-ISA(15)-950 and a single mode pore size distribution for 5-ISA(15)-1100. One should notice that for 5-ISA(15)-750 and 5-ISA(15)-950, the following was observed: a) mesopores in the 2.5 – 12 nm range, b) macropores

in the 90 – 140 nm range. It was also revealed that the macropore distribution significantly increased, as calcination temperature rose from 750 to 950 ^{o}C. This can also be attributed to the formation of γ-Al_2O_3 at 950 ^{o}C. However, at 1100 ^{o}C, the pore sizes of the catalyst drastically decreased. This was assigned to the collapse of the interfacial silica-alumina phase [27].

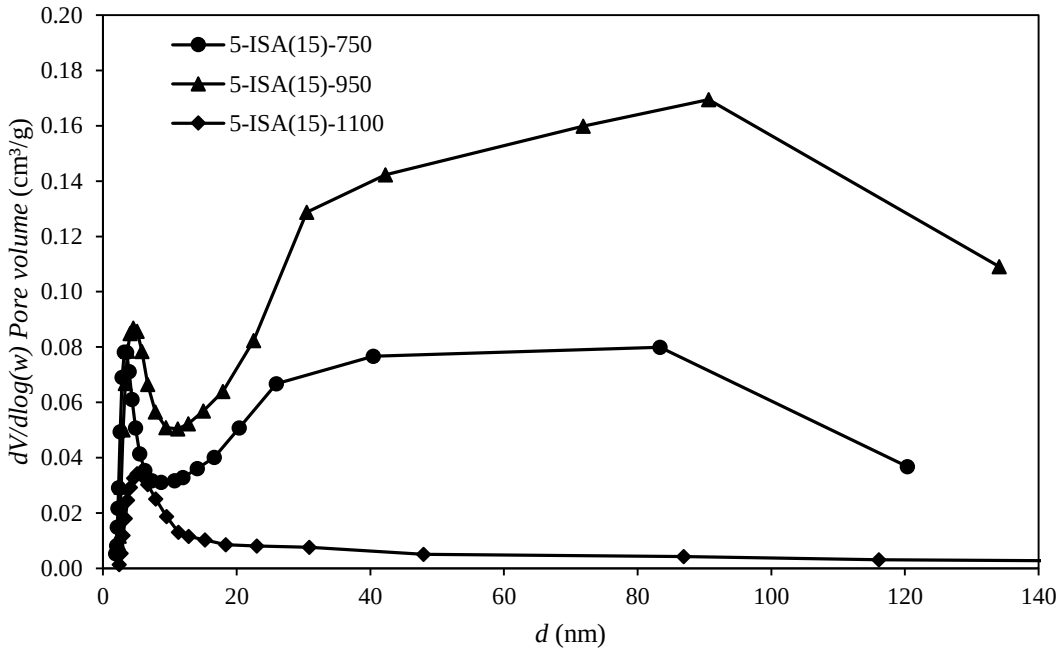

Figure 5.5. BJH pore size distribution curve of Fe_2O_3/SiO_2-Al_2O_3 catalyst synthesized at different calcination temperatures.

5.1.4. Acidity

Catalyst acidity plays a significant role in catalytic activity and carbon deposition [99]. Acid sites are assigned to the catalyst surface protons [100]. In addition and with respect to protonic acidity, the strength can be defined as the O-H bond energy between the framework oxygen and the attached protons [101]. In the present study, the acidity of the fresh catalysts was measured using NH_3-temperature programmed desorption (TPD).

Ammonia is a good basic probe molecule allowing the quantification of acidity of the solid catalysts. In addition, given its small molecular size, ammonia is able to reach acid sites in very small pores [102]. Using NH_3-TPD, the area under the desorbed ammonia peak gives the total acidity, while the peak position is an indicator of the acid site strength.

Table 5.2 reports the total acidity of Fe_2O_3/SiO_2-Al_2O_3 catalysts with various iron loadings. It was found that the total acidity increased from 283 to 957 µmol/g when the iron loading was raised from 5wt% to 10wt%. This showed that the higher iron loadings increased the number of acid sites, with acidity in Fe_2O_3 being in the 33 – 52 µmol/g range [103]. Thus, it can be concluded that the addition of iron oxide yielded new acid sites on the SiO_2-Al_2O_3. This is in agreement with the findings of others [104]. Furthermore, it has also has been reported in the earlier literature [105], that new acid sites can be generated by adding a second metal oxide. However, Fe addition in excess of 15wt%, appears not to have an effect on the total acidity, while increasing however, the acid site strength.

Table 5.2. Total acidity of the catalysts as measured by NH_3-TPD.

Sample	Weak (µmol/g STP)	Strong (µmol/g STP)	Total (µmol/g STP)
5-ISA(5)-950	257	108	365
5-ISA(15)-950	195	88	283
10-ISA(15)-950	581	376	957
15-ISA(15)-950	278	675	952

Addition of SiO_2 to the catalyst yields a mild acidity reduction. This effect is however, lower than the one observed when adding iron oxide. In this regard, Table 5.2 reports acidity densities decreasing from 365 to 283 µmol/g when SiO_2 augments from

5wt% to 15wt%. These results appear to be inconsistent with Mardkhke et al. [27]. This author showed that total acidity of SiO_2-Al_2O_3 augmented with increasing SiO_2 in the 5wt% to 15w% range, for samples calcined at 900^oC. In addition, Yaripour et al. [106] and Mollavali et al. [107] also reported a similar trend. However, Mardkhke et al. [27] also showed that the total acidity of SiO_2-Al_2O_3 diminished at higher SiO_2 contents for samples calcined at 1100 ^oC. Thus, it is suggested that the presence of iron oxide likely changes the nature of the SiO_2-Al_2O_3 acidity.

Figure 5.6 reports the two broad NH_3-TPD peaks observed at 100 – 250 ^oC and 500 – 750 ^oC. These NH_3-TPD peaks correspond to weak and strong acid sites, respectively [108]. One can notice that increasing the iron loading from 10wt% to 15wt%, yields drastically reduced peaks in the 100 – 250 ^oC range, while the peaks in the 500 – 750 ^oC range are significantly augmented. This suggests that the addition of Fe enhances the number of strong acid sites. In addition, the weak acid site reduction may be due to the blockage of weak acid sites given the expected mullite and iron oxide formation. This interpretation is supported by XRD as shown in Figure 5.4. This explanation is also confirmed by the catalyst properties reported in Table 5.1, where the surface area and pore volume of 10-ISA(15)-950 are higher than those for 15-ISA(15)-950. A similar phenomenon of pore blockages on acid sites has been reported by Nie et al [108] when considering the addition of CuO-ZnO on H-ZSM-5.

In order to establish NH_3-TPD desorption kinetics, on the prepared iron supported alumina catalysts, desorption parameters were determined using the approach from Cvetanovic and Amenomiya [109, 110]. Furthermore, White [111] proposed an adapted desorption rate model assuming the following:

(i) The ammonia desorption rate is a first order rate process.

(ii) The concentration of ammonia through the catalysts bed is uniform.

(iii) The increase of temperature is linear with time.

(iv) Readsorption of the desorbed ammonia does not occur.

(v) The catalyst surface is homogenous for ammonia adsorption. Therefore, the desorption constant (k_{des}) can be described by an Arrhenius equation (Eq. (5.1)) and is not a function of surface coverage (θ).

$$k_{des} = k_{do} \exp\left(\frac{-E_{des}}{RT}\right) \tag{5.1}$$

Regarding the assumptions of the rate model, the following can be stated: 1) (i) is considered adequate given the unimolecular desorption of ammonia [112], 2) Experimental conditions for ammonia TPD are selected to comply with assumptions (ii) and (iii), 3) The high gas flow rate is maintained to comply with assumption (iv).

Thus, the ammonia desorption rate can be evaluated using a material balance of desorbing ammonia [113] as follows:

$$r_{des} = -V_m \frac{\left(d\theta_{des}\right)}{dt} = k_{do}\theta_{des} \exp\left[-\frac{E_{des}}{R}\left(\frac{1}{T} - \frac{1}{T_m}\right)\right] \tag{5.2}$$

where T_m is the centering temperature, V_m represents the amount of ammonia adsorbed at saturation, θ_{des} represents the fractional surface coverage of the adsorbed species, k_{do} represents the pre-exponential factor, E_{des} represents the energy of desorption, and R represents the universal gas constant.

As described in the model assumptions, the temperature (T) in the ammonia TPD experiments increased at a constant heating rate using the following equation:

$$T = T_0 + \beta t \tag{5.3}$$

$$\frac{dT}{dt} = \beta \tag{5.4}$$

where, T_0 is the initial temperature, β is the heating rate and t is the heating time.

By applying the chain rule using Eq. (5.4):

$$\frac{\left(d\theta_{des}\right)}{dt} = \left(\frac{d\theta_{des}}{dT}\right)\left(\frac{dT}{dt}\right) = \left(\frac{d\theta_{des}}{dT}\right)\beta \tag{5.5}$$

and substituting Eq. (5.5) into Eq. (5.2), this yields:

$$\frac{d\theta_{des}}{dT} = \frac{k_{do}\theta_{des}}{V_m\ \beta}\exp\left[-\frac{E_{des}}{R}\left(\frac{1}{T}-\frac{1}{T_m}\right)\right] \tag{5.6}$$

Given that

$$\theta_{des} = 1-\frac{V_{des}}{V_m} \tag{5.7}$$

Thus, the rate of change of the θ_{des} site with temperature can be expressed as follow:

$$\frac{d\theta_{des}}{dT} = \frac{k_{do}}{V_m\ \beta}\left(1-\frac{V_{des}}{V_m}\right)\exp\left[-\frac{E_{des}}{R}\left(\frac{1}{T}-\frac{1}{T_m}\right)\right] \tag{5.8}$$

Eq. (5.8) is a first order ordinary differential equation that can be solved using the separation of variable method, yielding:

$$V_{des} = V_m\left(1-\exp\left[\ln\left(1-\frac{V_{do}}{V_m}\right)-\frac{k_{do}RT^2}{E_{des}\beta V_m}\left\{\exp\left(\frac{-E_{des}}{R}\left(\frac{1}{T}-\frac{1}{T_m}\right)\right)-\exp\left(\frac{-E_{des}}{R}\left(\frac{1}{T_o}-\frac{1}{T_m}\right)\right)\right\}\right]\right) \tag{5.9}$$

where V_{do} and T_0 are initial values for the desorbed volume and temperature desorption, respectively.

Considering Eq. (5.9), the energy of desorption of ammonia (E_{des}) can be fitted to ammonia TPD data. Data fitting can be accomplished with the least square method, using MATLAB at a 95% confidence limit and with a specific tolerance of 10^{-8}.

Table 5.3 reports the estimated energy of desorption for weak acid catalyst sites and strong acid catalyst sites with various iron loadings. The various statistical indicators such as the high correlation coefficient number (R^2) and the narrow spans of the 95% confidence intervals, show e that the model considering in Eq. (5.9) is in excellent agreement with the experimental data. Furthermore, Figure 5.7 shows the fitted model using Eq. (5.9) and the experimental data. This figure shows a good agreement between the experimental data and the predicted values, which further confirm the validity of the model.

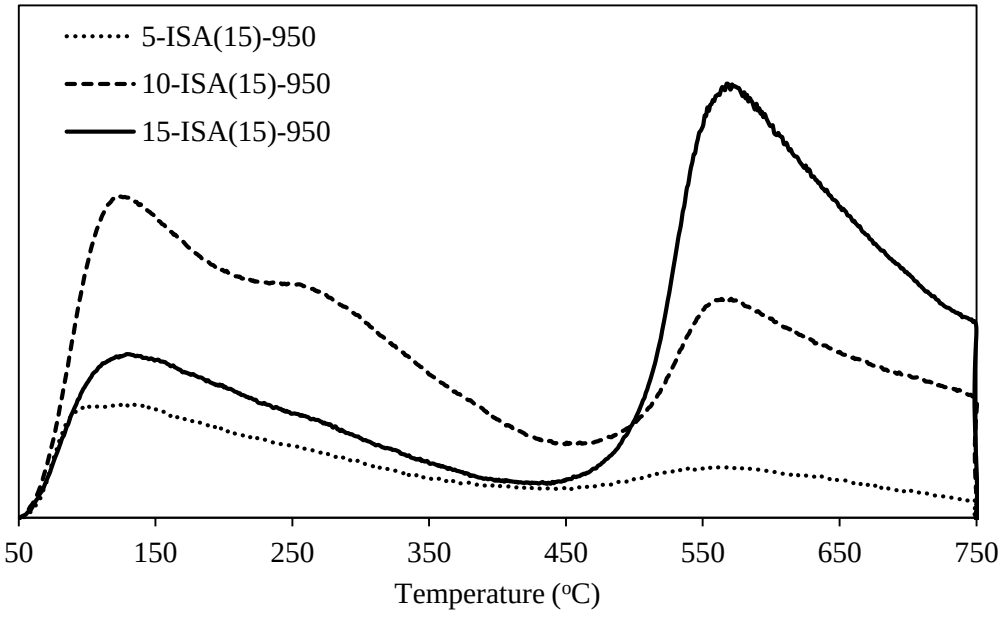

Figure 5.6. NH_3-profile of the catalysts.

Table 5.3. Estimated parameters for ammonia TPD kinetics (ramp rate 10°C min^{-1})

	Weak			Strong		
Catalysts	E_{des} (kJ mol^{-1})	R^2	V_{NH3} (cm^3 g^{-1})	E_{des} (kJ mol^{-1})	R^2	V_{NH3} (cm^3 g^{-1})
5-ISA(15)-950	11.1 ± 0.19	0.997	4.36	100.5 ± 1.1	0.996	1.97
10-ISA(15)-950	7.5 ± 0.12	0.998	13.01	84.9 ± 1.3	0.994	8.42
15-ISA(15)-950	10.8 ± 0.19	0.997	6.22	76.4 ± 1.3	0.994	15.11

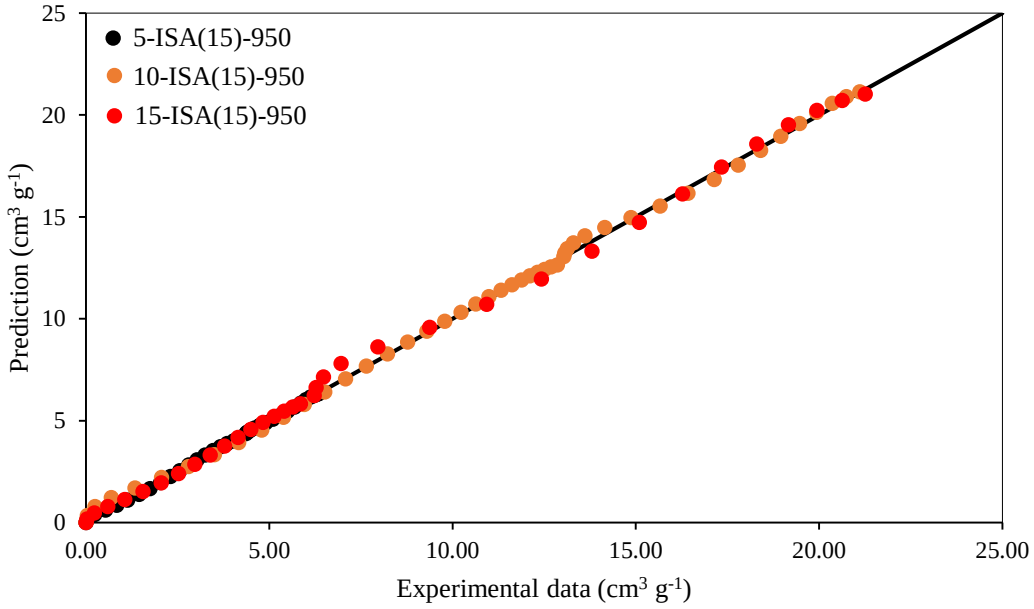

Figure 5.7. The fitted model (Eq. (5.9)) and the experimental data of ammonia desorbed for the catalysts with different iron loadings (heating rate 10°C min^{-1}).

Since the acidity of the samples studied, for both weak acid sites and strong acid sites, showed separate NH_3-TPD peaks with limited overlapping, the estimated activation energies for ammonia desorption in weak acid sites and strong acid sites were calculated separately.

Table 5.3 reports the desorption energy for the strong acid sites. It was found that for 5wt% iron (5-ISA(15)-950) the catalyst desorption energy was 100.5 kJ/mol. As well, when the iron loading was increased to 10wt% (10-ISA(15)-950), the desorption energy decreased to 84.9 kJ/mol. Additionally, higher iron loading up to 15wt% (15-ISA(15)-950) reduced the desorption energy to 76.4 kJ/mol. These findings suggest that the strong acidity is dominated by chemisorbed NH_3. This is considered to be the case, since the amount of ammonia desorbed is inversely proportional to the activation energy for ammonia desorption. Thus, higher desorption energies lead to lower ammonia desorbed amounts. This observation is in agreement with earlier studies [113, 114] where higher activation energies for desorption were associated to lower desorbed ammonia amounts.

In the case of weak acid sites, the activation energy of ammonia was found not being proportional to the amount of ammonia desorbed, particularly for the samples with low iron loadings (5wt% and 10wt%). This suggests that the NH_3 was physisorbed to weak acid sites. This finding is in agreement with a previous study by Harlin et al. [115] and Lok et al. [116], indicating that physisorbed NH_3 occurs below 200 ^oC adsorption temperatures.

Table 5.3 also reports the estimated activation energies for ammonia desorption from the weak acid sites. One can notice that these activation energies for the three iron loadings were consistently much lower than those for the strong acid sites. For example, the activation energy of 5-ISA(15)-950 in weak acid sites was found to be 11.1 kJ/mol while in the strong acid sites it was found to be 100.5 kJ/mol. This suggests that the activation energies for ammonia desorption are also related to the strength of the acid sites. Karge et al. [117] reported a similar result for a Y-zeolite with a 2.4 to 8.6 Si/Al ratios. The higher desorption energies were found for the stronger acid sites.

5.1.5. SEM image

The fresh Fe_2O_3/SiO_2-Al_2O_3 catalysts were analyzed by Scanning Electron Microscopy (SEM). This was done to investigate the surface catalyst morphology after calcination at different temperatures. Figure 5.8 reports a SEM micrograph for 5-ISA(15)-750, 5-ISA(15)-950 and 5-ISA(15)-1100. From Figure 5.8a, it can be seen that 5-ISA(15)-750 displays a rough surface. After calcination at 950 ^oC however, a much more regular crystal phase formation was observed (Figure 5.8b). This supports the XRD diffractogram results (Figure 5.2), showing an alumina amorphous phase and a γ-Al_2O_3 phase at 750 ^oC and 950 ^oC calcination temperatures. Furthermore, an even smoother surface was observed on the 5-ISA(15)-1100 catalyst (Figure 5.8c). This suggests that iron oxide is homogenously mixed at this condition, with the support. In addition, the smooth 5-ISA(15)-1100 surface is in agreement with a significant decrease in the catalyst porosity, as observed with BET (see Table 5.1).

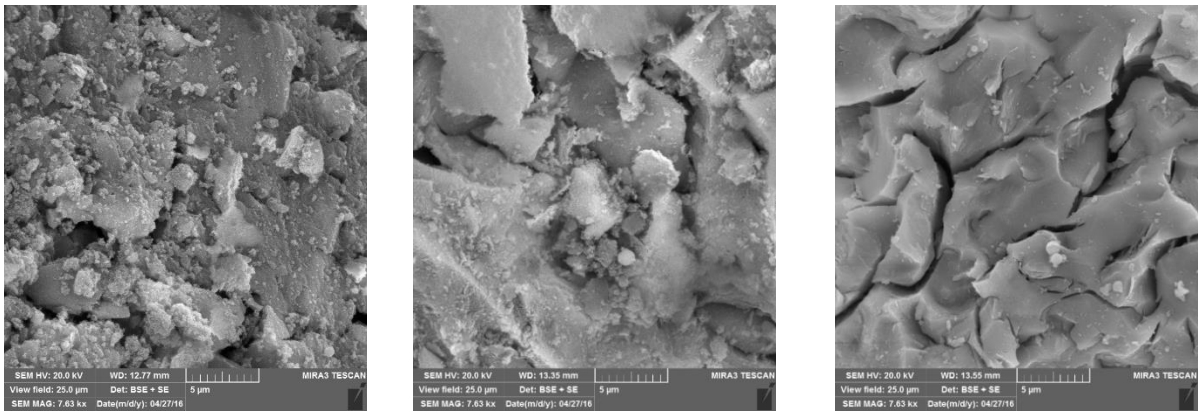

(a) (b) (c)

Figure 5.8. SEM micrograph of (a) of 5-ISA(15)-750, (b) 5-ISA(15)-950 and (c) 5-ISA(15)-1100.

5.2. Catalyst performance

Runs were carried out at temperatures ranging from 400 to 600 ^{o}C, to establish the reaction temperature effect on toluene steam reforming. All experimental conditions involved at least three repeats. Reported results in various figures show average values as well as typical standard deviations for repeats. A steam to toluene molar ratio of 1 was selected, given that toluene conversion is the focus of the present study. The reaction time was set to 20 sec and the 10-ISA(15)-950 catalyst was loaded to comply with a 1.5 catalyst/toluene mass ratio. Preliminary studies also involved toluene steam reforming with no catalyst loaded. This was done to assess the effect of the thermal reaction. As well the chemical equilibrium was calculated using the method proposed by Teh anda Rangaiah [118], and was compared to the experimental data as will be discussed later.

It is worth mentioning that during toluene steam reforming, the following consecutive reactions can occur [35, 119]:

Toluene steam reforming $C_7H_8 + 7H_2O \leftrightarrow 7CO + 11H_2$ $\Delta H^o = +869$ MJ/kmol (5.1)

Methane steam reforming $CH_4 + H_2O \leftrightarrow CO + H_2$ $\Delta H^o = +206$ MJ/kmol (5.2)

Water-gas shift $CO + H_2O \leftrightarrow CO_2 + H_2$ $\Delta H^o = -42$ MJ/kmol (5.3)

CO_2 reforming $CH_4 + CO_2 \leftrightarrow 2CO + 2H_2$ $\Delta H^o = +247$ MJ/kmol (5.4)

Figure 5. 9 reports the toluene steam reforming conversion as well as the composition of dry gas yields at three different iron contents: 5wt% (5-ISA(15)-950), 10wt% (10-ISA(15)-950) and 15wt% (15-ISA(15)-950). It is acknowledged that catalyst acidity favours hydrocarbon cracking, with acid sites promoting protonation of the aromatics via

a carbenium ion [99]. Table 5.2 reports NH_3-TPD with a total acidity for 10-ISA(15)-950 being much higher than that for 5-ISA(15)-950.

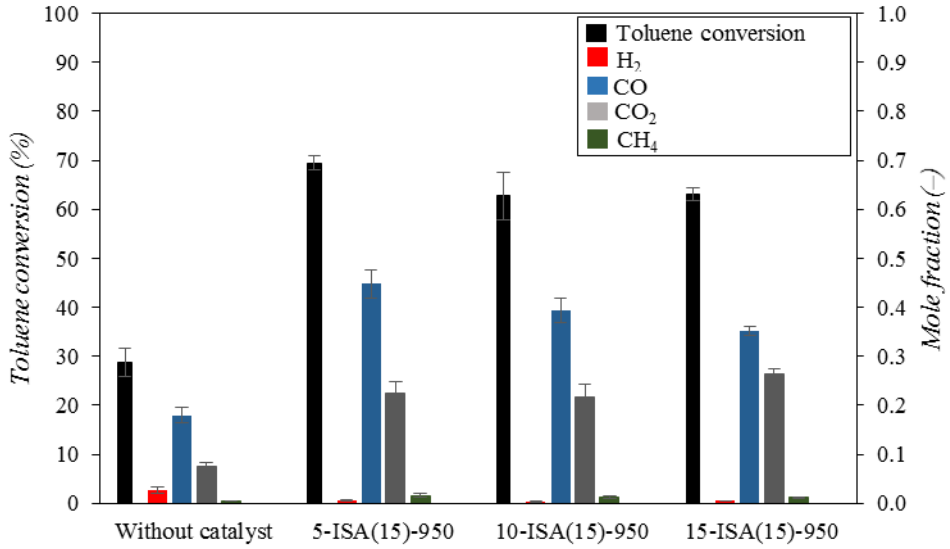

Figure 5. 9. Toluene conversion and composition of producer gas (T = 500°C, P = 380 kPa, toluene to steam ratio = 1, catalyst to toluene ratio = 1.5).

However, the observed reactivity appear not to be in line with the total acidity trends. Chen et al. [120] found that strong acid sites promote tar cracking. Therefore, it was suggested that the toluene conversion reactivity is dominated by strong acid sites. Indeed, toluene conversion was also affected by the specific catalyst surface area. Reduction in specific surface area were confirmed using BET (Table 5.1). In this respect, Kumar et al. [28] reported that the presence of iron on alumina can accelerate the shrinkage of alumina and transform it from gamma to other phases, leading to loss in surface area.

Figure 5. 9 shows that at 500 °C, the toluene conversion decreased from 69% to 63% when the iron loading increased from 5wt% to 10wt% in the ISA(15)-950. To justify these results, it was assumed that the increase in strong acid site density was partially

counterbalanced by the reduction of surface area. However and given a comparable toluene conversion was observed when the the iron loading augmented from 10wt% to 15wt% in the ISA(15)-950 catalysts, a close compensation was hypothesized.

As well, it is shown in the present study that iron loading also has a significant effect on the composition of the producer gas. The increase of iron loading yields higher CO_2 with significantly reduced CO. This suggests that the higher content iron oxide catalysts with a strong acidic site density promote the water-gas shift reaction (Eq. (14)) [108]. This was confirmed by the NH_3-TPD data reported in Table 5.2, with higher strong acidic site densities for the higher iron content catalysts. In this respect, earlier studies also reported that iron oxides catalysts promote the water-gas shift reaction [23, 121]. Furthermore, the CH_4 was consistently observed to be at very low levels (~1%), suggesting that iron oxides favour methane steam reforming (Eq. (13)). Furthermore, given H_2 is essentially a non-detectable species in the 350 – 400 °C range, these results were explained considering reaction times were inadequate to reach chemical equilibrium, as shown in Figure 5. 13 (full lines). This situation changes as soon as temperatures were raised above 450 °C and 20 sec with H_2 yields becoming much closer to the chemical equilibrium.

Figure 5. 10 describes the effect of reaction times on toluene conversion using a 10-ISA(15)-950 catalyst. Reaction times were varied in the 10 to 25 sec range. These runs were developed with the 10-ISA(15)-950 catalyst at 500 ^{o}C, with a steam to toluene ratio of 1, and a toluene to catalyst ratio of 1.5. One can observe a significant change in toluene conversion from 54% to 62% when the reaction time was augmented from 15 s to 20 sec. One should note that a slight increase of toluene conversion from 62% to 64% was observed when the reaction time was varied from 20 to 25 sec. It is considered that this

very limited toluene conversion was the result of toluene steam reforming being very close to thermodynamic chemical equilibrium.

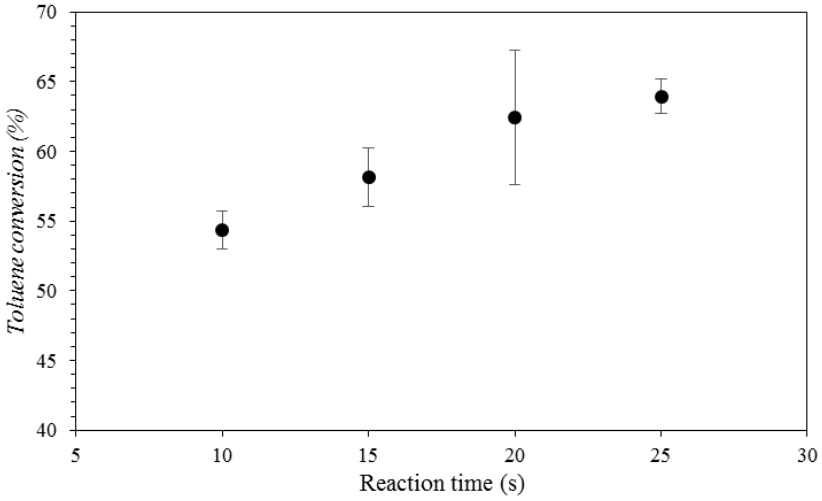

Figure 5. 10. Toluene conversion at different reaction times (T = 500 ºC, P = 380 kPa, toluene to steam ratio = 1, catalyst to toluene ratio = 1.5).

Figure 5. 11 describes the permanent gases compositions and their changes with reaction time. It is also apparent that CO and CO_2 changed significantly up to 20 sec. This is in agreement with the data reported by Mazumder et al. [35], where these authors used supported nickel catalysts. Figure 5. 12 shows that toluene conversion for both thermal and catalytic steam reforming is positively affected at higher reaction temperature. This is consistent and in agreement with others [53, 122, 123]. Higher temperatures enhance endothermic toluene steam reforming (Eq. (12)). A valuable result is the catalytic toluene steam reforming using a 10-ISA(15)-950 catalyst. This catalyst shows a toluene conversion that is more than twice the one for thermal steam reforming. This increased toluene conversion can be assigned to the 29 cm^2/g surface area and 957 µmol/g acidity of 10-ISA(15)-950 catalyst. One should note that these results are in line with the earlier research by Uddin et al. [23].

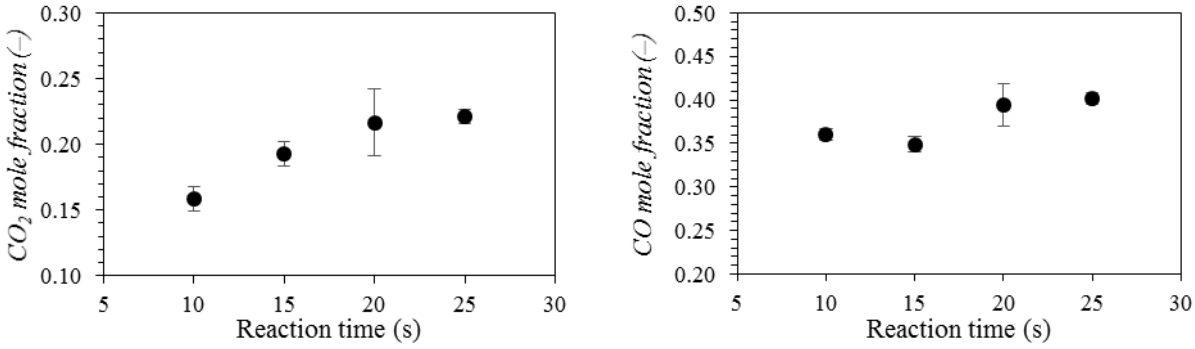

Figure 5. 11. Composition of produced gas at different reaction times (T = 500 ºC, P = 380 kPa, toluene to steam ratio = 1, catalyst to toluene ratio = 1.5).

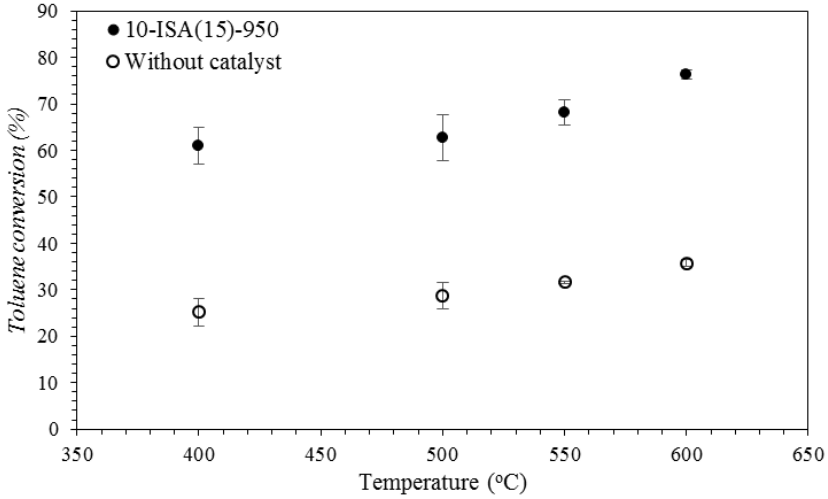

Figure 5. 12. Toluene Conversion at Different Reaction Temperatures (P = 380 kPa, t = 20 sec, toluene to steam ratio = 1, catalyst to toluene ratio = 1.5).

Figure 5. 13 reports the composition of product gas species (H_2, CO, CO_2 and CH_4) at different reaction thermal levels. It can be noticed that in both the catalytic and thermal toluene steam reforming, the H_2 composition increased as the reaction temperature is raised. This suggests that higher temperatures favor toluene steam reforming as described in Eq. (12), with this affecting the overall reaction network during gasification. As a result, in toluene catalytic steam reforming, higher temperatures lead to higher CO and lower CO_2

levels. This is due to the endothermic CO_2 nature of the reforming reaction (Eq. (15)). This result is in agreement with the data from Mazumder et al. [124].

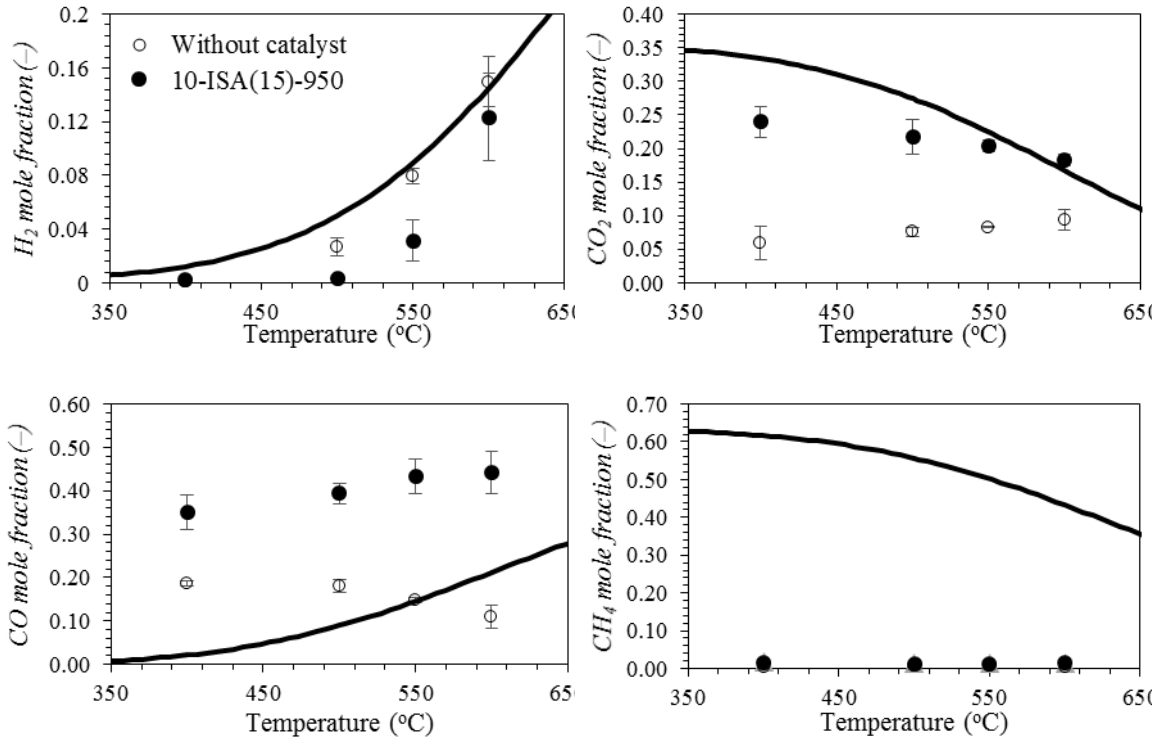

Figure 5. 13. Composition of Produced Gas at Different Reaction Temperatures (T = 500 °C, P = 380 kPa, toluene to steam ratio = 1, catalyst to toluene ratio = 1.5). Full lines: describe the chemical equilibrium mole fraction.

Furthermore, the CO_2 and CO composition trends were of specially interest in the case of for the thermal experiments. Unlike the case of the toluene catalytic steam reforming, during toluene thermal steam reforming, the CO_2 increased while the CO content decreased at higher temperatures.

In summary, steam toluene catalytic gasification led to H_2 and CO_2 yields close to reaction chemical equilibrium at the 500 – 600 °C higher thermal levels. CH_4 yields on the other hand, remained at the level of traces (<1%) with this being attributed to the dominant

methane steam reforming reaction (Eq. (13)). Therefore and as the consequence, the thermodynamic model underpredicts mole fraction of CO obtained from the experiments.

5.3. Conclusions

a) An iron oxide over silica-doped alumina catalysts was successfully synthesized using a One-Pot method. This Fe_2O_3/SiO_2-γAl_2O_3 catalyst was proven to be effective and thermally stable for toluene steam reforming, with iron content significantly affecting catalyst acidity.

b) The iron content of the Fe_2O_3/SiO_2-γAl_2O_3 was found to accelerate the alumina collapse and transform γ-alumina into other phases. The addition of Si ions was also found to enhance the thermal stability of the γ-Al_2O_3 with the presence of Si ions retarding α-Al_2O_3 nucleation.

c) The preparation of the Fe_2O_3/SiO_2-γAl_2O_3 catalyst with a high surface area, large pore sizes and excellent thermal stability, was observed to be affected by the calcination temperature, with 950^{o}C being a preferred thermal level.

d) The prepared Fe_2O_3/SiO_2-γAl_2O_3 catalyst displayed consistently good toluene conversion due to high surface area and high acidity.

e) The synthesized FeO_2/SiO_2-γAl_2O_3 (10-ISA(15)-950) catalyst showed a promising 76% toluene conversion at 600 ^{o}C. H_2 and CO_2 yields observed were close to chemical equilibrium values. This demonstrate the potential of the FeO_2/SiO_2-γAl_2O_3 (10-ISA(15)-950) for the steam reforming of tars from biomass gasification.

CHAPTER 6

RESULTS AND DISCUSSION – THERMODYNAMIC STUDY ON GASIFICATION WITH VARIOUS BIOMASSES

6.1. The effect of gasification temperature

The gasification temperature is the most important operating parameter in biomass gasification. Indeed, it has a significant effect on the heating value and composition of the producer gas [125]. In order to study the effect of the gasification temperature, several simulations were carried out under the following operating conditions: reformer temperature of 800 ^{o}C, oxygen equivalence ratio of zero, and steam to carbon ratio of zero. As shown in Figure 6. 1a, the H_2 and CO composition of the producer gas from gasification of mangrove, algae, rice husk and palm frond were relatively high (above 35%) at gasification temperature of 600^{o}C. This results from the endothermicity of the Boudouard, and steam reforming reactions, which are favored by high gasification temperature. The effect of gasification temperature on H_2/CO ratio of the producer gas from various biomass is illustrated in Figure 6. 1b. For all the studied biomasses, the H_2/CO ratio decreased with increasing gasification temperature until around 900 ^{o}C. This is because carbon conversion through both partial oxidation and methane formation reactions are favored at higher gasification temperature (see Figure 6. 1c), resulting in higher concentration of CO and CH_4, as shown in Figure 6. 1a and Figure 6. 1d, respectively. This result is in agreement with its experimental counterpart reported by Turn et al. [126]. Indeed, higher gasification temperatures enhance carbon conversion, which results in less char formation.

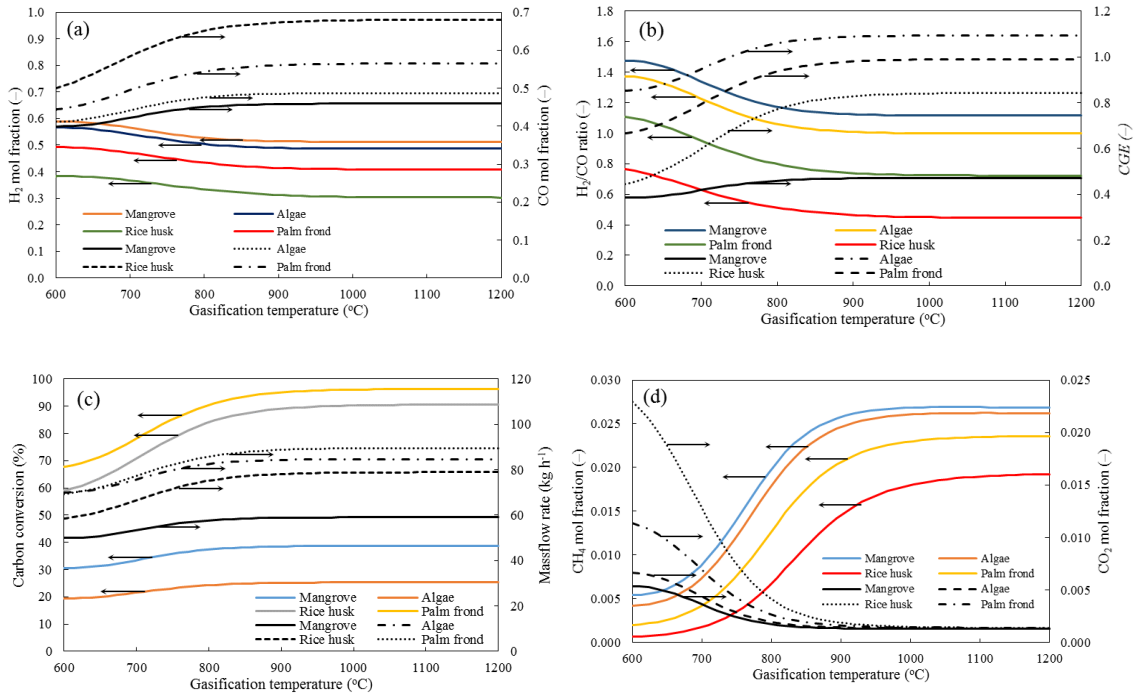

Figure 6. 1. The effect of gasification temperature on (a) the composition of H_2 and CO, (b) H_2/CO ratio and cold gas efficiency, (c) carbon conversion and mass flowrate, and (d) the composition of CH_4 and CO_2.

The H_2/CO ratio remained constant at gasification temperature higher than 900°C because all reaction reached equilibirum due to the absence of the active reactants, particularly oxygen. This is in agreement with the result reported by Wang et al. [127] which states that gasification of biomass ($CH_{1.4}O_{0.59}N_{0.0017}$) at 100 kPa with an oxygen equivalence ratio equal to zero reached equilibrium at temperature of around 1100 K (900°C). It is also found that at the same gasification temperature, the increase of H_2/CO ratio is linearly proportional with the increase of H/O ratio of the biomass, as shown in Figure 6. 2a. For example, at gasification temperature of 600°C, H_2/CO ratio increased in the following order: rice husk (0.76), palm frond (1.11), algae (1.37) and mangrove (1.48). This is because high H/O ratio enhances both steam reforming and methane formation reactions due to high hydrogen composition in the biomass. In addition, it is worth

mentioning that typical composition of other contaminant elements such as sulfur and nitrogen in the biomass is very low [4]. In the case of the gasification of mangrove, the increase of gasification temperature has no appreciable effect on H_2/CO ratio of the producer gas, as shown in Figure 6. 1b. This is attributed to low carbon conversion in gasification of mangrove due to a low oxygen composition (29.14%; see Table 4.3) in mangrove for the partial oxidation reaction and low a activity of the methane formation reaction. In this study, it is found that the highest carbon conversion without additional oxygen supply for mangrove gasification was 38%. This is lower than the value reported by [4]. In this later study, the carbon conversion of biomass gasification at ER = 0 ranged from 65% to 87%.

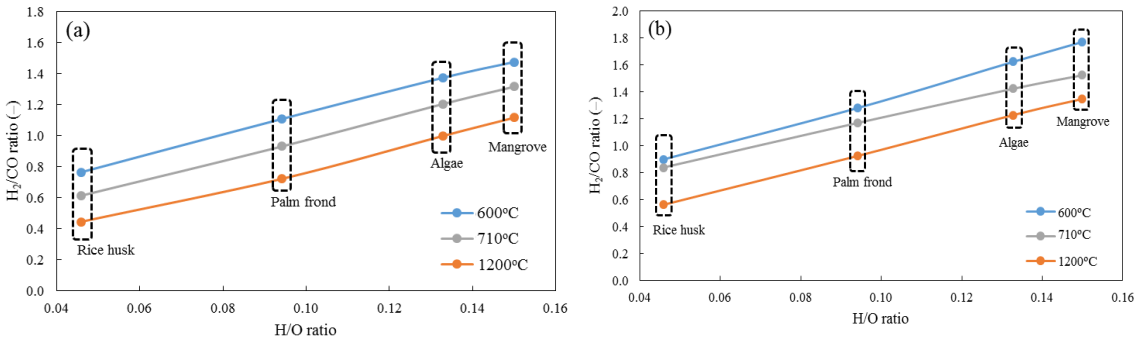

Figure 6. 2. The effect of H/O ratio of biomass on H_2/CO ratio of producer gas at (a) different gasification temperatures (T reformer = 800ºC), and (b) different reformer temperatures (T gasifier = 600ºC).

Figure 6. 1b shows that the CGE increased with increasing gasification temperatures. This is because the composition of CO and CH_4 at larger gasification temperature. At the same gasification temperature, the CGE decreased in the following order: algae, palm frond, rice husk and mangrove. This is attributed to the H_2 and CO composition, and the flowrate of producer gas. The CGE of gasification of mangrove was considerably lower

than CGE of gasification of rice husk, palm frond and algae. This is explained by the fact that the flowrate of producer gas from gasification of mangrove was significantly lower when compared to the producer gas flowrates from rice husk, algae and palm frond. The flowrate of producer gas is significantly affected by carbon conversion during gasification. In the case of the gasification of mangrove, the gasification temperature has only minimal effect on CGE of mangrove. The reason for this is that the gas flowrate has a strong effect on the CGE. From Figure 6. 1c, it is clearly shown that gasification temperature has no significant effect on the flowrate of mangrove gas. The flowrate of algae gas and CO composition of algae gas were slightly lower than those of palm frond gas, as shown in Figure 6. 1c and Figure 6. 1a, respectively. However, H_2 composition of algae gas was much larger than that of palm frond gas. Therefore, the CGE of algae gasification was higher than the CGE of palm frond gasification. For example, at gasification temperature of 600^{o}C, the CO composition of palm frond gas (0.44) was higher than the CO composition of algae gas (0.41). However, the H_2 composition of algae gas (0.57) was higher than the H_2 composition of palm frond gas (0.49). Furthermore, the gas flowrate of algae gas (66 kg/hr) was higher than the gas flowrate of palm frond gas (63 kg/hr). Therefore, the CGE of algae gasification (0.85) was higher than the CGE of palm frond gasification (0.67).

Figure 6. 3a shows the effect of gasification temperature on GSE of gasification of various biomasses. At the same gasification temperature, the GSE decreased in the following order: rice husk, palm frond, algae and mangrove. The heating value and composition of biomass have a significant effect on the GSE. For example, the heating value of mangrove is higher than the heating value of the other biomasses. However, the

GSE of mangrove is lower than the GSE of other biomasses. This is because mangrove has a lower oxygen composition when compared to the other biomasses. This results in low carbon conversion for the gasification of mangrove. The gasification of rice husk showed the highest GSE if compared to gasification of other biomasses. However, the heating value of rice husk is much lower than that of mangrove. This is due to the high oxygen composition in the rice husk, results in high carbon conversion in rice husk gasification.

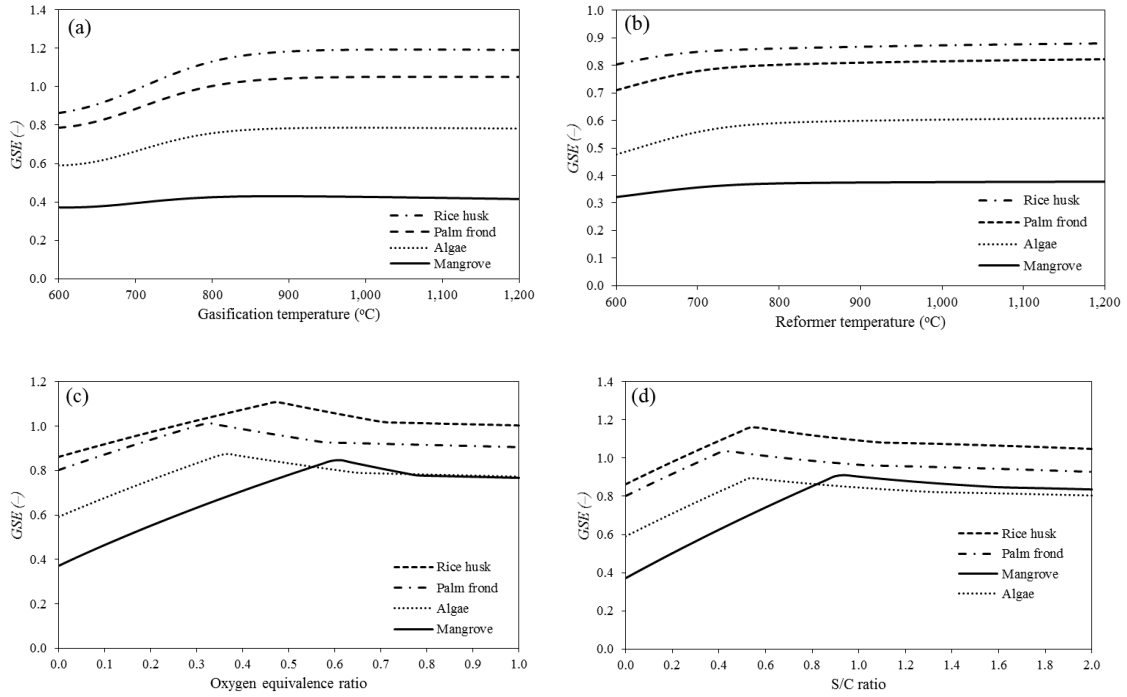

Figure 6. 3. The gasification system efficiency as the function of (a) gasification temperature, (b) reformer temperature, (c) oxygen equivalence ratio, and (d) steam to carbon (S/C) ratio.

6.2. The effect of reformer temperature

The addition of reformer unit in the gasification process enhanced H_2 content in the producer gas [7, 128]. The effect of reformer temperature on the composition of the producer gas is depicted in Figure 6. 4a and Figure 6. 4b. The CO concentration increased

for increasing values of the reformer temperature, while the concentration of CH_4 and CO_2 decreased at larger values of the reformer temperature. This is because high reformer temperature enhanced both the methane reforming and the CO_2 reforming reactions. The concentration of hydrogen increased as the reformer temperature increased up to certain temperature. Further heating in the reformer results in a decrease of H_2 concentration. For example, for a reformer temperature increase from 600 to 673^{o}C, the H_2 concentration of rice husk gas rises from 0.39 to 0.41 (see Figure 6. 4a), while the H_2O concentration decrease from 0.15 to 0.14 (not shown in the figure). When the reformer temperature is higher than 673^{o}C, the concentration of H_2 decrease while the concentration of H_2O and CO increase. This suggests that a reverse water-gas shift reaction occurred at reformer temperatures higher than 673^{o}C due to lack of CH_4, which results in the water-gas shift reaction shifted to the left. The highest H_2 concentrations of the producer gases from palm frond (0.50), algae (0.57) and mangrove (0.59) were obtained at reformer temperature of 722, 771 and 808^{o}C, respectively.

Figure 6. 4c shows the effect of reformer temperature on H_2/CO ratio of the producer gas from gasification of algae, palm frond, mangrove, and rice husk. The H_2/CO ratio decreased with increasing reformer temperature. This is because the increase of CO concentration was larger than the increase of H_2 concentration at higher reforming temperatures. Indeed, higher reformer temperatures favor the endothermic CO_2 reforming reaction. At the same reformer temperature, for example at 600^{o}C, the H_2/CO ratio of the producer gas decreased in the following order: mangrove (1.77), algae (1.62), palm frond (1.28) and rice husk (0.90). It is found that, at reformer temperatures ranging between 600 to 1200^{o}C, the H_2/CO ratio is linearly proportional with the H/O ratio of the biomass (see

Figure 6. 4b). This is because high H/O ratios enhance both the steam reforming and the methane formation reactions due to a high hydrogen content in the reactant (i.e., the biomass).

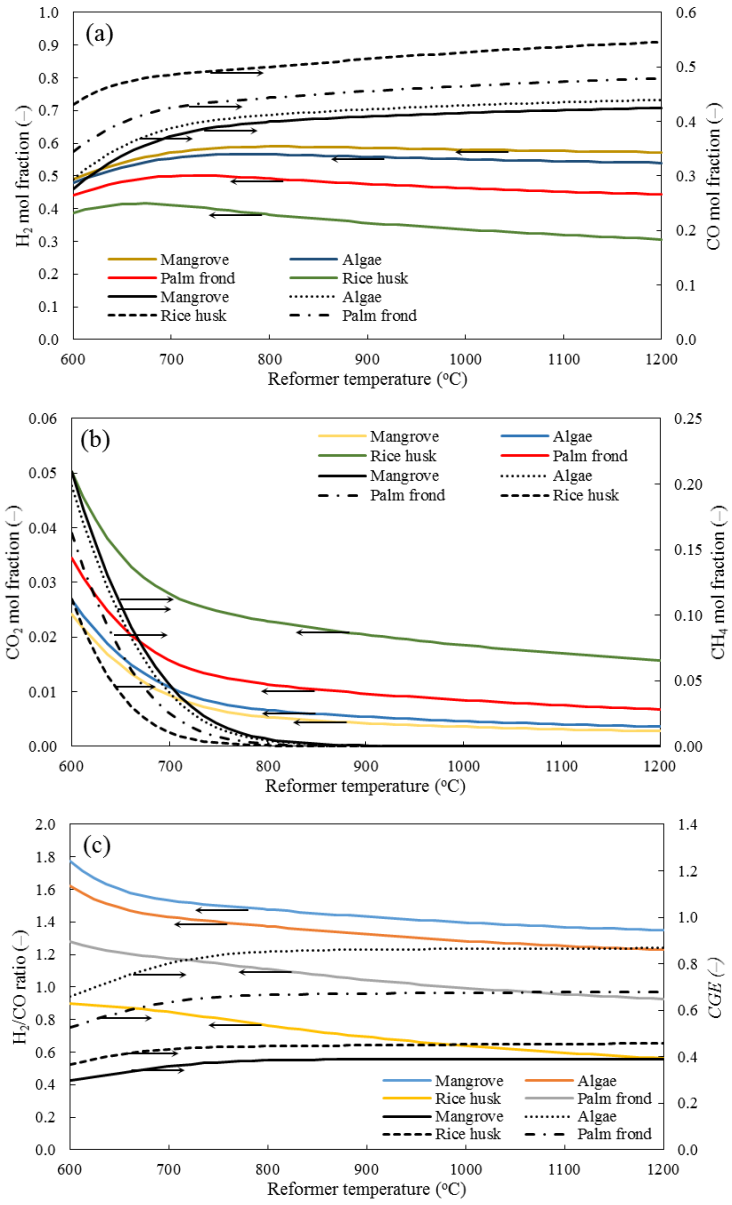

Figure 6. 4. The effect of reformer temperature on (a) the composition of H_2 and CO, (b) the composition of CO_2 and CH_4, and (c) H_2/CO ratio and cold gas efficiency (T gasifier = 600°C).

Cold gas efficiency (CGE) of the producer gas from gasification of algae, palm frond, mangrove, and rice husk increased with increasing reformer temperature, as shown in Figure 6. 4c. This is attributed to the increase of combustible gas composition, mainly H_2 and CO, in the producer gas as the reformer temperature is increased. Indeed, high temperatures enhance the endothermic CO_2 reforming and methane reforming reactions. At the same reformer temperature (e.g., 600^{o}C), the CGE of different biomasses increased in the following order: mangrove (0.30), rice husk (0.37), palm frond (0.53) and algae (0.66). According to the definition of the lower heating value of the producer gas (presented above in section 3), the composition and flowrate of the gasifier product are strongly affected by the composition of the biomass. Therefore, the order of CGE, when we vary the reformer temperature, is similar to the order of CGE when the gasification temperature is varied. The CGE of algae gasification increased significantly from 0.66 to 0.85 as the reformer temperature is increased from 600 to 800^{o}C. This is because the concentration of H_2 and CO have increased due to both the methane reforming and CO_2 reforming reactions. However, when the reformer temperature is larger than than 800^{o}C, the CGE significantly stop increasing. This is attributed to the reverse water-gas shift reaction, which is favored at reformer temperature higher than 800^{o}C. This later reaction consumes CO_2 and H_2, while the concenctration of H_2O and CO increase. The reformer temperature has little effect on the GSE, as shown in Figure 6. 3b. This is due to the fact that the gasification temperatures, which sigficantly affects the GSE was held constant at 600^{o}C.

6.3. The effect of oxygen equivalence ratio (ER)

The oxygen equivalence ratio refers to the ratio of actual oxygen to biomass weight ratio per stoichiometric oxygen to biomass weight ratio. It is an important operating

parameter in biomass gasification [125]. High ER tends to complete the oxidation reaction, which results in high CO_2 composition in the producer gas instead of other gases (i.e., CO, CH_4 and H_2) [129]. In this simulation, gasification temperature and reformer temperature were set at 600^{o}C and 800^{o}C, respectively. The parametric study was performed by varying the additional oxygen supply. Figure 6. 5a shows that the H_2/CO ratio of producer gas from algae, mangrove, palm frond and rice husk decreased as the ER increased. This is due to the fact that the presence of additional oxygen in the gasification system enhanced partial oxidation, which results in an increase of CO concentration in the producer gas and a decrease in H_2 concentration (see Figure 6. 5b). This finding is in agreement with the experimental result observed by [130]. In effect, these authors observed that the composition of combustible gases such as H_2, CO, CH_4 and C_nH_m is reduced with increasing ER. A similar trend was also obtained experimentally by [131] who investigated the effect of ER on the composition of the producer gas in the co-gasification of biomass and coal.

Figure 6. 5c shows that the gasification of mangrove require an ER of 0.61 for complete carbon conversion. On other hand the required ERs, for gasification of rice husk, algae and palm frond were 0.47, 0.37 and 0.33, respectively. The gasification of mangrove required higher ER for complete carbon conversion if compared to the gasification of rice husk, algae and palm frond. This is explained by the decreasing C/O ratio: mangrove (2.28), algae (1.02), palm frond (0.86) and rice husk (1.02). Biomass with higher C/O ratio possesses higher carbon content relative to oxygen content. Therefore, larger additional oxygen supply is required to achieve 100% carbon conversion through the partial oxidation reaction. This is in agreement with the result reported by [44]. Billaud and co-workers

found that the char yield decreased as the ER increased in both their experimental and GASPAR model results. It is worth noticing that at the current operating conditions, the carbon conversion was dominated by the partial oxidation reaction instead of the methane formation and steam reforming reactions. Moreover, the presence of oxygen was used mainly for the partial oxidation other than the hydrogen combustion.

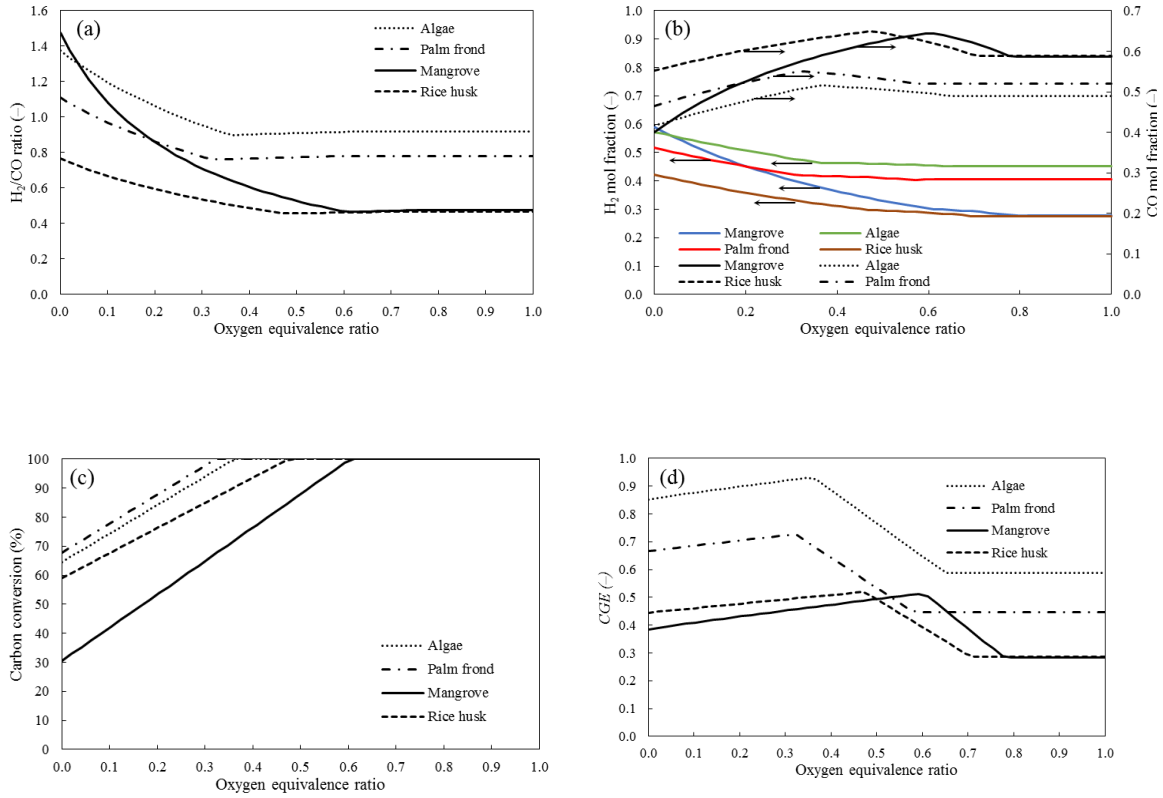

Figure 6. 5. The effect of oxygen equivalence ratio on (a) H_2/CO ratio of producer gas, (b) the composition H_2 and CO, (c) carbon conversion, and (d) cold gas efficiency.

Unlike in the gasification with zero ER, the presence of sufficient oxygen in gasification enhanced the carbon conversion through partial oxidation, which converts carbon into CO. Therefore, when the carbon conversion reaches 100%, due to additional oxygen supply, the H_2/CO ratio of the producer gas is linearly proportional to H/C ratio of biomass. Producer gas with high H_2/CO ratio was obtained from gasification of biomass

with high H/C ratio because of the high hydrogen content. At ER = 0, the H_2/CO ratio of mangrove gas was higher than the H_2/CO of producer gas from other biomasses. However, as the ER increased, the H_2/CO of mangrove gas decreased drastically approaching the value of H_2/CO ratio of rice husk gas. Indeed, while the H/O ratio of mangrove was higher than that of other biomasses, its H/C ratio was close to the H/C ratio of rice husk. When the ER is higher than 0.6, the H_2/CO of mangrove gas remained constant at 0.46 because the concentration of H_2 and CO decreased with a similar slope due to the combustion reactions which convert H_2 and CO into H_2O and CO_2, respectively. The H_2/CO ratio of algae gas and palm frond gas decreased in a similar fashion, while the decrease of H_2/CO ratio of rice husk gas was slightly lower. This is attributed to the value of the H/O ratio and H/C ratio of these various biomasses. When the ER is increased, the CGE of biomass gasification increased. After a certain ER value (optimum ER value), the CGE started decreasing as can be seen in Figure 6. 5d. The increase of CGE is attributed to the increase of the CO content and the flowrate of the producer gas as the ER ratio is increased since carbon conversion increased at higher values of ER. Further increase of ER reduced the CGE because the CO in the producer gas was oxidized into CO_2 due to the presence of an excess of oxygen. The optimum ER value of the biomass depends on the C/O ratio of the biomass. Among the biomasses studied in this work, the lowest optimum ER was exhibited for palm frond gasification (ER = 0.31) with CGE of 0.73, while the highest optimum ER was achieved for the mangrove gasification (ER = 0.59) with CGE of 0.51. The gasification of algae showed the highest CGE (CGE = 0.93) if compared to gasification of other biomasses with an optimum ER of 0.35. Hydrogen composition of algae is higher than the hydrogen composition of palm frond, rice husk and mangrove, explaining the observed

CGE trend. However, the highest GSE was not exhibited for the gasification of algae, as shown in Figure 6. 3c. The highest GSE (1.11) is obtained for the gasification of rice husk at ER of 0.47. The gasification of rice husk consumed less energy when compared to the gasification of other biomass hence the highest observed GSE.

6.4. The effect of steam to carbon (S/C) ratio

Steam to carbon ratio, like oxygen equivalence ratio has a considerable effect on both the energy input and the composition of producer gas [125]. This ratio is defined as a mole of steam per mole of carbon in the biomass. The parametric study was conducted by varying the flow of steam while keeping the flow of biomass constant at a gasification temperature of 600^{o}C and a reformer temperature of 800^{o}C. For gasification of algae, when the S/C ratio<0.53 the H_2/CO ratio remained constant, as shown in Figure 6. 6a. This is due to the fact that the increase of H_2 and CO production are similar in magnitude, through steam reforming reaction (see Figure 6. 6b). However, when S/C>0.53 the H_2/CO ratio sharply increase with increasing S/C ratio since the amount of H_2 continuously increase while the CO remains constant due to lack of carbon source. In other word, for gasification of algae the carbon conversion reached 100% at S/C ratio of 0.53, as shown in Figure 6. 6c. A similar trend was also exhibited for gasification of palm frond, rice husk and mangrove. At S/C ratio of 2.0, when the carbon conversion reached 100% for all biomasses, the H_2/CO ratio of algae gas and palm frond gas were much higher than the H_2/CO ratio of mangrove gas and rice husk gas. This is because the H/C ratio of algae and palm frond were much higher than those of mangrove and rice husk. As the hydrogen amount increased with increasing S/C ratio, the CGE also increased, as shown in Figure 6. 6d. For gasification of algae, the CGE sharply increased as the S/C ratio increased from 0

to 0.53. This is due to the increase of H_2 and CO amounts in producer gas, which result in the increase of LHV of the producer gas. When the S/C ratio increased from 0.53 to 1.31 the CGE slightly decreased (from 1.30 to 1.27). This is due to the decline of the LHV of producer gas because of the low amount of CO and CH_4 in the producer gas. After, the CGE sharply increased (i.e., when the S/C ratio became larger than 1.31). This is explained as follows: the increase of the LHV from H_2 is sufficient to compensate the decrease of the LHV due to the decline of CO and CH_4 content. At S/C of 2 (complete carbon conversion was reached), the CGE decreased in the following order: algae, palm frond, rice husk and mangrove. Indeed, the hydrogen composition of algae is higher than that of palm frond, rice husk and mangrove.

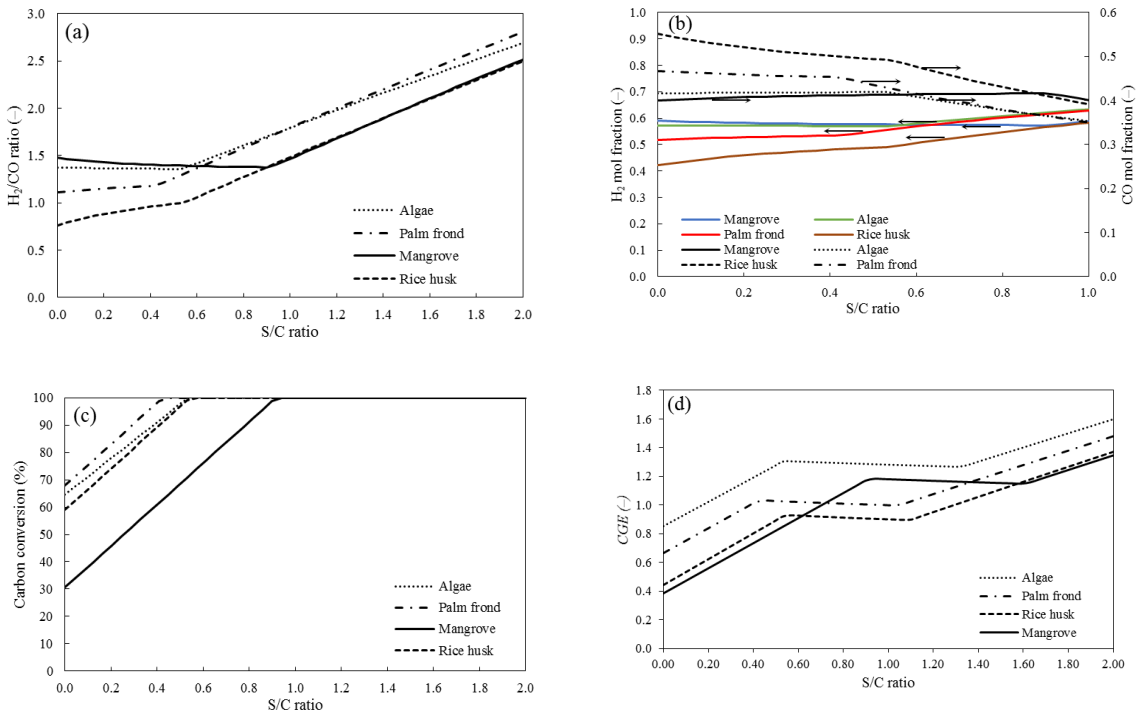

Figure 6. 6. The effect of steam to carbon (S/C) ratio on (a) H_2/CO ratio of producer gas, (b) the composition H_2 and CO, (c) carbon conversion, and (d) cold gas efficiency.

Figure 6. 3d shows the effect of S/C ratio on gas system efficiency (GSE). It is found that the energy input for gasifier and reformer strongly influence the GSE. The GSE of gasification of all biomasses increased with increasing S/C ratio. After a maximum point, the GSE declined as the S/C increased. For example, the GSE of algae gasification reached maximum at 0.89 as the S/C ratio increased up to 0.53. Then, the GSE declined from 0.89 to 0.80 as S/C became higher than 0.53. This trend can be attributed to the carbon conversion trough both steam reforming and partial oxidation reaction. At S/C ratio of 2, the GSE decreased in the following order: rice husk, palm frond, mangrove and algae. This is attributed to the biomass heating value and the composition of hydrogen and carbon in the biomass.

6.5. Conclusions

a) The gasification of algae with oxygen showed the highest CGE (0.93), while gasification with steam exhibited an increase of CGE from 0.85 to 1.60 as the S/C ratio increased from 0 to 2.

b) Rice husk gasification with oxygen exhibited the highest GSE (1.11) at ER of 0.47, while with steam, the highest GSE (0.89) was at S/C ratio of 0.53.

c) The highest H_2/CO ratio was found on the gasification of algae with oxygen.

d) The highest CGE in gasification with oxygen and steam was found for algae, while the highest GSE was achieved for rice husk.

CHAPTER 7

RESULTS AND DISCUSSION – THERMODYNAMIC STUDY ON TAR ELIMINATION IN BIOMASS GASIFICATION

During our parametric study, a non-adiabatic system was assumed for all simulations. The selected temperature of the pyrolysis zone, the combustion zone, the counter-current reduction zone, and the co-current zone are 850 K, 1495 K, 970 K, and 1340 K, respectively. A detailed discussion of the parametric study is provided in the text thereafter, including the model description.

7.1. Model description

We select a biomass feedstock mass flow rate equal to 20 $kg.hr^{-1}$ and an air (i.e., gasifying agent) volumetric flow rate of 28 $m^3.hr^{-1}$. As described in Section 4.3.2 and depicted in Figure 4.3, the gasifier is simulated using six separate processes labeled Drying, Pyrolysis-A, Pyrolysis-B, Combustor (R-1), Counter-current reduction zone (R-2), and Co-current reduction zone (R-3). In the drying process, the moisture content in the biomass (w_{adb}) is vaporized, producing oven-dried biomass (w_{odb}) and water vapor (w_{vap}). The main focus on the Pyrolysis-A is the formation of tar and char. The product of Pyrolysis-A is presented previously in Table 4.6. From Figure 7.1a, it is clear that the amounts of H_2O and CO drastically decrease while the amounts of H_2, CH_4, and CO_2 significantly increase in the Pyrolysis-B. This suggests that the Pyrolysis-B is dominated by both the water-gas shift reaction and the reverse CO_2 reforming reaction. One should notice that the equilibrium are not reached by the char and the tar in the Pyrolysis B. In other words, the

tar and the char are considered as non-reacting components. This can be seen in Figure 7.1a that the amount of char and tar remain constant in the Pyrolysis-B process.

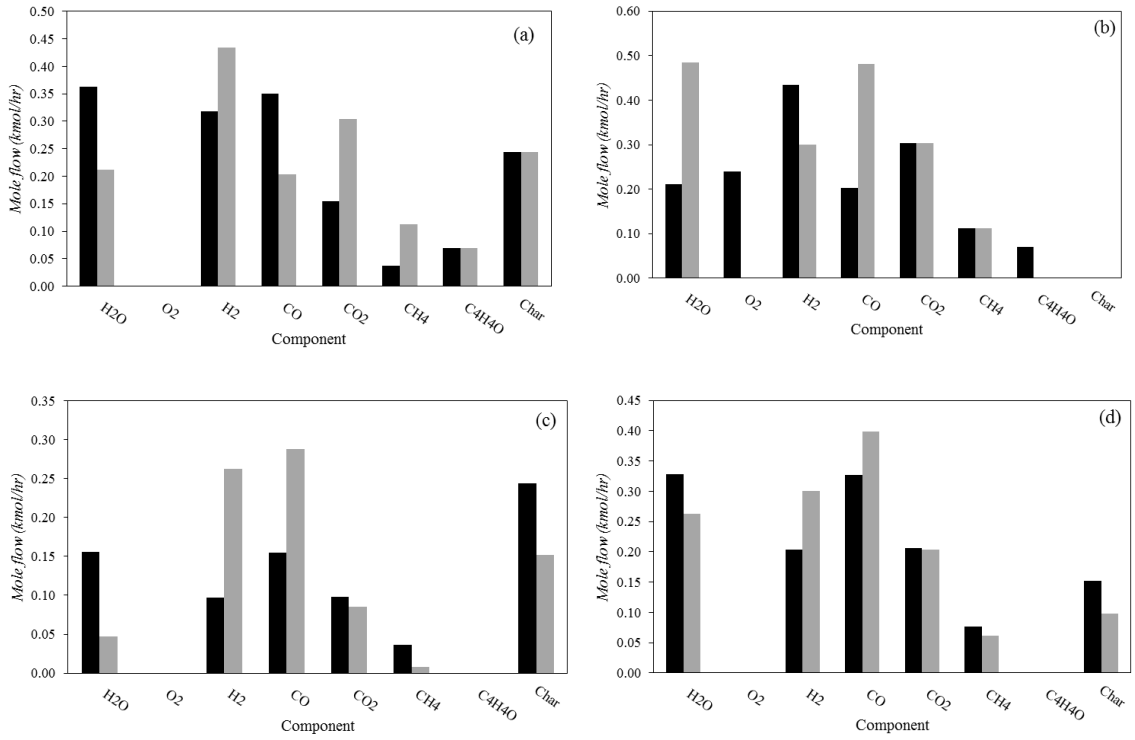

Figure 7.1. Mole flow of the feed and product of (a) Pyrolysis-B, (b) Combustion zone, (c) counter-current reduction zone, and (d) co-current reduction zone. (Feed: black; product: grey).

In the Combustor (R-1), oxygen, an air component, reacts with the volatiles from the Pyrolysis-B ($w_{py\text{-}a}$). Figure 7.1b indicates that the amounts of H_2 and O_2 in the feed stream ($w_{py\text{-}a}$ + w_{air}) are higher than their counterparts in the flue gas stream ($w_{fg\text{-}a}$). This is attributed to hydrogen combustion reaction. This is because in the lack of oxygen environment, the flame speed of hydrogen is much faster than CH_4 or CO [23]. Consequently, the amount of H_2O the flue gas stream ($w_{fg\text{-}a}$) is higher than its counterparts in the combustion feed stream ($w_{py\text{-}a}$ + w_{air}). Due to these exothermic reactions, combustion zone plays a role as a heat source for the gasification process [27]. The similar conclusion is also reported in other studies [22]. Indeed, the temperature in the combustion zone is

sufficient for tar elimination [7]. This is the reason for the absence of C_4H_4O in the combustion product ($w_{fg\text{-}a}$). This suggests that C_4H_4O is decomposed into CO and H_2O through the endothermic furan steam reforming reaction.

The amounts of the components in the inlet and outlet of counter-current reduction zone (R-2) are depicted in Figure 7.1c. As depicted in Figure 7.1c, it is suggested that the steam reforming reaction (Eq. (3)) takes place in the counter-current reduction zone. This is the reason for the decrease of char and H_2O while the CO and H_2 increase. In addition, the amount of CH_4 and CO_2 also decrease. This is because methane and CO_2 reforming reactions (i.e., Eq. (6) and Eq. (7), respectively) are hypothesized to occur as well. Due to these endothermic reactions, the temperature of the counter-current reduction zone (970 K) is lower than that of combustion zone (1495 K). A similar pattern is reported by Susanto and Beenackers [5], showing that their experimental temperature on counter-current reduction zone is lower than its counterpart in the combustion zone. Other experimental studies [22] also reported the same conclusion with moving-bed gasifier.

The amounts of the components in the inlet and outlet of co-current reduction zone (R-3) are depicted in Figure 7.1d. From Figure 7.1d, it is shown that H_2O, CO_2 and CH_4 decrease while H_2 and CO increase. The explanation for this is that the endothermic methane and CO_2 reforming reactions (i.e., Eq. (6) and Eq. (7), respectively) are suggested plays a role in the co-current reduction zone. This implies to the temperature of the co-current reduction zone. The temperature of the co-current reduction zone (1344 K) is lower than that of the combustion zone (1495 K). The hot producer gas from co-current reduction zone ($w_{pg\text{-}h}$) is then cooled to 298 K, producing a producer gas with ambient temperature ($w_{pg\text{-}c}$).

7.2. The effect of O_2 equivalence ratio

The O_2 equivalence ratio is the ratio of actual oxygen to biomass weight ratio per stoichiometric oxygen to biomass weight ratio. The effects of O_2 addition on gasification performance have been studied by varying both the split ratio of O_2 stream as well as the flow of O_2 while keeping a constant biomass flow rate. It is worth mentioning that the supply of O_2 requires more energy for gas purification process as compared to the supply of air [24]. Therefore, the energy required for O_2 production is also taken into account in this study, as discussed earlier in Section 4.3.2.

Figure 7.2 shows that the compositions of CO_2 and H_2O increase when the O_2 equivalence ratio is increased for all combination (i.e., O_2 is fed to combustion zone, counter-current reduction, or co-current reduction zone). The reason for this behavior is that the presence of O_2 enhances partial oxidation reaction produces CO, and shifts both methane reforming and CO_2 reforming reactions to the left. This is further confirmed by a decrease of the compositions of H_2, CO, and CH_4 at higher O_2 equivalence ratios. This finding is in good agreement with the experimental study conducted by Narváez et al. [28], which reported that the compositions of H_2, CO, and CH_4 were reduced when the air equivalence ratio was increased. A similar trend has also been found by Billaud et al. [29] on the gasification of biomass in entrained flow reactor using O_2 as a gasifying agent.

It can be clearly seen from Figure 7.2a that splitting O_2 stream into counter-current reduction zone has a considerable effect on the composition of producer gas. For example, at the O_2 equivalence ratio of 0.3, the concentrations of H_2 and CO raise from 0.23 to 0.28 and from 0.31 to 0.48, respectively, when one shifts the O_2 feed stream from combustion zone to counter-current zone. Also, we find that O_2 addition in the counter-current zone

increases the CO concentration through partial oxidation reaction. Gases with high CO concentrations flow from the counter-current reduction zone to the pyrolysis section. In this later zone, CO reacts with the H_2O from the pyrolysis and drying processes, to produce CO_2 and H_2 thanks to the water-gas shift reaction. In the combustion zone, H_2 reacts with O_2 through hydrogen combustion producing H_2O. Gases with rich H_2O vapor flows to the co-current reduction zone. Then, H_2O vapor coming from the combustion zone reacts with CH_4 leading to the formation of CO and H_2 by the methane reforming reaction. Thus, one can suggest that the increase of CO and H_2 concentrations by injecting O_2 to the combustion zone is mainly due to high CO concentration of the gas from counter-current reduction zone. It is also worth mentioning that higher carbon conversion is observed for the gasification system with O_2 injection into the counter-current reduction zone when compared to the gasification system with O_2 injection into the combustion zone (see Figure 7.3a). Explanation for this observation resides in the fact that counter-current reduction zone contains carbon in its feed. Indeed, carbon reaction with oxygen through partial oxidation reaction is favored when compared to the other reaction constituents (with CO_2 and H_2O) through Boudouard reaction and steam reforming reaction, respectively. This is in line with previous study [22], showing that oxygen is the most active gasifying agent to react with carbon, followed by steam and CO_2.

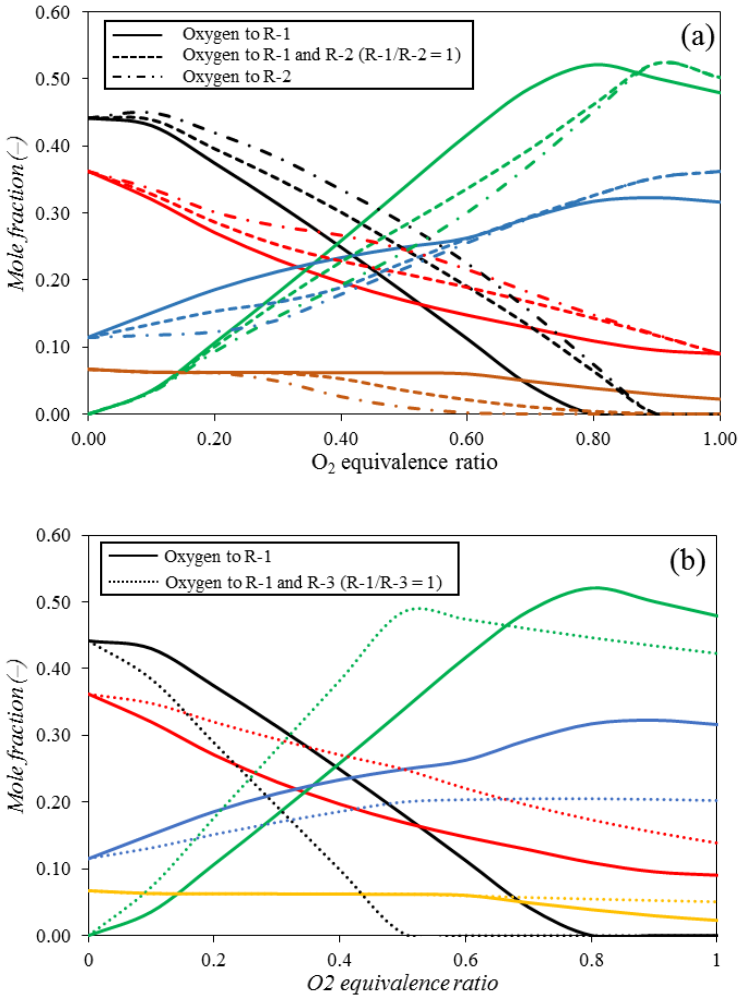

Figure 7.2. The effect of O_2 equivalence ratio on the composition of producer gas (wet basis) at two O_2 injections: (a) to counter-current zone and (b) to co-current zone. (Red: H_2, green: CO_2, blue: H_2O, black: CO and brown: CH_4)

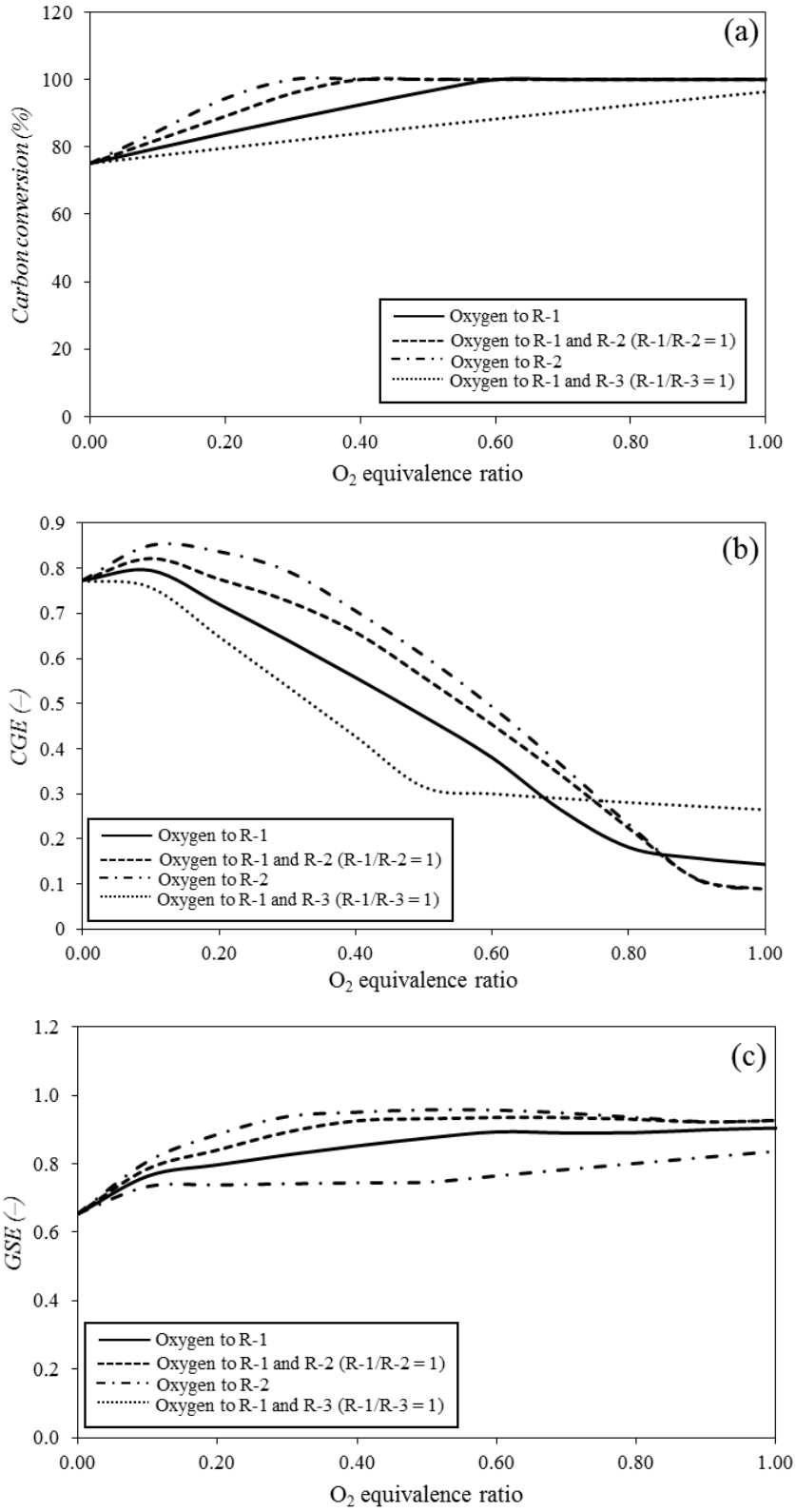

Figure 7.3. The effect of O_2 equivalence ratio at various O_2 injections on (a) carbon conversion, (b) cold gas efficiency, and (c) gasification system efficiency.

As it can be observed in Figure 7.2b, by splitting oxygen feed into combustion zone and co-current reduction zone with the same ratio, the concentrations of H_2, CO_2 and H_2O increase, whereas the content of CO decreases. For instance, at O_2 equivalence ratio of 0.3, the concentration of CO and H_2O decrease from 0.31 to 0.19 and from 0.21 to 0.17, respectively, while the concentrations of H_2 and CO_2 increase from 0.23 to 0.29 and from 0.18 to 0.28, respectively. This results can be explained by noting that the O_2 addition to the co-current reduction zone promotes partial oxidation reaction producing CO. Indeed, high CO concentration enhances water-gas shift reactions resulting the decrease in H_2O and the increase in both H_2 and CO_2. In addition, at high O_2 equivalence ratios, the unreacted O_2 cannot be converted further using partial oxidation reaction since co-current reduction zone is a tail zone. Thus, it can be concluded that the presence of oxygen in the co-current reaction has no positive effect on the gasification process. This is also can explain why low carbon conversion is observed when oxygen feed is split into combustion zone and co-current reduction zone (see Figure 7.3a).

Figure 7.3b shows that the CGE decreases with increasing O_2 equivalence ratio. This is due to the fact that the concentration of CO and H_2 decrease, whereas the content of CO_2 and H_2O increases at higher O_2 equivalence ratios. One should notice that for a fixed O_2 equivalence ratio, the CGE increases when the amount of O_2 to counter-current reduction is increased. For instance, when the oxygen is injected to combustion zone, the CGE is 0.64, whereas the CGE increases to 0.79 if oxygen is injected to counter-current reduction zone, at O_2 equivalence ratio of 0.3. This can be explained by the fact that the addition of O_2 to counter-current reduction zone yields higher H_2 and CO concentrations in the producer gas. Conversely, this behavior is reversed when O_2 is split to co-current reduction

zone. A decrease of CGE is observed if O_2 to co-current reduction is increased. At the same O_2 equivalence ratio, for example, when we use an O_2 equivalence ratio = 0.3, the CGE is equal to 0.54 (a decrease by 16%, if compared to what one gets with oxygen feed into the combustion zone). In effect, the lower flow rate of producer gas is resulting from the lower carbon conversion. One should note that if the O_2 equivalence ratio is higher than 0.5, the decrease of CGE tends to plateau due to the absence of CO. Thus, the decrease of CGE is mainly caused by the decrease of H_2 concentration since the CH_4 concentration shows no significant decrease.

Figure 7.3c shows that the GSE increases at higher O_2 equivalence ratios. The reason for this lays in the fact that the increase of O_2 promotes higher conversion of the biomass. A similar finding trend has also been reported by Billaud [44] (i.e., higher O_2 equivalence ratio yields higher carbon conversion). Consequently, the energy that is released from the biomass also increases. This is confirmed by carbon conversion in Figure 7.3a. Again, at the same O_2 equivalence ratio, the GSE increases when the amount of O_2 fed to the counter-current reduction zone is increased. This can be explained by the fact that high CO and H_2 concentrations are obtained when the oxygen feed to the counter-current reduction zone is raised. Lower GSE is observed if the split ratio of O_2 to co-current reduction zone is increased. Indeed, a low flow rate of the producer gas is observed due to a low carbon conversion.

7.3. The effect of steam addition

Steam to carbon (S/C) ratio refers to moles of steam as a gasifying agent per mole of carbon in the biomass feedstock. It has been reported that S/C ratio has a significant effect on the gasification [30]. In the downdraft gasifier with an internal recycle, one should

notice that the reliability of the ejector as the source of suction force for the recycle gas is exceptionally substantial [5]. It is worth noticing that the previous study [31] reported a good performance of the ejector, when the steam was used as a motive fluid. A parametric study is conducted by varying both the split ratio of steam stream and the S/C ratio. In addition, the O_2 equivalence ratio is set at 0.3 during simulation. For all steam feeding combinations, the concentration of H_2 and CO_2 increase while CO content decreases as the S/C ratio is increased, as shown in Figure 7.4a and Figure 7.4b. This is due to the fact that steam enhances H_2 production since the steam plays a role as a hydrogen carrier [32]. It is worth mentioning that at the same S/C ratio, the H_2 concentration increases with increasing amount of steam in the counter-current reduction zone. For instance, at S/C ratio of 2, when the steam is injected to the combustion zone, the concentration of H_2 is equal to 0.28. However, if the steam is injected to the counter-current reduction zone, the H_2 concentration rises to 0.33. Reason for this observation lays in the fact that a high concentration of H_2O vapor in the counter-current reduction zone promotes the water-gas shift reaction. In addition, the unreacted steam may be converted into H_2 by the steam reforming, the methane reforming, and furan steam reforming reactions in the preceding zones (i.e., the combustion zone and the co-current reduction zone). Figure 7.5a confirms that the carbon conversion is boosted by an increase of the amount of steam in the counter-current reduction zone. This is also confirmed by the composition of CO, as depicted in Figure 7.4a. Indeed, this figure indicates that the CO composition increases when the steam is entirely injected to the counter-current reduction zone.

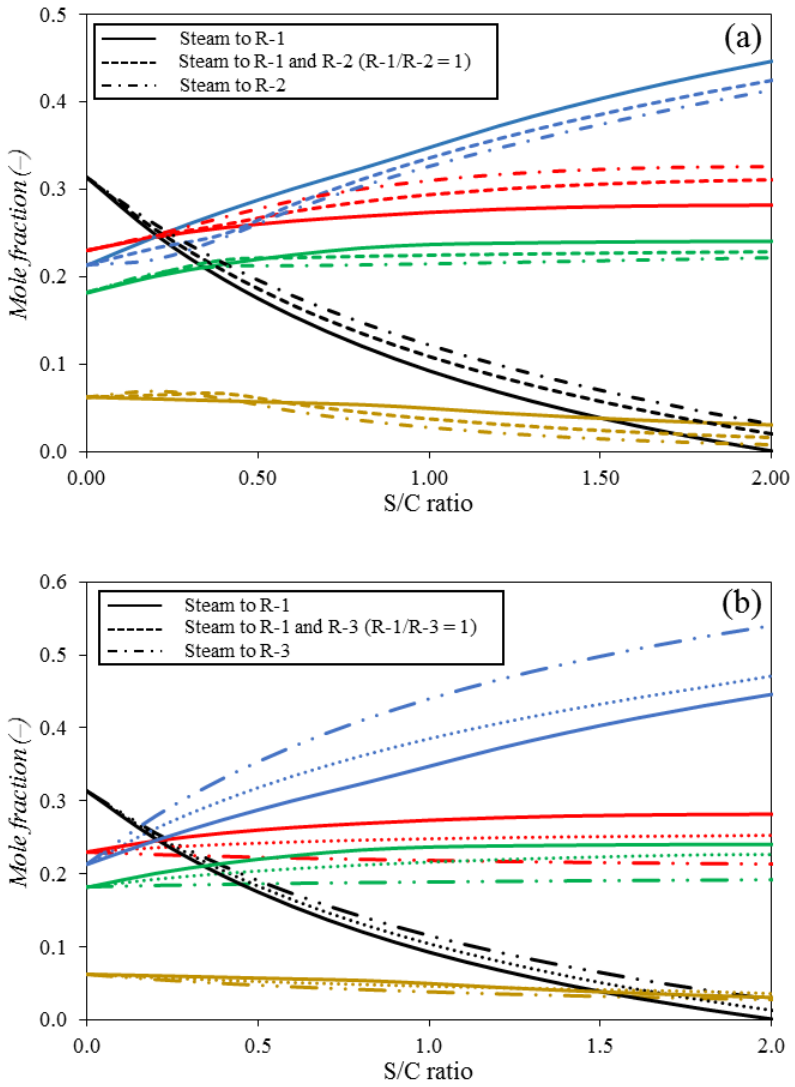

Figure 7.4. The effect of S/C ratio on the composition of producer gas (dry basis) at two steam injections: (a) to counter-current zone and (b) to co-current zone. (Red: H_2, green: CO_2, blue: H_2O, black: CO and brown: CH_4)

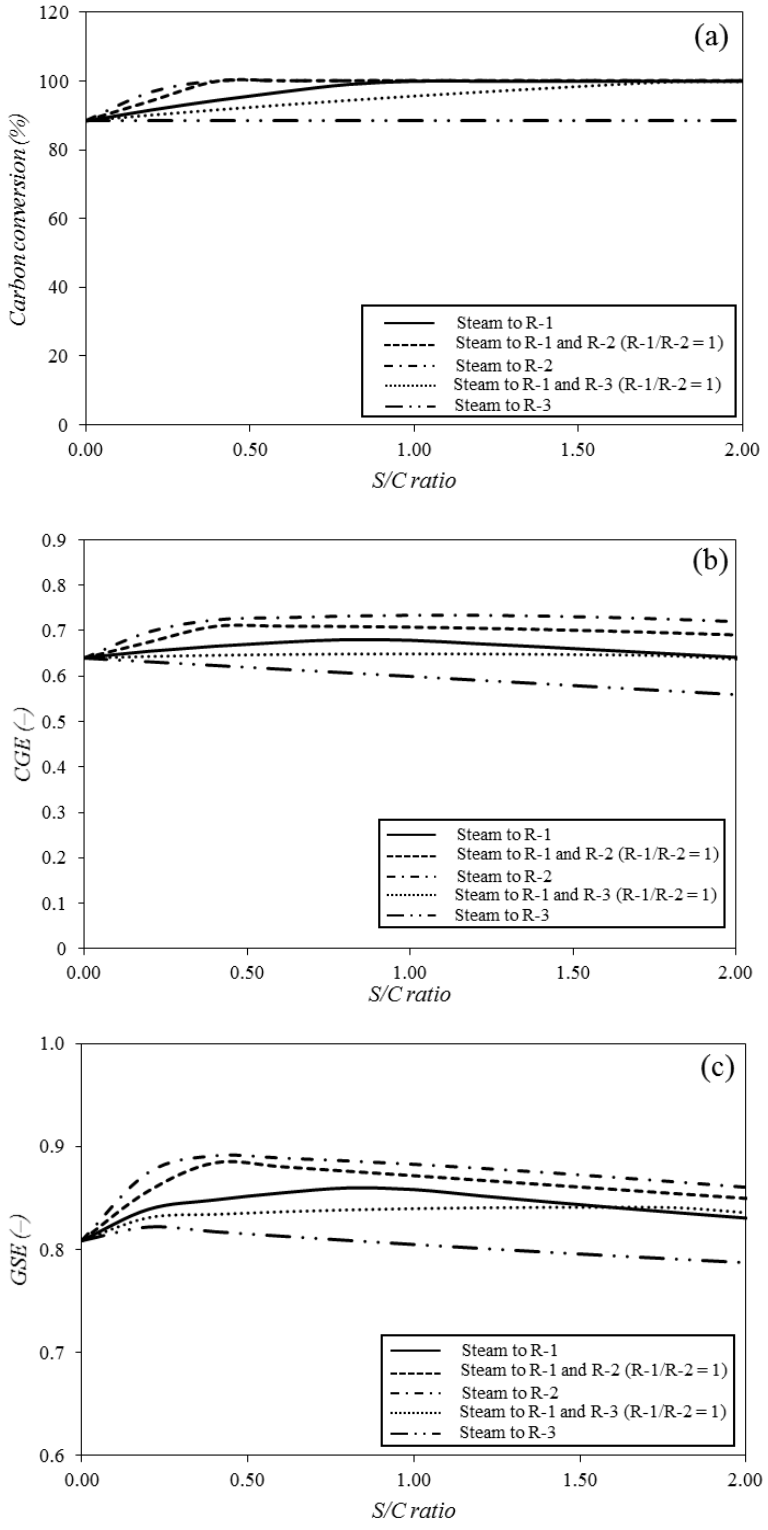

Figure 7.5. The effect of S/C ratio at various steam injections on (a) carbon conversion, (b) cold gas efficiency, and (c) gasification system efficiency.

The injection of steam through the co-current reduction zone mitigates the H_2 concentration, as shown in Figure 7.4b. At the same S/C ratio, the H_2 concentration decreases as the steam injection to the co-current reduction zone is increased. For instance, at S/C ratio of 2, the H_2 concentration decreases from 0.28 to 0.23 when the steam feed is shifted from combustion zone into co-current reduction zone. This results can be explained by noting that the co-current reduction zone is a tail zone. Therefore, the unreacted steam from the co-current reduction zone cannot be converted further into H_2.

Figure 7.5b shows that the CGE increases as the S/C ratio is increased up to certain S/C ratio depends on the combination of steam injection. Then, the CGE decrease if the S/C is continuously increased. For instance, the highest CGE when the steam is injected to the combustion zone is observed at 0.68 when S/C ratio reach 0.80. On the other hand, if the steam is injected to the counter-current reduction zone, the highest achievable CGE is equal to 0.72 while S/C ratio reach 0.40. It is also worth noticing that injecting steam to the co-current reduction zone leads to an adverse effect on the CGE. These behaviors can be explained by assessing the value of the flow rate of the producer gas, which is significantly affected by the carbon conversion. As a consequence, the increase of the flow rate of the producer gas is proportional to the increase of carbon conversion [29]. This is also confirmed by carbon conversion as shown in Figure 7.5a.

Figure 7.5c shows that the GSE changes for varying combinations of steam injection. However, the similar trend is observed for all combinations of steam injection. An optimum S/C ratio differs based on the steam injection combination. For example, the highest GSE is observed at 0.89 when the S/C ratio is 0.4 and the steam is injected to the counter-current reduction zone. On the other hand, lower value of the maximum GSE of 0.86 is observed

if the steam is injected to the combustion zone with the S/C ratio of 0.8. However, the GSE is mitigated if the amount of steam to the co-current reduction zone is increased. For instance, at S/C ratio of 2, the GSE decreases from 0.83 to 0.79 as the steam flow is shifted from combustion zone to the co-current reduction zone. These patterns can be attributed to significant effect of flow rate of the producer gas on the GSE. Indeed, the carbon conversion is considerably affected by the carbon conversion. This is further confirmed by carbon conversion as shown in Figure 7.5a.

7.4. Conclusions

a) A new approach on the thermodynamic simulation of gasification process has been developed using Aspen Plus. Indeed, the formation of tar is taken into account in the present model.

b) The present model provides higher accuracy (relative error: 4% – 11%) when compared to the conventional model (relative error: 33%).

c) The variation of the split ratio of gasifying agent (steam or O_2) into different zones (combustion zone, counter-current reduction zone, and/or co-current reduction zone) has a considerable effect on the gasification performance.

d) The gasification with O_2 injection to the counter-current reduction zone shows a higher CGE (0.79) relative to the CGE (0.64) obtained for the gasification with O_2 injection into the combustion zone. However, injecting O_2 to the co-current reduction zone has an adverse effect on the gasification performance (CGE = 0.54).

e) A positive effect on gasification performance is observed when steam is injected to the counter-current reduction zone (H_2 concentration = 0.33, CGE = 0.72, and GSE = 0.89). On the other hand, negative effects on gasification performance are found

when the steam is injected to the co-current reduction zone (H_2 concentration = 0.23, CGE = 0.56, and GSE = 0.79).

CHAPTER 8

CONCLUSIONS AND RECOMMENDATIONS

8.1. Conclusion of experimental work

The iron oxide over silica-doped alumina catalysts has been successfully synthesized using one-pot method. The FeO_2/SiO_2-Al_2O_3 catalysts herein has been proven as an effective and thermally stable catalysts for toluene steam reforming. The conclusions of the study on the catalyst development are mentioned bellow:

a. The presence of iron has significant contribution on the acidity of the catalysts.

b. The iron accelerate the alumina to collapse and transform into other phase.

c. The addition of Si ions can enhance the thermal stability of γ-Al_2O_3 at high temperature since the presence of Si ions can retard the nucleation α-Al_2O_3.

d. An effective calcination temperature for synthesizing the iron oxide over silica-doped alumina catalysts with high surface area, large pore size and excellent thermal stability was 950^oC.

e. The catalytic toluene stream reforming experiments exhibits high performance of the Fe_2O_3/SiO_2-Al_2O_3 catalysts in term of toluene conversion due to high surface area and high acidity.

f. The Fe_2O_3/SiO_2-Al_2O_3 with 5wt% Fe loading exhibited higher toluene conversion (69.50%) as compared to toluene conversion of the Fe_2O_3/SiO_2-Al_2O_3 catalysts with 10wt% iron loading (62.7%) and 15wt% iron loading (63.1%).

g. The toluene conversion increased with increasing reaction temperature. The 10-ISA(15)-950 catalysts exhibits high toluene conversion (76.3%) at reaction temperature of 600^{o}C.

h. The composition of gas products (H_2, CO, CO_2 and CH_4) are approaching chemical equilibrium as the reaction time and temperature were increased.

i. Taking account of these aspects, the iron oxide over silica-doped alumina catalysts are highly potential for steam reforming of tars from biomass gasification.

8.2. Conclusion of thermodynamic study of gasification with various biomasses

In this work, a thermodynamic simulation of gasification process using various biomass such as rice husk, palm frond, algae (*N. oculta*) and mangrove was conducted in Aspen plus. The conclusions of this thermodynamic study are mentioned bellow:

a. The gasification with zero gasifying agent showed that at the same gasification temperature, the increase of H_2/CO ratio is proportional with the increase of H/O ratio of biomass.

b. The installation of reformer unit showed enhancement on the H_2 composition in the producer gas for gasification of all biomass.

c. The gasification of algae with oxygen as a gasifying agent showed highest CGE at ER of 0.35 with CGE of 0.93.

d. The use of steam as a gasifying agent for algae gasification exhibited continuous improvement of CGE from 0.85 to 1.60 as the S/C ratio increased from 0 to 2.

e. On rice husk gasification with oxygen, the highest GSE was shown at ER of 0.47 with GSE of 1.11.

f. The gasification of rice husk with steam as a gasifying agent showed highest GSE at S/C ratio of 0.53 with CGE of 0.89.

g. Algae showed the highest H_2/CO ratio and CGE on gasification with both air and steam as the gasifying agent while the highest GSE was shown on gasification of rice husk.

8.3. Conclusion of thermodynamic study of tar elimination in biomass gasification

A new approach on the thermodynamic simulation of gasification process has been developed using Aspen Plus. Indeed, the formation of tar is taken into account in the present model. The conclusions of this study are mentioned bellow:

a. The present model provides higher accuracy (relative error: 4% – 11%) when compared to the conventional model (relative error: 33%).

b. The variation of the split ratio of gasifying agent (steam or O_2) into different zones (combustion zone, counter-current reduction zone, and/or co-current reduction zone) has a considerable effect on the gasification performance.

c. The gasification with O_2 injection to the counter-current reduction zone shows a higher CGE (0.79) relative to the CGE (0.64) obtained for the gasification with O2 injection into the combustion zone. However, injecting O_2 to the co-current reduction zone has an adverse effect on the gasification performance (CGE = 0.54).

d. A positive effect on gasification performance is observed when steam is injected to the counter-current reduction zone (H2 concentration = 0.33, CGE = 0.72, and GSE = 0.89). On the other hand, negative effects on gasification performance are found when the steam is injected to the co-current reduction zone (H_2 concentration = 0.23, CGE = 0.56, and GSE = 0.79).

8.4. Future work

a. Investigation of the performance of the supported iron oxide catalyst on toluene steam reforming with the presence of producer gas

b. Investigation of the catalysts performance at different steam to toluene ratios

c. The use of oxygen as gasifying agent for toluene conversion

d. Evaluation on the performance of biomass gasification with chemical looping

REFERENCES

1. *International Energy Outlook 2016*. 2016, U.S Energy Information Administration.
2. OECD/IEA, *CO2 emission from fuel combustion: Highlights*. 2016, International Energy Agency: Paris, France.
3. McKendry, P., *Energy production from biomass (part 1): overview of biomass.* Bioresource Technology, 2002. **83**(1): p. 37-46.
4. De Lasa, H., et al., *Catalytic steam gasification of biomass: Catalysts, thermodynamics and kinetics.* Chemical Reviews, 2011. **111**(9): p. 5404-5433.
5. Shahbaz, M., et al., *Fluidization of palm kernel shell, palm oil fronds, and empty fruit bunches in a swirling fluidized bed gasifier.* Particulate Science and Technology, 2016: p. 1-8.
6. Pode, R., *Potential applications of rice husk ash waste from rice husk biomass power plant.* Renewable and Sustainable Energy Reviews, 2016. **53**: p. 1468-1485.
7. Kraisornkachit, P., et al., *Performance evaluation of different combined systems of biochar gasifier, reformer and CO2 capture unit for synthesis gas production.* International Journal of Hydrogen Energy, 2016. **41**(31): p. 13408-13418.
8. López-González, D., et al., *Kinetic analysis and thermal characterization of the microalgae combustion process by thermal analysis coupled to mass spectrometry.* Applied Energy, 2014. **114**: p. 227-237.
9. Ali, S.A.M., S.A. Razzak, and M.M. Hossain, *Apparent kinetics of high temperature oxidative decomposition of microalgal biomass.* Bioresource Technology, 2015. **175**: p. 569-577.
10. Kebelmann, K., et al., *Intermediate pyrolysis and product identification by TGA and Py-GC/MS of green microalgae and their extracted protein and lipid components.* Biomass and Bioenergy, 2013. **49**: p. 38-48.
11. Kennes, D., et al., *Bioethanol production from biomass: Carbohydrate vs syngas fermentation.* Journal of Chemical Technology and Biotechnology, 2016. **91**(2): p. 304-317.
12. Guan, G., et al., *Catalytic steam reforming of biomass tar: Prospects and challenges.* Renewable and Sustainable Energy Reviews, 2016. **58**: p. 450-461.
13. Abu El-Rub, Z., E.A. Bramer, and G. Brem, *Review of catalysts for tar elimination in biomass gasification processes.* Industrial and Engineering Chemistry Research, 2004. **43**(22): p. 6911-6919.
14. Nordgreen, T., T. Liliedahl, and K. Sjöström, *Metallic iron as a tar breakdown catalyst related to atmospheric, fluidised bed gasification of biomass.* Fuel, 2006. **85**(5–6): p. 689-694.
15. Guangul, F.M., S.A. Sulaiman, and A. Ramli, *Gasifier selection, design and gasification of oil palm fronds with preheated and unheated gasifying air.* Bioresource Technology, 2012. **126**: p. 224-232.
16. Kook, J.W., et al., *Gasification and tar removal characteristics of rice husk in a bubbling fluidized bed reactor.* Fuel, 2016. **181**: p. 942-950.
17. Loha, C., H. Chattopadhyay, and P.K. Chatterjee, *Thermodynamic analysis of hydrogen rich synthetic gas generation from fluidized bed gasification of rice husk.* Energy, 2011. **36**(7): p. 4063-4071.

18. Zhu, Y., et al., *Fluidized Bed Co-gasification of Algae and Wood Pellets: Gas Yields and Bed Agglomeration Analysis.* Energy and Fuels, 2016. **30**(3): p. 1800-1809.
19. Basu, P., *Chapter 5 - Gasification Theory and Modeling of Gasifiers*, in *Biomass Gasification and Pyrolysis*. 2010, Academic Press: Boston. p. 117-165.
20. Guan, G., et al., *Catalytic steam reforming of biomass tar over iron- or nickel-based catalyst supported on calcined scallop shell.* Applied Catalysis B: Environmental, 2012. **115–116**: p. 159-168.
21. Ashok, J., et al., *Bi-functional hydrotalcite-derived NiO-CaO-Al2O3 catalysts for steam reforming of biomass and/or tar model compound at low steam-to-carbon conditions.* Applied Catalysis B: Environmental, 2015. **172-173**: p. 116-128.
22. Koike, M., et al., *alpha-aluminaComparative study on steam reforming of model aromatic compounds of biomass tar over Ni and Ni-Fe alloy nanoparticles.* Applied Catalysis A: General, 2015. **506**: p. 151-162.
23. Azhar Uddin, M., et al., *Catalytic decomposition of biomass tars with iron oxide catalysts.* Fuel, 2008. **87**(4-5): p. 451-459.
24. Shen, Y. and K. Yoshikawa, *Recent progresses in catalytic tar elimination during biomass gasification or pyrolysis - A review.* Renewable and Sustainable Energy Reviews, 2013. **21**: p. 371-392.
25. Susanto, H. and A.A.C.M. Beenackers, *A moving-bed gasifier with internal recycle of pyrolysis gas.* Fuel, 1996. **75**(11): p. 1339-1347.
26. Asadullah, M., K. Fujimoto, and K. Tomishige, *Catalytic performance of Rh/CeO2 in the gasification of cellulose to synthesis gas at low temperature.* Industrial and Engineering Chemistry Research, 2001. **40**(25): p. 5894-5900.
27. Mardkhe, M.K., et al., *Synthesis and characterization of silica doped alumina catalyst support with superior thermal stability and unique pore properties.* Journal of Porous Materials, 2015: p. 1-13.
28. Kumar, K.N.P., et al., *Pore-structure stability and phase transformation in pure and M-doped (M = La, Ce, Nd, Gd, Cu, Fe) alumina membranes and catalyst supports.* Journal of Materials Science Letters, 1996. **15**(3): p. 266-270.
29. Beguin, B., E. Garbowski, and M. Primet, *Stabilization of alumina toward thermal sintering by silicon addition.* Journal of Catalysis, 1991. **127**(2): p. 595-604.
30. Busca, G., *Chapter Three - Structural, Surface, and Catalytic Properties of Aluminas*, in *Advances in Catalysis*, C.J. Friederike, Editor. 2014, Academic Press. p. 319-404.
31. Jenkins, B.M., et al., *Combustion properties of biomass.* Fuel Processing Technology, 1998. **54**(1–3): p. 17-46.
32. McKendry, P., *Energy production from biomass (part 2): conversion technologies.* Bioresource Technology, 2002. **83**(1): p. 47-54.
33. McKendry, P., *Energy production from biomass (part 3): gasification technologies.* Bioresource Technology, 2002. **83**(1): p. 55-63.
34. Fagbemi, L., L. Khezami, and R. Capart, *Pyrolysis products from different biomasses: application to the thermal cracking of tar.* Applied Energy, 2001. **69**(4): p. 293-306.

35. Mazumder, J. and H. De Lasa, *Fluidizable Ni/La2O3-γAl2O3 catalyst for steam gasification of a cellulosic biomass surrogate.* Applied Catalysis B: Environmental, 2014. **160-161**(1): p. 67-79.
36. Higman, C. and M. van der Burgt, *Gasification*. Gasification. 2008.
37. Sánchez, C., et al., *A new model for coal gasification on pressurized bubbling fluidized bed gasifiers.* Energy Conversion and Management, 2016. **126**: p. 717-723.
38. Basu, P., *Chapter 6 - Design of Biomass Gasifiers*, in *Biomass Gasification and Pyrolysis*. 2010, Academic Press: Boston. p. 167-228.
39. Phillips, J., *Different Types of Gasifiers and Their Integration with Gas Turbines*. EPRI / Advanced Coal Generation: Charlotte.
40. Prabowo, B., et al., *Pilot scale autothermal gasification of coconut shell with CO<inf>2</inf>-O<inf>2</inf> mixture.* Frontiers in Energy, 2015. **9**(3): p. 362-370.
41. Shen, Y., et al., *In situ catalytic conversion of tar using rice husk char/ash supported nickel-iron catalysts for biomass pyrolytic gasification combined with the mixing-simulation in fluidized-bed gasifier.* Applied Energy, 2015. **160**: p. 808-819.
42. Udomsirichakorn, J. and P.A. Salam, *Review of hydrogen-enriched gas production from steam gasification of biomass: The prospect of CaO-based chemical looping gasification.* Renewable and Sustainable Energy Reviews, 2014. **30**: p. 565-579.
43. Channiwala, S.A. and P.P. Parikh, *A unified correlation for estimating HHV of solid, liquid and gaseous fuels.* Fuel, 2002. **81**(8): p. 1051-1063.
44. Billaud, J., et al., *Influence of H2O, CO2 and O2 addition on biomass gasification in entrained flow reactor conditions: Experiments and modelling.* Fuel, 2016. **166**: p. 166-178.
45. Min, Z., et al., *Catalytic reforming of tar during gasification. Part I. Steam reforming of biomass tar using ilmenite as a catalyst.* Fuel, 2011. **90**(5): p. 1847-1854.
46. Berrueco, C., et al., *Effect of temperature and dolomite on tar formation during gasification of torrefied biomass in a pressurized fluidized bed.* Energy, 2014. **66**: p. 849-859.
47. Yan, F., et al., *Hydrogen-rich gas production by steam gasification of char from biomass fast pyrolysis in a fixed-bed reactor: Influence of temperature and steam on hydrogen yield and syngas composition.* Bioresource Technology, 2010. **101**(14): p. 5633-5637.
48. Mazumder, J. and H.I. de Lasa, *Catalytic steam gasification of biomass surrogates: Thermodynamics and effect of operating conditions.* Chemical Engineering Journal, 2016. **293**: p. 232-242.
49. Li, C. and K. Suzuki, *Tar property, analysis, reforming mechanism and model for biomass gasification—An overview.* Renewable and Sustainable Energy Reviews, 2009. **13**(3): p. 594-604.
50. Yu, H., et al., *Characteristics of tar formation during cellulose, hemicellulose and lignin gasification.* Fuel, 2014. **118**: p. 250-256.

51. Vidian, F., A. Surjosatyo, and Y.S. Nugroho, *Thermodynamic Model for Updraft Gasifier with External Recirculation of Pyrolysis Gas.* Journal of Combustion, 2016. **2016**.
52. Virginie, M., et al., *Characterization and reactivity in toluene reforming of a Fe/olivine catalyst designed for gas cleanup in biomass gasification.* Applied Catalysis B: Environmental, 2010. **101**(1–2): p. 90-100.
53. Virginie, M., C. Courson, and A. Kiennemann, *Toluene steam reforming as tar model molecule produced during biomass gasification with an iron/olivine catalyst.* Comptes Rendus Chimie, 2010. **13**(10): p. 1319-1325.
54. Swierczynski, D., C. Courson, and A. Kiennemann, *Study of steam reforming of toluene used as model compound of tar produced by biomass gasification.* Chemical Engineering and Processing: Process Intensification, 2008. **47**(3): p. 508-513.
55. Devi, L., K.J. Ptasinski, and F.J.J.G. Janssen, *A review of the primary measures for tar elimination in biomass gasification processes.* Biomass and Bioenergy, 2003. **24**(2): p. 125-140.
56. Machin, E.B., et al., *Tar reduction in downdraft biomass gasifier using a primary method.* Renewable Energy, 2015. **78**: p. 478-483.
57. Anis, S. and Z.A. Zainal, *Tar reduction in biomass producer gas via mechanical, catalytic and thermal methods: A review.* Renewable and Sustainable Energy Reviews, 2011. **15**(5): p. 2355-2377.
58. Abu El-Rub, Z., E.A. Bramer, and G. Brem, *Experimental comparison of biomass chars with other catalysts for tar reduction.* Fuel, 2008. **87**(10–11): p. 2243-2252.
59. Phuphuakrat, T., T. Namioka, and K. Yoshikawa, *Tar removal from biomass pyrolysis gas in two-step function of decomposition and adsorption.* Applied Energy, 2010. **87**(7): p. 2203-2211.
60. Zanzi, R., K. Sjöström, and E. Björnbom, *Rapid high-temperature pyrolysis of biomass in a free-fall reactor.* Fuel, 1996. **75**(5): p. 545-550.
61. Pan, Y.G., et al., *Removal of tar by secondary air in fluidised bed gasification of residual biomass and coal.* Fuel, 1999. **78**(14): p. 1703-1709.
62. Brandt, P., E. Larsen, and U. Henriksen, *High tar reduction in a two-stage gasifier.* Energy and Fuels, 2000. **14**(4): p. 816-819.
63. Sutton, D., B. Kelleher, and J.R.H. Ross, *Review of literature on catalysts for biomass gasification.* Fuel Processing Technology, 2001. **73**(3): p. 155-173.
64. Asadullah, M., K. Tomishige, and K. Fujimoto, *A novel catalytic process for cellulose gasification to synthesis gas.* Catalysis Communications, 2001. **2**(2): p. 63-68.
65. Devi, L., et al., *Olivine as tar removal catalyst for biomass gasifiers: Catalyst characterization.* Applied Catalysis A: General, 2005. **294**(1): p. 68-79.
66. Bambal, A.S., K.S. Vecchio, and R.J. Cattolica, *Catalytic effect of Ni and Fe addition to gasifier bed material in the steam reforming of producer gas.* Industrial and Engineering Chemistry Research, 2014. **53**(35): p. 13656-13666.
67. Nordgreen, T., T. Liliedahl, and K. Sjöström, *Elemental Iron as a Tar Breakdown Catalyst in Conjunction with Atmospheric Fluidized Bed Gasification of Biomass: A Thermodynamic Study.* Energy & Fuels, 2006. **20**(3): p. 890-895.

68. Rhodes, C., G.J. Hutchings, and A.M. Ward, *Water-gas shift reaction: finding the mechanistic boundary.* Catalysis Today, 1995. **23**(1): p. 43-58.
69. Nordgreen, T., et al., *Iron-based materials as tar depletion catalysts in biomass gasification: Dependency on oxygen potential.* Fuel, 2012. **95**: p. 71-78.
70. Shabbar, S. and I. Janajreh, *Thermodynamic equilibrium analysis of coal gasification using Gibbs energy minimization method.* Energy Conversion and Management, 2013. **65**: p. 755-763.
71. Melgar, A., et al., *Thermochemical equilibrium modelling of a gasifying process.* Energy Conversion and Management, 2007. **48**(1): p. 59-67.
72. Chaiwatanodom, P., S. Vivanpatarakij, and S. Assabumrungrat, *Thermodynamic analysis of biomass gasification with CO2 recycle for synthesis gas production.* Applied Energy, 2014. **114**: p. 10-17.
73. Ravikiran, A., et al., *Generalized Analysis of Gasifier Performance using Equilibrium Modeling.* Industrial & Engineering Chemistry Research, 2012. **51**(4): p. 1601-1611.
74. Jarungthammachote, S. and A. Dutta, *Equilibrium modeling of gasification: Gibbs free energy minimization approach and its application to spouted bed and spout-fluid bed gasifiers.* Energy Conversion and Management, 2008. **49**(6): p. 1345-1356.
75. Renganathan, T., et al., *CO2 utilization for gasification of carbonaceous feedstocks: A thermodynamic analysis.* Chemical Engineering Science, 2012. **83**: p. 159-170.
76. Gopaul, S.G., A. Dutta, and R. Clemmer, *Chemical looping gasification for hydrogen production: A comparison of two unique processes simulated using ASPEN Plus.* International Journal of Hydrogen Energy, 2014. **39**(11): p. 5804-5817.
77. Mostafavi, E., et al., *Simulation of high-temperature steam-only gasification of woody biomass with dry-sorption CO2 capture.* Canadian Journal of Chemical Engineering, 2016. **94**(9): p. 1648-1656.
78. Rossi, C.C.R.S., L. Cardozo-Filho, and R. Guirardello, *Gibbs free energy minimization for the calculation of chemical and phase equilibrium using linear programming.* Fluid Phase Equilibria, 2009. **278**(1–2): p. 117-128.
79. de Lasa, H.I., *Riser simulator*. 1992, Google Patents.
80. Tijmensen, M.J.A., et al., *Exploration of the possibilities for production of Fischer Tropsch liquids and power via biomass gasification.* Biomass and Bioenergy, 2002. **23**(2): p. 129-152.
81. Peters, L., et al., *CO2 removal from natural gas by employing amine absorption and membrane technology—A technical and economical analysis.* Chemical Engineering Journal, 2011. **172**(2–3): p. 952-960.
82. Kraisornkachit, P., et al., *Performance evaluation of different combined systems of biochar gasifier, reformer and CO2 capture unit for synthesis gas production.* International Journal of Hydrogen Energy.
83. Pinto, F., et al., *Effect of gasification agent on co-gasification of rice production wastes mixtures.* Fuel, 2016. **180**: p. 407-416.
84. Neves, D., et al., *Characterization and prediction of biomass pyrolysis products.* Progress in Energy and Combustion Science, 2011. **37**(5): p. 611-630.

85. Gomez-Barea, A., et al., *Devolatilization of wood and wastes in fluidized bed.* Fuel Processing Technology, 2010. **91**(11): p. 1624-1633.
86. Di Blasi, C., et al., *Product distribution from pyrolysis of wood and agricultural residues.* Industrial and Engineering Chemistry Research, 1999. **38**(6): p. 2216-2224.
87. Gibbs, G.J. and H.F. Calcote, *Effect of Molecular Structure on Burning Velocity.* Journal of Chemical & Engineering Data, 1959. **4**(3): p. 226-237.
88. Zanzi, R., K. Sjöström, and E. Björnbom, *Rapid pyrolysis of agricultural residues at high temperature.* Biomass and Bioenergy, 2002. **23**(5): p. 357-366.
89. Jayah, T.H., et al., *Computer simulation of a downdraft wood gasifier for tea drying.* Biomass and Bioenergy, 2003. **25**(4): p. 459-469.
90. Ramimoghadam, D., M.Z.B. Hussein, and Y.H. Taufiq-Yap, *The Effect of Sodium Dodecyl Sulfate (SDS) and Cetyltrimethylammonium Bromide (CTAB) on the Properties of ZnO Synthesized by Hydrothermal Method.* International Journal of Molecular Sciences, 2012. **13**(10): p. 13275-13293.
91. Lizárraga, R., et al., *Structural characterization of amorphous alumina and its polymorphs from first-principles XPS and NMR calculations.* Physical Review B, 2011. **83**(9): p. 094201.
92. Glinka, A., B. Pacewska, and S. Michałowski, *Investigation of thermal decomposition of hydrated aluminium oxide.* Journal of thermal analysis, 1984. **29**(5): p. 953-957.
93. Osaki, T., et al., *Silica-doped alumina cryogels with high thermal stability.* Journal of Non-Crystalline Solids, 2007. **353**(24-25): p. 2436-2442.
94. Mazumder, J. and H.I. de Lasa, *Ni catalysts for steam gasification of biomass: Effect of La2O3 loading.* Catalysis Today, 2014. **237**: p. 100-110.
95. Shutilov, A.A., et al., *Effect of silica on the stability of the nanostructure and texture of fine-particle alumina.* Kinetics and Catalysis, 2012. **53**(1): p. 125-136.
96. Lee, S.K., et al., *Structure of Amorphous Aluminum Oxide.* Physical Review Letters, 2009. **103**(9): p. 095501.
97. Trueba, M. and S.P. Trasatti, *γ-Alumina as a Support for Catalysts: A Review of Fundamental Aspects.* European Journal of Inorganic Chemistry, 2005. **2005**(17): p. 3393-3403.
98. Ashok, J. and S. Kawi, *Nickel-iron alloy supported over iron-alumina catalysts for steam reforming of biomass tar model compound.* ACS Catalysis, 2014. **4**(1): p. 289-301.
99. Abbot, J., *Role of Brønsted and Lewis acid sites during cracking reactions of alkanes.* Applied Catalysis, 1989. **47**(1): p. 33-44.
100. Zaki, T., *Catalytic dehydration of ethanol using transition metal oxide catalysts.* Journal of Colloid and Interface Science, 2005. **284**(2): p. 606-613.
101. Barthomeuf, D., *Zeolite acidity dependence on structure and chemical environment. Correlations with catalysis.* Materials Chemistry and Physics, 1987. **17**(1): p. 49-71.
102. Auroux, A., *Acidity characterization by microcalorimetry and relationship with reactivity.* Topics in Catalysis, 1997. **4**(1): p. 71-89.

103. Kayo, A., T. Yamaguchi, and K. Tanabe, *The effect of preparation method on the acidic and catalytic properties of iron oxide.* Journal of Catalysis, 1983. **83**(1): p. 99-106.
104. Connell, G. and J.A. Dumesic, *Acidic properties of binary oxide catalysts*. Journal of Catalysis, 1986. **102**(1): p. 216-233.
105. Murrell, L.L. and R.L. Garten, *Mössbauer spectroscopy as a probe of FeO on TiO2 and Ir-Fe on TiO2 - unique preparation of a highly dispersed bimetallic system.* Applications of Surface Science, 1984. **19**(1): p. 218-226.
106. Yaripour, F., et al., *Catalytic dehydration of methanol to dimethyl ether (DME) over solid-acid catalysts.* Catalysis Communications, 2005. **6**(2): p. 147-152.
107. Mollavali, M., et al., *Relationship between surface acidity and activity of solid-acid catalysts in vapour phase dehydration of methanol.* Fuel Processing Technology, 2009. **90**(9): p. 1093-1098.
108. Nie, R., et al., *Core–shell structured CuO–ZnO@H-ZSM-5 catalysts for CO hydrogenation to dimethyl ether.* Fuel, 2012. **96**: p. 419-425.
109. Cvetanović, R.J. and Y. Amenomiya, *A Temperature Programmed Desorption Technique for Investigation of Practical Catalysts.* Catalysis Reviews, 1972. **6**(1): p. 21-48.
110. Cvetanović, R.J. and Y. Amenomiya, *Application of a Temperature-Programmed Desorption Technique to Catalyst Studies*, in *Advances in Catalysis*, H.P. D.D. Eley and B.W. Paul, Editors. 1967, Academic Press. p. 103-149.
111. White, M.G., in *Heterogeneous Catalisis*. 1990, Prentice Hall: New Jersey, USA.
112. Tonetto, G., J. Atias, and H. de Lasa, *FCC catalysts with different zeolite crystallite sizes: acidity, structural properties and reactivity.* Applied Catalysis A: General, 2004. **270**(1–2): p. 9-25.
113. Hossain, M.M., *Co–Pd/γ-Al2O3 catalyst for heavy oil upgrading: Desorption kinetics, reducibility and catalytic activity.* The Canadian Journal of Chemical Engineering, 2012. **90**(4): p. 946-955.
114. Ayandiran, A.A., et al., *Oxidative dehydrogenation of propane to propylene over VOX/CaO-γ-Al2O3 using lattice oxygen.* Catalysis Science and Technology, 2016. **6**(13): p. 5154-5167.
115. Tiitta, M., et al., *Medium and large pore zeolites in n-hexene skeletal isomerization,* in *Studies in Surface Science and Catalysis*, M.C. E. van Steen and L.H. Callanan, Editors. 2004, Elsevier. p. 2323-2330.
116. Lok, B.M., B.K. Marcus, and C.L. Angell, *Characterization of zeolite acidity. II. Measurement of zeolite acidity by ammonia temperature programmed desorption and FTi.r. spectroscopy techniques.* Zeolites, 1986. **6**(3): p. 185-194.
117. Karge, H.G., V. Dondur, and J. Weitkamp, *Investigation of the distribution of acidity strength in zeolites by temperature-programmed desorption of probe molecules. 2. Dealuminated Y-type zeolites.* Journal of Physical Chemistry, 1991. **95**(1): p. 283-288.
118. Teh, Y.S. and G.P. Rangaiah, *A Study of Equation-Solving and Gibbs Free Energy Minimization Methods for Phase Equilibrium Calculations.* Chemical Engineering Research and Design, 2002. **80**(7): p. 745-759.
119. Zhao, B., et al., *Steam reforming of toluene as model compound of biomass pyrolysis tar for hydrogen.* Biomass and Bioenergy, 2010. **34**(1): p. 140-144.

120. Chen, G.Y., et al., *Catalytic Cracking of Tar from Biomass Gasification over a HZSM-5-Supported Ni-MgO Catalyst.* Energy and Fuels, 2015. **29**(12): p. 7969-7974.
121. Simell, P.A., J.K. Leppälahti, and J.B.s. Bredenberg, *Catalytic purification of tarry fuel gas with carbonate rocks and ferrous materials.* Fuel, 1992. **71**(2): p. 211-218.
122. Kuba, M., et al., *Influence of bed material coatings on the water-gas-shift reaction and steam reforming of toluene as tar model compound of biomass gasification.* Biomass and Bioenergy, 2016. **89**: p. 40-49.
123. Ashok, J. and S. Kawi, *Steam reforming of toluene as a biomass tar model compound over CeO2 promoted Ni/CaO–Al2O3 catalytic systems.* International Journal of Hydrogen Energy, 2013. **38**(32): p. 13938-13949.
124. Mazumder, J. and H.I. de Lasa, *Fluidizable La2O3 promoted Ni/γ-Al2O3 catalyst for steam gasification of biomass: Effect of catalyst preparation conditions.* Applied Catalysis B: Environmental, 2015. **168–169**: p. 250-265.
125. Gungor, A., *Modeling the effects of the operational parameters on H2 composition in a biomass fluidized bed gasifier.* International Journal of Hydrogen Energy, 2011. **36**(11): p. 6592-6600.
126. Turn, S., et al., *An experimental investigation of hydrogen production from biomass gasification.* International Journal of Hydrogen Energy, 1998. **23**(8): p. 641-648.
127. Wang, S., X. Bi, and S. Wang, *Thermodynamic analysis of biomass gasification for biomethane production.* Energy, 2015. **90, Part 2**: p. 1207-1218.
128. Gao, N., et al., *Hydrogen-rich gas production from biomass steam gasification in an updraft fixed-bed gasifier combined with a porous ceramic reformer.* International Journal of Hydrogen Energy, 2008. **33**(20): p. 5430-5438.
129. Morf, P., P. Hasler, and T. Nussbaumer, *Mechanisms and kinetics of homogeneous secondary reactions of tar from continuous pyrolysis of wood chips.* Fuel, 2002. **81**(7): p. 843-853.
130. Narváez, I., et al., *Biomass Gasification with Air in an Atmospheric Bubbling Fluidized Bed. Effect of Six Operational Variables on the Quality of the Produced Raw Gas.* Industrial & Engineering Chemistry Research, 1996. **35**(7): p. 2110-2120.
131. Li, K., R. Zhang, and J. Bi, *Experimental study on syngas production by co-gasification of coal and biomass in a fluidized bed.* International Journal of Hydrogen Energy, 2010. **35**(7): p. 2722-2726.

VITAE

Name : Muflih Arisa Adnan

Nationality : Indonesian

Date of birth : May 20th, 1991

Email : muflih.adnan@gmail.com

Academic background : B. Eng. in Chemical Engineering from Sebelas Maret University, Indonesia

Publications (in progress):

1. **Muflih A. Adnan**, Oki Muraza, Shaikh A. Razzak, Mohammad M. Hossain, Hugo I. de Lasa (2016), Iron Oxide over a Silica-Doped Alumina Catalyst for Catalytic Steam Reforming of Toluene as a Surrogate Tar Biomass Species, submitted to Renewable Energy.

2. **Muflih A. Adnan**, Housam Binous, Oki Muraza, Shaikh A. Razzak, Mohammad M. Hossain (2016), Performance prediction of biomass gasification based on the biomass composition: A thermodynamic approach, submitted to Energy.

3. **Muflih A. Adnan**, Herri Susanto, Housam Binous, Oki Muraza, Mohammad M. Hossain, (2016), Enhancement of hydrogen production in a modified moving bed downdraft gasifier – A thermodynamic study by including tar, submitted to International Journal of Hydrogen Energy.

Conference:

1. **Muflih A. Adnan**, Mohammad M. Hossain, Oki Muraza, (2016), Iron-silica doped alumina as an effective support for tar cracking catalyst in biomass gasification, accepted on 7th Student Conference in Madina, Saudi Arabia.

2. Dwi Hantoko, **Muflih A. Adnan**, Sunu Herwi Pranolo (2012), Performance Prediction of Biomass Gasification in Fixed-Bed Gasifier Based on Selection Size and Shape of Biomass Particle, 19th Regional Symposium on Chemical Engineering, Denpasar, Bali, Indonesia.